Title
Manipulating Materials: Electronic and Topological Properties of Chemically and Structurally Complex Materials

Author
Mack, Stephanie

Publication Date
2019

Peer reviewed|Thesis/dissertation

Manipulating Materials: Electronic and Topological Properties of Chemically and Structurally Complex Materials

by

Stephanie Alexandra Mack

A dissertation submitted in partial satisfaction of the

requirements for the degree of

Doctor of Philosophy

in

Physics

in the

Graduate Division

of the

University of California, Berkeley

Committee in charge:

Professor Jeffrey B. Neaton, Chair
Professor Steven G. Louie
Professor Mark Asta

Fall 2019

Manipulating Materials: Electronic and Topological Properties of Chemically and Structurally Complex Materials

Abstract

Manipulating Materials: Electronic and Topological Properties of Chemically and Structurally Complex Materials

by

Stephanie Alexandra Mack

Doctor of Philosophy in Physics

University of California, Berkeley

Professor Jeffrey B. Neaton, Chair

Electronic structure theory enables fundamental understanding of material properties. Using first-principles based methods, several different classes of complex materials are studied including perovskite oxide heterostructures, halide perovskites, alkali metals under pressure, and high-throughput screening of multiferroic materials.

- In Chapter 2 we discuss the basis of electronic structure methods used in this thesis and introduce the calculation of topological properties from first-principles.
- In Chapter 3 the properties of lithium, an ostensibly simple metal, under pressure are introduced and our explorations into the emergence of nontrivial topological features at high pressures are shown.
- Halide perovskites have emerged as a promising material class for solar energy conversion due to their optoelectronic properties. We explore three different halide perovskite materials and, in collaboration with experiment, develop an understanding of how their properties change through chemical substitutions and structural manipulations. This includes the optoelectronic properties of Sn–alloyed $Cs_2AgBiBr_6$ (Chapter 4) and $Cs_8Au_4XCl_{23}$ (X = In; Bi) (Chapter 6); and the increase in conductivity of $(EA)_2CuBr_4$ through pressure (Chapter 5).
- Similarly, perovskite oxides are a highly tunable class of materials which display a wide range of interesting phenomena. Here we exploit the fact that experimentalists can control the synthesis of perovskite oxide heterostructures at the precision of single atomic layers. Given this level of control, we use first-principles calculations to design monolayers and bilayers that would tune the work function of bulk $SrRuO_3$ for thermionic applications in Chapter 7

- In Chapter 8, we discuss our work developing a high throughput workflow based on symmetry and first-principles calculations to screen tens of thousands of materials for candidates which are both magnetic and ferroelectric.
- Finally, Chapter 9 presents an overview of the work.

To the girls

Contents

List of Figures

List of Tables

Acknowledgments

"You should drink some
bourbon and rethink this"

November 3, 2017

First and foremost, I have to thank Jeff for being a great advisor these past six years. I cannot imagine another group in which the same degree of intellectual freedom to pursue my interests would have been given. Your own breadth of scientific curiosity has been both an inspiration and an aspiration. Beyond that, you've cultivated an inclusive and collaborative group culture, which undoubtedly has been important in my growth as a scientist throughout my time in Berkeley. Even though we did not always agree about the appropriate use of commas and semicolons, there is no perfect grad school experience (also thanks in advance for letting me use your quotes wildly out of context).

Thanks to *all* my favourite postdocs (I admit there was more than one...quelle surprise) for teaching me so much about science, work-life balance, and making time for the important things in life. You are all wonderful role models. All Neatonians past and present deserve my thanks for shaping my grad school experience; I can honestly say that I learned something from every member of the group. I feel very fortunate to have rather surreptitiously found myself as part of an amazing scientific family where kindness and respect are as important as the scientific output. During my Ph.D., there were a few I knew particularly well and want to thank. Guo, for getting me started in the group and teaching me DFT. Michele, my academic big sister, for convincing me to join the group and letting me inherit her desk. Flo, your baking was always more delicious than you advertised. Samia (and Hank), I'm so grateful you've stuck around with me this whole time, especially these past few months, and for having excellent taste in chairs. Sinéad, it's been good craic, thank you for being a great friend and mentor these past few years, and for brightening my walls with your artwork. Tess, thanks for teaching me all I know about workflows and it's been fun watching you find your scientific happy place. Marina, your dedication to science and exploring your surroundings is inspiring and you've been an amazing social catalyst for the group, but I must admit I do not trust you with directions. Sophie, I'm so glad I wasn't the only one learning about topological materials and, more importantly, I could come to you with all my Swedish questions, from buying a book to a turkey. Liz, you impress me so much with your tenacity (not just in terms of running, but I was glad I had a hype partner for the runaround) and I always knew I could call on you when I needed help. Jonah, thank you for always being so calm and supportive, especially in the more stressful parts of this degree, and always being there for a chat or coffee break. Sorry for the many, many hours of tormenting you. Actually, thanks to all Neatonians for putting up with years of mischievousness (as some have put it). Jung-Hoon, buddy, thank you for all the advice and support over the years, especially before quals, and always letting me kill time before group meeting with

you. LINN(!), you always were (and frankly still are) remarkably patient putting up with me, which I appreciate greatly, even if you in turn never fully appreciated my poetry skills.

I've also appreciated the opportunity to collaborate with Professor Hemamala Karunadasa and the current and former members of her group, in particular Kurt and Adam, who have all given me the chance to learn so much about halide perovskites and to think about materials from a different scientific perspective.

Thanks to the Monserrat group (and the KAVLI/Winton Programme for funding my exchange to Cambridge) for providing a most refreshing scientific vacation before the summer of writing began in earnest, it was a breath of fresh air during a stressful year.

Outside of research there are many other people who have been important to me these past few years. Arielle, you've been a steadfast friend this entire time, thanks for never letting me forget how to say pollo and semi-spontaneously hiking Half Dome; thanks to Kelly for being a great gym partner; Halleh, you've always given me lots to think about after our chats; Lizzy, from hosting you as a prospie to now having our coffee catch-ups as fellow grad students, it's been great getting to know you. Thanks to the members of the Science Policy Group, especially Kathy and Andrew, for opening my eyes to a different aspect of science and keeping my Tuesday evenings busy. To the women at Lake Merritt, thanks for letting me play around in boats at 5am again. Thanks to all my ski friends for helping me escape the sunshine to something closer to proper winter weather; although almost making me miss my flight to APS, the powder was worth it.

There are also all of the invisible forces that helped make the process so much easier. Meg Holm, who made me feel welcome from my very first meeting with Jeff and assured me after the second meeting that pictures for the DOE instagram page were not a normal part of life. Thanks to Anne, Claudia, Donna, Kathy, Joelle, and Brian for making campus life easier and Suksham, Laura, Arica, and Marisa for making LBL life easier. Kai Song of hpcshelp, you were magical in solving my computing woes.

Thanks to Mandar and Squishy, for keeping me relatively normal, always being willing to travel, and providing me a home away from home. May we continue to keep pursuing our own dreams and never lose sight of each other. Thanks to Mom, for everything from helping me set up my apartment to always being a phone call away. You sparked my love of learning early on for which I'll always be grateful. I'll do my best to keep picking locations for my next positions that double as nice vacation spots.

At this point, I think the most important lesson learned over these past years has been to always strive to be kind, sincere, and generous with one's time. Science is a wonderful adventure, but is not nearly so much fun without an even more wonderful group of people around you, whether near or far. Thank you.

Chapter 1

Introduction

"This might be a fool's errand...so Stephanie maybe you could try this"

March 24, 2017

The contents of this dissertation use the DFT formalism (as introduced in Chapter 2) to predict novel electronic and topological band structure properties of materials with clear consequences for experimental observables. Modern, advanced electronic structure methods are used to study the band structure – symmetry, topology, and its consequence for optoelectronic properties – of chemically and structurally complex materials away from their bulk ground states. This includes manipulating variables such as pressure and strain at interfaces, and chemically with dopants and defects. We provide an overview of density functional theory, which is the starting point for all our calculations; Berry phases and their manifestations in material properties through the modern theory of polarization and topological properties; and codes that can be used to automate high-throughput calculations.

The advent of these modern computational techniques and databases provide a unique opportunity to both discover and design novel material functionality. Since DFT essentially only requires knowledge of the chemical composition of a material and an initial guess at the atomic positions, it is highly flexible and can be used to calculate many different properties. The structure at a given pressure and temperature determines the other properties of a material [1]. The accuracy of first-principles based DFT calculations will certainly depend on the level of theory used in those calculations (such as the inclusion of relativistic effects, magnetism, and precision of structural relaxations if there are competing structural phases). Furthermore, not all properties are straightforwardly extracted from the output of these calculations and, depending on the properties one wants to compute, extensions beyond standard DFT are necessary.

Macroscopic phenomena of materials often requires atomic scale understanding of the electronic interactions. Recently, it has come to light that beyond the symmetry of the

material, certain phenomena can only be explained with knowledge of the topology of the system as well – these effects include the quantum spin hall effect where there is a quantization of the electronic energy levels and the linear dispersion of graphene and the Dirac-like behavior of the electrons. Topological classification provides an exciting new approach to understand novel properties of materials and another axis of tunability for desired properties. Furthermore, the recent advances made so that one can calculate topological invariants from first-principles allow us to make specific predictions of materials which can host these nontrivial topological properties.

Topological electronic materials exhibit unique properties that arise due to the interplay of symmetry and topology in a crystalline material. Materials which possess the same symmetries can have different topological classifications which results in observable consequences. For instance, at the interface of a topological insulator and vacuum (or a 'normal' (topologically trivial) insulator) there are metallic surface states which necessarily arise due to the interface between two topologically distinct materials. They are characterized by topological invariants, which define to which class of topological materials they belong; furthermore, there are different topological invariants for different classes of topological materials.

In Chapter 3 the properties of lithium, an ostensibly simple metal, under pressure are introduced and our explorations into the emergence of nontrivial topological features at high pressures are shown. Predicting the structure of materials is a difficult challenge because of the sheer size of phase space of all possible configurations for a material. Fortunately, huge advances have been made to make this a more tractable problem and other work has developed techniques to accurately predict the structural evolution of elemental lithium throughout a large pressure range up to 500 GPa [2, 3].

In Chapters 4, 5, and 6 we explore three different halide perovskite materials and, in collaboration with experiment, develop an understanding of how their properties change through chemical substitutions and structural manipulations. This includes the optoelectronic properties of $Cs_2AgBiBr_6$ and $Cs_8Au_4XCl_{23}$ (X = In; Bi); and the conductivity of $(EA)_2CuBr_4$ through pressure. Perovskite structures ABX_3 can host myriad phenomena depending on the transition metals on the A and B sites. Halide perovskites, (where X = F, Cl, Br, I), are a particularly exciting field of research for optoelectronic applications. Beyond the typical plethora of inorganic substitution options for the A and B sites, interestingly the structure can also have small organic molecules on the A site known as a hybrid organic-inorganic perovskite, or a hybrid-halide perovskite, as depicted in Figure 1.1. One such material of great interest is $MAPbI_3$ (MA = methyl ammonium) which was shown to have a nearly ideal band gap for solar applications. Furthermore, the efficiency of halide perovskite based devices have reached the same level as silicon in only just over a decade of research. The Pb cation in $(MA)PbI_3$ is of concern, since it can decompose into water soluble lead salts, which is not ideal for applications, but is highly suggestive that derivatives of this structure would be similarly promising. For solar applications a band gap around 1.4 eV is ideal, however finding a material with a gap of 1.6 eV would still be very impactful in improving solar capture efficiency [4].

There has been much research in substituting both the A and B sites in halide perovskites.

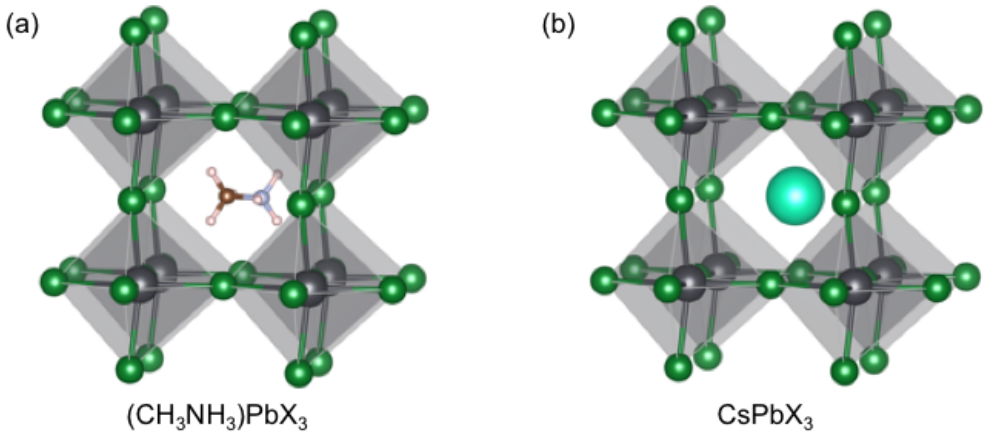

Figure 1.1: Here we show two examples of halide perovskites of the form ABX_3 where X is a halide (such as Cl, Br, or I). In panel a) we are showing an example of a halide perovskite with an organic cation on the A–site, whereas in panel b) this can be replaced by an inorganic cation such as Cs which has a similar size to the methylammonium molecule. This enables even more diverse substitutional options in this class of materials.

Replacing the Pb, nominally in a 2+ oxidation state, which is on the B-site, is of high priority, and both isovalent and heterovalent direct substitutions have been extensively explored. Another recent approach is to double the unit cell, $A_2BB'X_6$, so as to have two different cations replace Pb, and one such example $Cs_2AgBiBr_6$ was recently synthesized [5, 6, 7] and shown to have improved stability in air and water as compared to $MAPbI_3$. However, it has an indirect band gap of over 1.8 eV which is too large to be an improvement over other halide perovskites for solar applications. Therefore, we seek to further alloy the system to design a material with a smaller, direct band gap inspired by prior work looking at Tl as a substitute [8]. In this work we examine Sn as a heterovalent substitute in the double perovskite $Cs_2AgBiBr_6$ as elucidated further in Chapter 4 in collaboration with experiment [9].

As for the A-site, larger organic molecule can be incorporated on it in which case the layered perovskite compound can be considered as a quasi-2D material, since the organic linker molecules physically separate the 2D layers of inorganic octahedra. The organic linkers can have significant impact on the connectivity and structural distortions of the inorganic 2D layers, therefore greatly affecting their macroscopic properties. Beyond optoelectronic properties, prior work has shown that with an applied pressure of 51 GPa (EDBE)$CuCl_4$ (EDBE = 2,2-(ethylenedioxy)bis(ethylammonium)) shows orders of magnitude increase in its conductivity. Here we study a similar compound, $(EA)_2CuBr_4$, where the Cl has been replaced by Br and similar organic molecules are on the A sites, which experimentally was shown to exhibit and order of magnitude higher conuctivity with only 2.6 GPa of pressure than the $CuCl_4$ material, as expanded in Chapter 5.

There is a truly astonishing number of halide perovskites and as synthesis yields more interesting structures, one difficulty is deciding what is still considered a 'perovskite' structure as well as the dimensionality, i.e. at which point the material is described as quasi-2D versus 3D; these points are still under debate in the literature (and social media [10]). As such, we adopt a fairly loose definition of the perovskite structure, but generally consider it to be perovskite so long as there are corner sharing BX_6 octahedra. The third halide perovskite system studied also demonstrates the flexibility of chemical substitutions possible within the perovskite framework in Chapter 6. In all three systems, first-principles calculations allow us to better understand the effect of chemical and structural motifs on their optoelectronic and transport properties in collaboration with experimental results.

Similarly, perovskite oxides are a highly tunable class of materials which display a wide range of interesting phenomena. Here we exploit the fact that experimentalists can control the synthesis of perovskite oxide heterostructures at the precision of single atomic layers. Given this level of control, we use first-principles calculations to design monolayers and bilayers that would tune the work function of bulk $SrRuO_3$ for thermionic applications in Chapter 7.

Another property which perovskite oxides can have is ferroelectricity, in which it is a polar material with a switchable polarization. Materials which simulatneously display for than one ferroic ordering – ferroelectricity, ferromagnetism, or ferroelasticity – are termed multiferroics. Expanding the catalogue of multiferroics has thus far mostly relied on finely tuning complex perovskite oxides through strain engineering and chemical substitution. While this has been a successful strategy yielding over a dozen new bulk perovskite oxide multiferroics, few new classes of multiferroics have been discovered as typical strategies rely on knowledge of structural motifs of known multiferroics. Prior work [11] has developed a high-throughput workflow to screen the Materials Project database for ferroelectrics based on space group symmetry requirements and *ab initio* calculations. In Chapter 8, we discuss our work developing a high throughput workflow based on symmetry and first-principles calculations to a materials database for candidate polar insulating materials which are both magnetic and ferroelectric.

Chapter 2

Methods

"We're after the truth, or whatever"

October 20, 2017

This thesis uses density functional theory (DFT), and associated methods. In what follows, I will briefly review DFT and aspects of modern practical implementations of DFT used in this thesis for understanding and predicting phase behavior and electronic structure of complex materials.

Density Functional Theory

The focus of this dissertation is condensed matter physics and the electronic structure of crystalline solids. Fundamentally, solids consist of on the order of 10^{23} interacting electrons and nuclei. The Hamiltonian for this fully interacting system can be written as

$$\mathcal{H} = -\frac{1}{2}\sum_i \nabla_i^2 + \frac{1}{2}\sum_i \sum_{j\neq i} \frac{1}{|\mathbf{r}_i - \mathbf{r}_j|} - \frac{1}{2}\sum_i \frac{1}{m_\alpha}\nabla_\alpha^2 + \frac{1}{2}\sum_\alpha \sum_{\beta\neq\alpha} \frac{Z_\alpha Z_\beta}{|\mathbf{R}_\alpha - \mathbf{R}_\beta|} - \sum_i \sum_\alpha \frac{Z_\alpha}{|\mathbf{r}_i - \mathbf{R}_\alpha|} \tag{2.1}$$

where the i, j denote electronic, and α, β the nuclear, degrees of freedom. In what follows, we use the Born-Oppenheimer approximation, namely we neglect the nuclear kinetic energy, and assume the ions are fixed at their lattice sites, where they generate a static potential for the electrons.

DFT is a widely-used method to calculate properties of atoms, molecules, solids, surfaces, interfaces, and more. This is because it provides a rigorous, exact way of mapping a problem with interacting particles to a non-interacting problem. The basis of this is given by the Hohenberg-Kohn [12] theorems and Kohn-Sham [13] ansatz, described below largely following the descriptions from [14, 1].

The first Hohenberg-Kohn theorem states that for a system of interacting particles in an external potential, that external potential is *uniquely* determined by the ground state

density (and thus the total energy is a unique functional of the ground state density alone). The second Hohenberg-Kohn theorem states that for a given external potential, a functional for the energy in terms of density can be defined. The ground state energy is then the global minimum of that energy functional, and the density that minimizes E$[n(r)]$ is then the exact ground state density. Although these theorems prove that such a functional exists, the remaining question is the form of that functional.

These theorems imply that the ground state energy, E_0, of an interacting system in an external potential V_{ext} is the energy that minimizes a functional, $E[\rho(\mathbf{r})]$, as given below, with respect to the density ρ.

$$E[\rho(\mathbf{r})] = F[\rho(\mathbf{r})] + \int \rho(\mathbf{r}) V_{ext}(\mathbf{r}) d^3\mathbf{r} \tag{2.2}$$

which in principle can be solved exactly by minimizing the energy with respect to the electron density $\rho(\mathbf{r})$.

Density functional theory potentially represents a simplification relative to wavefunction-based theory, as it replaces the wavefunction, a function of 3N coordinates, with the density, a function of three, as the fundamental variable. However, the exact functional of the density is unknown. To make progress, Kohn and Sham partitioned the functional into non-interacting and interacting parts, with the non-interacting part being known. This lead to the Kohn-Sham equations, a major breakthrough in DFT and the reason that it is still used today.

The Kohn-Sham equation shows that one can construct a non-interacting electron system that has the same density as the interacting system of interest; since it was already shown that a given density provides a unique external potential, therefore solving the electronic problem of an equivalent non-interacting system with the same density will give the external potential for the interacting system, thereby greatly simplifying the problem by solving the fictitious, non-interacting electronic system. While the functional in Eqn. 2.2 $F[\rho(\mathbf{r})]$ is not known exactly it can be broken into three terms, two of which we know the exact form and one which remains unknown.

$$F[\rho(\mathbf{r})] = T_s[\rho(\mathbf{r})] + \frac{e^2}{2} \iint \frac{\rho(\mathbf{r})\rho(\mathbf{r}')}{|\mathbf{r} - \mathbf{r}'|} d^3\mathbf{r} d^3\mathbf{r}' + E_{XC}[\rho(\mathbf{r})]. \tag{2.3}$$

The first term is just the kinetic energy of the non-interacting electrons; the second is the electron-electron Hartree interaction. The third term is the exchange-correlation functional and this is the term in which approximations must be made since the exact form of it remains unknown.

The electron density is $\rho(\mathbf{r}) = \sum_i |\psi_i(\mathbf{r})|^2$ which leaves the kinetic energy term as

$$T_s[\rho(\mathbf{r})] = \sum_i -\frac{\hbar^2}{2m_e} \int \psi_i^* \nabla^2 \psi_i d^3\mathbf{r}. \tag{2.4}$$

Minimizing the energy with respect to the electron density leaves us with a one-particle Schrödinger equation. Minimizing the density leads to an equation of the form 2.5, with the eigenvalues really Lagrange multipliers, enforcing the constraint of 2.4

$$\left(-\frac{\hbar^2}{2m_e}\nabla^2 + V_{eff}(\mathrm{r})\right)\psi_i(\mathrm{r}) = \epsilon_i\psi_i(\mathrm{r}) \tag{2.5}$$

where V_{eff} is the effective one-body potential

$$V_{eff} = V_{ext}(\mathrm{r}) + \int \frac{e^2 n\left(\mathrm{r}'\right)}{|\mathrm{r}-\mathrm{r}'|} d^3\mathrm{r}' + V_{XC}(\mathrm{r}) \tag{2.6}$$

given in terms of the exchange-correlation potential

$$V_{\mathrm{xc}}(\mathbf{r}) = \frac{\delta E_{\mathrm{xc}}[\rho(\mathbf{r})]}{\delta\rho(\mathbf{r})}. \tag{2.7}$$

The exchange-correlation potential is still unknown. The first approximation in the Kohn-Sham formalism to the exchange-correlation energy is the local density approximation (LDA) [15], which has shown to work decently well in capturing material properties, which was not obvious at the time and remains surprising,

$$E_{XC}^{\mathrm{LDA}} = \int \varepsilon_{XC}(\rho(\mathbf{r}))\rho(\mathbf{r})d^3\mathbf{r}. \tag{2.8}$$

One can also include the gradient of the electron density in the generalized gradient approximation (GGA), a commonly used one being PBE as developed by Perdew, Becke, and Ernzerhof [16], which also works quite well,

$$E_{\mathrm{XC}}^{\mathrm{GGA}} = \int d^3 r e_{\mathrm{XC}}^{\mathrm{GGA}}\left(n_\uparrow(\mathbf{r}), n_\downarrow(\mathbf{r}), |\nabla n_\uparrow(\mathbf{r})|, |\nabla n_\downarrow(\mathbf{r})|\right) \tag{2.9}$$

Alternatively, one can include a fraction of exact exchange defined as

$$E_{\mathrm{X}} = -\frac{1}{2}\sum_{\sigma,i,j}\int d^3 r \int d^3 r' \frac{\phi_{i\sigma}^*(\mathbf{r})\phi_{j\sigma}^*\left(\mathbf{r}'\right)\phi_{i\sigma}\left(\mathbf{r}'\right)\phi_{j\sigma}(\mathbf{r})}{|\mathbf{r}-\mathbf{r}'|} \tag{2.10}$$

in the so-called hybrid functionals. This can be partitioned into long-range (LR) and short-range (SR) contributions such as is done in the HSE functional [17] (named for Heyd, Scuseria, and Ernzerhof) where a fraction of exact exchange (here $a = 1/4$, the separation range is determined by the screening parameter ω which is determined from perturbation theory) is included only for short-range interactions

$$E_{XC}^{\mathrm{HSE}} = aE_X^{\mathrm{HF,SR}}(\omega) + (1-a)E_X^{\mathrm{PBE,SR}}(\omega) + E_X^{\mathrm{PBE,LR}} + E_C^{\mathrm{PBE}}. \tag{2.11}$$

In order to proceed with solving the self-consistent Kohn-Sham equations, one needs to choose a basis set with which to represent the electronic wavefunctions. The materials

studied in this dissertation are those which possess discrete translational symmetry, and as such we use a plane-wave basis set representation.

The periodicity of the lattice allows us to use Bloch's theorem [18] to write the wavefunctions as a phase factor multiplied by a cell periodic function $u_{n\mathbf{k}}(\mathbf{r}) = u_{n\mathbf{k}}(\mathbf{r}+\mathbf{R})$, for crystal momentum $\mathbf{k}$ and band index n,

$$\psi_{n\mathbf{k}}(\mathbf{r}) = e^{i\mathbf{k}\cdot\mathbf{r}} u_{n\mathbf{k}}(\mathbf{r}). \tag{2.12}$$

In this work, we primarily use plane wave basis functions, summing over reciprocal lattice vectors $\mathbf{G}$,

$$u_{n\mathbf{k}}(\mathbf{r}) = \sum_{\mathbf{G}} c_{n,\mathbf{k}}(\mathbf{G}) e^{i\mathbf{G}\cdot\mathbf{r}}. \tag{2.13}$$

In principle plane waves are a complete basis but an infinite number are required. In practice only a finite number is necessary, given by an energy cutoff; we check the convergence of our results with respect to this cutoff (where m_e is the electron mass)

$$\frac{\hbar^2|\mathbf{k}+\mathbf{G}|^2}{2m_e} \leq E_{cutoff}. \tag{2.14}$$

It is worth noting that the formulation of DFT is exact for the ground state of the system, and furthermore only the charge density and total energy equate to that of the physical, interacting system. As such, the eigenvalues of the Kohn-Sham equation are not meant to accurately represent quasiparticle excitations with this formalism, nor the electronic band gap. The single-particle eigenvalues calculated in DFT are not physically meaningful; corrections to those single-particle energies require beyond standard DFT formalisms, like the GW approach, which includes first-order self-energy corrections. This is beyond the scope of this dissertation.

Many material properties are determined by the valence electrons, and these valence electrons are largely decoupled from the core electrons for the most part under ambient conditions. One caveat is that this needs to be checked more carefully for materials subjected to high pressures, where the atomic cores are very close together and indeed core overlap can strongly influence material properties (as further discussed in Chapter 3). Barring high pressure situations, we can simplify the representation of the electronic wavefunction by using pseudopotentials, wherein the basis sets do not explicitly treat the core electrons.

The periodicity of the lattice is particularly useful for bulk crystalline solids, but when one wants to study surfaces or defects in a crystalline solid we must work around the periodic plane wave approach by use of supercells. For the former case, one can still impose in-plane periodicity but include a finite amount of vacuum in the out-of-plane direction, enough such that the periodic representations of the slabs (the crystal of finite thickness that is periodic in-plane) do not interact and the slab is thick enough that the interior converges to bulk-like properties, as further discussed in Chapter 7. For the latter case, one can create the desired defect (atomic substitution, vacancy, etc.) in a new unit cell that is simply $n_i \times n_j \times n_k$

repetitions of the original unit cell of the crystal. One actually has to use large supercells and check that artifacts associated with periodicity are avoided as best as one can while maintaining the concentration of defects needed, as further discussed in Chapter 4. The defects can be charged or neutral, though in this work we only consider neutral defects.

Although so far we have used the reciprocal space representation for the wavefunctions, one can define a real space representation as well and one such example are Wannier functions [19]. The Wannier functions $w_{n\mathrm{R}}$ are defined as Fourier transforms of the Bloch wavefunctions $\psi_{n\mathrm{k}}$ and vice versa as shown below

$$|w_{n\mathbf{R}}\rangle = \frac{\Omega}{(2\pi)^3} \int_{\mathrm{BZ}} e^{-i\mathbf{k}\cdot\mathbf{R}} |\psi_{n\mathbf{k}}\rangle \, d^3k \tag{2.15}$$

$$|\psi_{n\mathbf{k}}\rangle = \sum_{\mathbf{R}} e^{i\mathbf{k}\cdot\mathbf{R}} |w_{n\mathbf{R}}\rangle \tag{2.16}$$

where the integrals are performed over the Brillouin zone, n is the band index, $\mathbf{R}$ are the lattice vectors, $\mathbf{k}$ are the wave vectors, and Ω is the unit cell volume. These form a complete, orthonormal basis, and each Wannier function is localized around $\mathbf{R}_j$; these are not uniquely defined as one can include a phase factor to achieve so-called maximally localized Wannier functions [20]. Calculating these are well integrated within Wannier90 [21] (an open-source code which computes the maximally-localized Wannier functions from the Bloch wavefunctions calculated with DFT) which interfaces with many commonly used electronic structure theory codes and are furthermore very useful for calculation of topological invariants as further discussed in the following section and in Chapter 3.

Topological materials from an electronic structure perspective

As discussed in the introduction, topological electronic materials are classified by topological invariants. In the case of topological insulators mentioned above, the topological invariant is the $\mathbb{Z}_2$ index. It takes on a value of 1 for a topologically nontrivial insulator and 0 for a topologically trivial insulator (i.e. topologically equivalent to vacuum). Due to the bulk-boundary correspondence, the topological invariant can be defined in terms of a bulk or surface property of the material. From the bulk properties the $\mathbb{Z}_2$ index can be defined in terms of the Berry phase of the Bloch wavefunctions as outlined below. If the crystal has inversion symmetry, the calculation of the $\mathbb{Z}_2$ index can actually be greatly simplified because the Bloch wavefunctions at the time-reversal invariant momenta (TRIM) of the Brillouin zone, which are invariant under inversion and time reversal symmetry, have well-defined parities; therefore the $\mathbb{Z}_2$ index can be calculated from the products of the parity eigenvalues of the occupied bands at the TRIM [22].

More generally, these invariants are related to the Berry phase of the Bloch wavefunctions and can be calculated from first-principles calculations of materials. In fact, the Wannier charge centers can be shown to be proportional to the Berry phase of the Bloch wavefunctions

$$\langle w_{n0}|\mathbf{r}|w_{n\mathbf{R}}\rangle = \mathbf{A}_{n\mathbf{R}}, \tag{2.17}$$

where the left hand side is the definition of the Wannier charge centers $\bar{\mathbf{r}}_n$, and with the $\mathbf{A}_{n\mathbf{R}}$ being the Fourier transform coefficients of the $\mathbf{A}_{n\mathbf{k}}$, the Berry connection which was defined in reciprocal space.

$$\mathbf{A}_{n\mathrm{R}} = \frac{V_{\mathrm{cell}}}{(2\pi)^3}\int_{\mathrm{BZ}} e^{-i\mathbf{k}\cdot\mathbf{R}}\mathbf{A}_n(\mathbf{k})d^3k. \tag{2.18}$$

The Bloch function is written as

$$\phi_n = \oint \mathbf{A}_n(\mathbf{k})\cdot d\mathbf{k}, \tag{2.19}$$

in terms of the Berry connection $\mathbf{A}_n$

$$\mathbf{A}_n(\mathbf{k}) = \langle u_{n\mathbf{k}}|\, i\nabla_{\mathbf{k}}|u_{n\mathbf{k}}\rangle. \tag{2.20}$$

In this way, the Wannier charge centers are directly proportional to the Berry phase; a phase going from 0 to 2π simply corresponds to a Wannier charge center going across the unit cell in one lattice direction, from 0 to a. One may be concerned, since the Wannier functions are not uniquely defined, if there is ambiguity in this definition, but the Wannier charge centers are uniquely defined up to a lattice vector, in complete analogy to a phase being defined modulo 2π, or the electronic polarization being defined modulo a quantum of polarization [23, 24, 25, 26, 27, 28, 29, 30].

The invariant is slightly more complicated when studying topological semimetals, instead of the $\mathbb{Z}_2$ invariant, the Chern number is the invariant. Topological Dirac (Weyl) semimetals are ones in which there are linearly dispersing bands with fourfold (twofold) degenerate crossing points.

The hybrid Wannier charge centers (these are wavefunctions which are Wannier-like along x-direction, and Bloch-like along y and z)

$$\bar{x}_n\left(k_y\right) = \frac{ia_x}{2\pi}\int_{-\pi/a_x}^{\pi/a_x} dk_x \left\langle u_{nk}\left|\partial_{k_x}\right|u_{nk}\right\rangle, \tag{2.21}$$

where $\bar{x}_n$ are assumed to be smooth functions of k_y for $k_y \in [0, 2\pi]$, can be used to express the polarization.

As alluded to above, the electric polarization is written in terms of Berry phase of Bloch wavefunctions

$$P_e^h\left(k_y\right) = e\sum_n \frac{ia_x}{2\pi}\int_{-\pi/a_x}^{\pi/a_x} dk_x \left\langle u_{nk}\right|\frac{\partial_{k,x}u_{nk}}{\partial k}\Big\rangle = e\sum_n \bar{x}_n\left(k_y\right). \tag{2.22}$$

In this case, we use P_e^h for the hybrid electronic polarization because we are only Wannierizing along one direction, the other two directions remain Bloch-like (so the wavefunctions are expressed as a "hybrid" of Wannier and Bloch states).

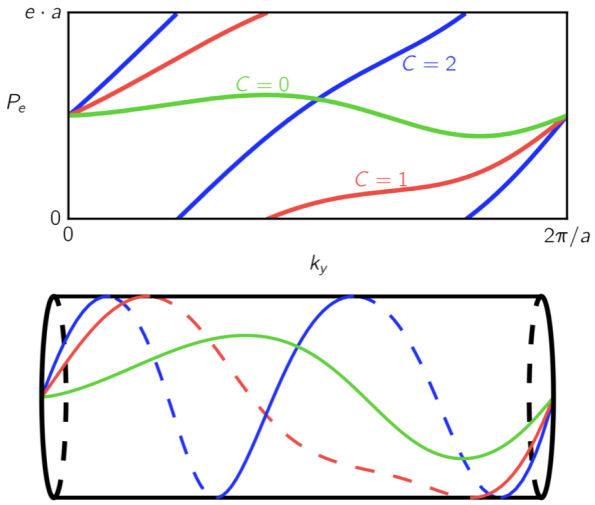

Figure 2.1: Adapted from [32]. This illustrates different windings of the WCC that are possible while traversing along the periodic direction in the Brillouin zone denoted by k_y. The winding is illustrated by taking the polarization axis (the vertical axis in the top figure) and forming a cylinder since it is defined modulo 2π.

The topological invariant is related to polarization [31, 32]

$$C = \frac{1}{ea}\left(P_e^h\left(k_y = 2\pi/a\right) - P_e^h\left(k_y = 0\right)\right), \tag{2.23}$$

where C is the Chern number, P_e^h denotes the hybrid electronic polarization. One can then track the hybrid Wannier charge centers along closed path in Brillouin zone (chosen depending on geometry of topological features) and the winding of the WCCs gives the Chern number as depicted in Fig. 2.1; note that in three dimensions the Chern number can be defined on any closed 2D cut through the Brillouin zone [32].

In addition to calculating the topological invariant, from a materials perspective it is important to also understand what gives rise to the topological features and how they are protected. Broadly speaking, one can divide topologically nontrivial materials into spin-orbit induced or crystalline topological materials. In the former case, spin-orbit coupling causes a reordering of the electronic bands such that one cannot adiabatically evolve the Hamiltonian between the normally ordered and inverted band structures without the energy gap closing (this is the case in such materials as Bi_2Se_3). In the latter case, crystalline symmetries give rise to band degeneracies which become nondegenerate when that symmetry is broken. By understanding the protection mechanism of these topological features, one can then manipulate and design materials to have these features.

Chapter 3

Emergence of topological phases of elemental lithium under pressure

"Put on Patti Smith and finish the lithium draft"

October 15, 2017

This chapter is primarily adapted from [33]

3.1 High pressure lithium

Lithium is the lightest metal on the periodic table, under ambient conditions, and, unusually, it undergoes structural phase transitions to *lower* symmetry structures under pressure. We studied the electronic structure of these high pressure phases of lithium using density functional theory calculations. At 80 GPa, where lithium is predicted to assume *Pbca* symmetry, we find it also becomes topologically nontrivial, with the electrons behaving as massless fermions. Lithium is unique as a topological material in that it is a light elemental solid where the topological features of the band structure are well-isolated from other bands at the Fermi level. Our results indicate that lithium has previously unexplored topological properties in its pressure phase diagram.

Lithium assumes a close-packed structure under ambient conditions and is a simple metal with a free electron-like band structure. More than a decade ago, it was predicted using first-principles calculations that, somewhat counter-intuitively, as the pressure increases and the average electron density rises lithium undergoes a sequence of phase transitions in which the coordination number decreases and the electronic structure strongly deviates from that of a simple metal, culminating in an insulating or zero-gap semiconducting state around 100 GPa [34]. This series of phase transitions was attributed to a Peierls-like set of symmetry-lowering distortions. Core overlap forces electron density to reside in the increasingly open interstitial

regions [35], lowering electronic kinetic energy and explaining the s-to-p transition [36] in the character of the band structure near the Fermi energy [37]. Interestingly, the initially-predicted zero-gap phases exhibited a nonsymmorphic space group, *Cmca*, and the broad linear dispersion in the band structure [34] is indicative of massless Dirac fermionic behavior. In this paper we characterize the predicted high pressure structures to feature isolated Dirac nodes at the Fermi energy with band velocities comparable to graphene [38, 39].

Since the original predictions nearly two decades ago[34], experiments have confirmed the basic idea that lithium exhibits lower coordinated structures with pressure, albeit with different structures. At around 40 GPa, lithium is found to transform from close-packed fcc to a lower symmetry $I\bar{4}3d$ [40] phase in which the atoms are only three-fold coordinated. Subsequent *ab initio* calculations [41, 2] and experiments [42] have shown this three-fold coordination persists in a series of different structural phases, with nonsymmorphic symmetries, up to pressures of at least 450 GPa. Although Li is the third-lightest element in the periodic table, with negligible spin-orbit coupling, the sequence of low-symmetry structures assumed as a function of pressure are mostly nonsymmorphic space groups, which promote band sticking, increasing the likelihood of nontrivial topology and hosting novel band structure features.

Experimental determination of the high-pressure structures of lithium is challenging for diffraction experiments due to its small atomic number (Z = 3). In fact, only four lower-pressure structural phases ($Im\bar{3}m$, $Fm\bar{3}m$, $I\bar{4}3d$, *Aba2*) have been experimentally confirmed. Beyond 70 GPa, although the Pearson class has been determined experimentally, the full crystallographic symmetry of the high pressure phases is not yet known [42]. Based on the Pearson class and using first-principles calculations, two prior studies [3, 2] used structure searching algorithms to determine the low-enthalpy space group symmetries at a range of pressures and predicted the zero-temperature phase diagram of lithium from 0 to 500 GPa. We adopt structures from one of these studies [3], which is in good agreement with an earlier independent study by Pickard and Needs [2]; the difference between the two studies is that Ref. [3] predicts two intermediary structures at 71 and 227 GPa, not reported in [2]. Starting with atomic coordinates from [3], we use structures at a representative pressure in the predicted phase diagram (see A), and then use DFT to compute and analyze their electronic structure. All DFT calculations are performed within the local density approximation (LDA) with PAW potentials treating all three electrons in Li as valence using the VASP code [43, 44]. We use the post-processing software Z2Pack [32, 31] and WannierTools [45] to compute topological invariants and surface states, and to determine whether a given phase is topologically trivial or nontrivial.

There has been considerable recent interest in understanding the phases of crystalline materials in terms of their topology as well as symmetry. This has led to the classification of new topological ground states, including topological insulators [46], Dirac/Weyl semimetals [47, 48, 49], and Dirac/Weyl nodal semimetals [50], signatures of which have subsequently been observed in experiments. Structural phases with topological electronic structure have a host of interesting properties, including high mobilities, giant magnetoresistance, and chiral anomalies. Thus far, the majority of materials identified or verified experimentally that

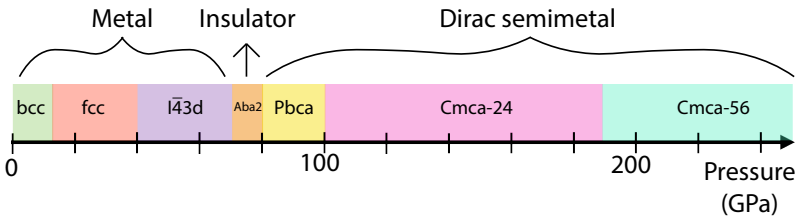

Figure 3.1: Predicted phase diagram of Li below 250 GPa from [3] at zero temperature. Note that from 100–165 GPa lithium assumes a *Cmca* unit cell with 24 atoms per unit cell, and a 56 atom unit cell from 165–220 GPa, after which $P4_2/mbc$ is the preferred space group.

have topological electronic structures are binary or ternary compounds that include heavy elements [51]. Some elemental systems have also been predicted to exhibit topological nodal line properties at standard or high pressures, including Ca, Sr, Y [52], Be, Mg [53], and even the lightest elemental solid, H [54, 55]. Yet, the majority of these elemental solids do not exhibit topological features at the Fermi energy and, if they do, these features are impeded by trivial bands.

3.2 Characterizing high pressure phases of lithium

Experimental determination of the high-pressure structures of lithium is challenging for diffraction experiments due to its small atomic number (Z = 3). In fact, only four lower-pressure structural phases ($Im\bar{3}m$, $Fm\bar{3}m$, $I\bar{4}3d$, *Aba2*) have been experimentally confirmed. Beyond 70 GPa, although the Pearson class has been determined experimentally, the full crystallographic symmetry of the high pressure phases is not yet known [42]. Based on the Pearson class and using first-principles calculations, two prior studies [3, 2] used structure searching algorithms to determine the low-enthalpy space group symmetries at a range of pressures and predicted the zero-temperature phase diagram of lithium from 0 to 500 GPa. We adopt structures from one of these studies [3], which is in good agreement with an earlier independent study by Pickard and Needs [2]; the difference between the two studies is that Ref. [3] predicts two intermediary structures at 71 and 227 GPa, not reported in [2]. Starting with atomic coordinates from [3], we use structures at a representative pressure in the predicted phase diagram (see Appendix A), and then use DFT to compute and analyze their electronic structure. All DFT calculations are performed within the local density approximation (LDA) with PAW potentials treating all three electrons in Li as valence using the VASP code [43, 44]. We use the post-processing software Z2Pack [32, 31] and WannierTools [45] to compute topological invariants and surface states, and to determine whether a given phase is topologically trivial or nontrivial.

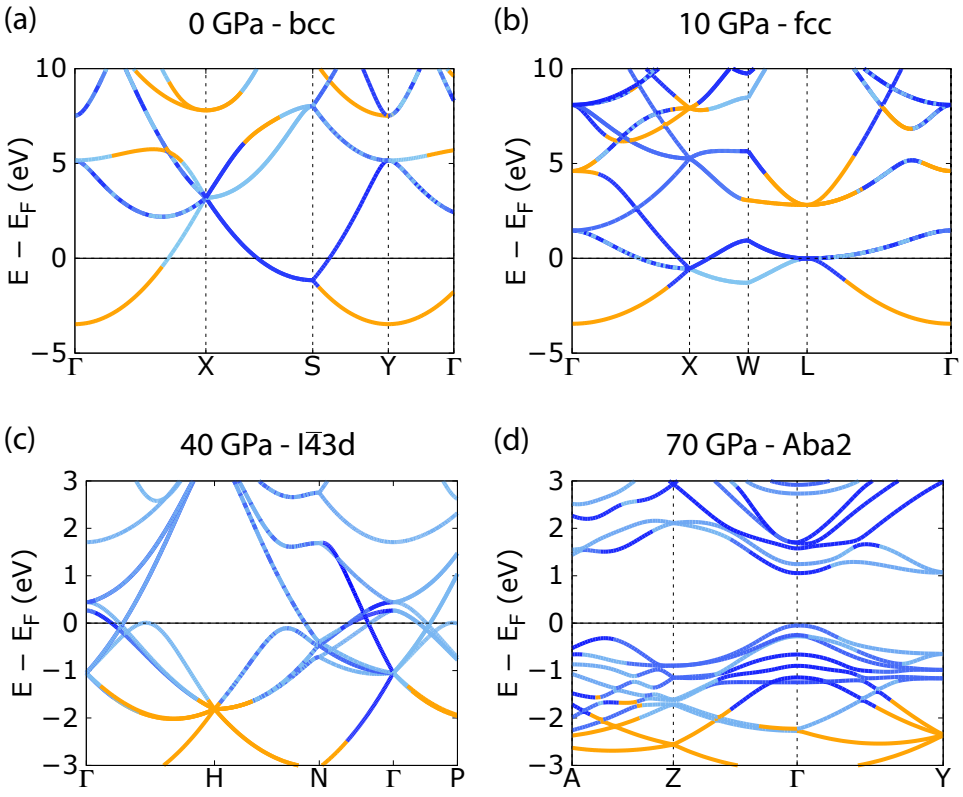

Figure 3.2: Band structures for four lowest pressure predicted structures. The colors indicate the dominant orbital contribution to the band, with the s, p_x, p_y, and p_z orbitals represented by orange, light, medium, and dark blue respectively. The Fermi level is set to zero.

Calculating topological invariants from first-principles

The calculations of the topological invariant are performed using Z2Pack [32]. The *Aba2* structure does not have inversion symmetry, and so the $\mathbb{Z}_2$ index is calculated using Z2Pack, where the invariant is well-defined on the time-reversal symmetric planes, and we calculate the adiabatic pumping of the Wannier charge centers along lines across the planes of the Brillouin zone surfaces. Performing these surface calculations the $\mathbb{Z}_2$ index is calculated to have a trivial value of zero, indicating that the *Aba2* structure is a topologically trivial insulator. In the case of *Pbca*, the winding number of the Berry phase is defined on a smooth contour enclosing the topological nodal ring, and so a torus was parametrized to enclose the nodal ring centered at $k_x = 0$; $k_y = 0.595$ Å^{-1}; $k_z = 0$. We can control the number of lines on the surface in k-space along which the Wannier charge centers are calculated, denoted as num_lines in Z2Pack, and here to ensure convergence we begin with a minimum value of 101 and our tolerance for the distance between the largest gap and the neighboring Wannier

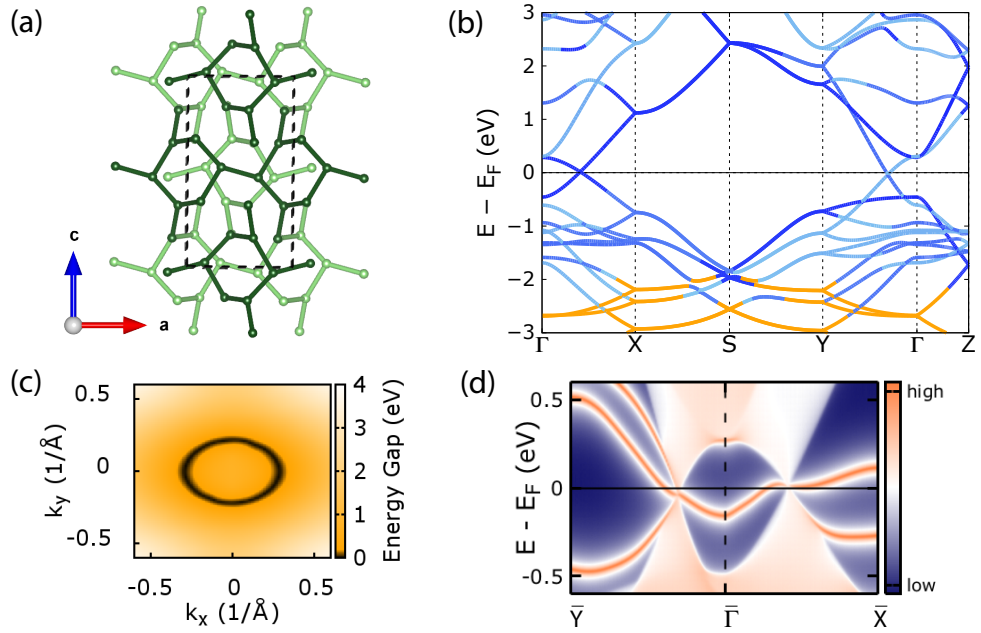

Figure 3.3: Solid Li at 80 GPa in its predicted *Pbca* phase. (a) *Pbca* unit cell - coloring indicates different atomic layers along the *b* direction. (b) Band structure at 80 GPa, where the colors indicate the dominant orbital contribution to the band, with the s, p_x, p_y, and p_z orbitals represented by orange, light, medium, and dark blue respectively. The Fermi energy is set to 0 eV and marked by a black line. (c) The nodal ring is shown in the $k_z = 0$ plane where the color gradient represents the size of the band gap in eV. The projection of the Fermi surface on the 2D k-plane indicates there is a nodal ring in the k_z=0 plane (d) The projected band structure along the [001] direction.

charge center is set to 0.001 $Å^{-1}$, as implemented in the TBModels package (in Z2Pack) with the tight-binding parameters calculated from Wannier90.

Although solid lithium is metallic [56] and considered nearly-free-electron-like at low pressures, between 70-80 GPa it is predicted to adopt the *Aba2* phase, which is predicted to be insulating (see Fig. 3.1). Using Z2Pack, we compute *Aba2* to be topologically trivial with a $\mathbb{Z}_2$ index of zero. At 80 GPa, a transition to the semimetallic *Pbca* phase is predicted; the crystal structure of *Pbca* at 80 GPa is shown in Fig. 3.3(a). Our calculated DFT band structure for *Pbca* at 80 GPa (see Fig. 3.1 for lattice parameters) features two four-fold degenerate Dirac points at the Fermi energy located along the Γ–X and Γ–Y directions as shown in Fig. 3.3(b). Interestingly, these Dirac points are isolated from other bands. At the Dirac points (and away from the Fermi level at X and Y) we observe 'band sticking' [57], or band degeneracies, enforced by the nonsymmorphic symmetries in the *Pbca* space group. Similar band degeneracies arise in the electronic structure of lithium at lower pressure in the $I\bar{4}3d$ phase, which is also nonsymmorphic. However, the eight-fold degeneracies at the

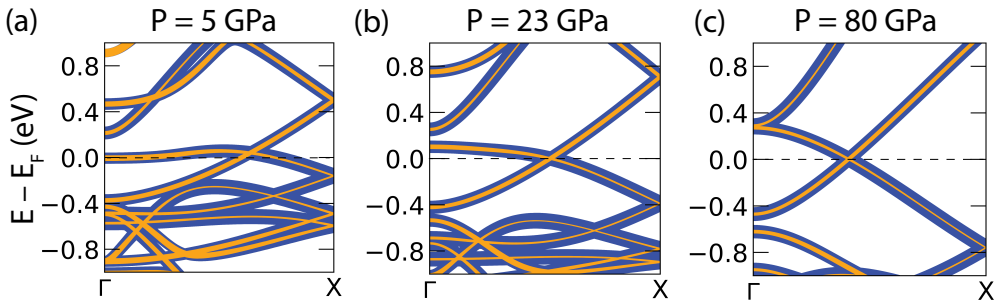

Figure 3.4: Band structures computed with DFT-LDA for bulk *Pbca* phase shown in order of increasing pressure from (a) 5 GPa through to (c) predicted pressure where the space group is stable at 80 GPa. The relative orbital contribution to the bands is shown where s-like is in orange and p-like in blue. Increasing pressure shows increasing p character in the bands at the Fermi level, the s-like contribution decreases from ∼30% to 10% comparing (a) and (c). Along with the broadening of bands this gives rise to a well-isolated Dirac crossing. A similar transition is seen along the Γ–Y direction.

H point, predicted in the band structure of any crystal with $I\bar{4}3d$ symmetry [58], are far below the Fermi energy and topologically-trivial nearly-free electron-like bands dominate the electronic structure at the Fermi level.

Our computed Fermi surface of the *Pbca* phase at 80 GPa appears in Fig. 3.3(c). The fourfold degenerate Dirac points form part of a nodal ring located at the Fermi energy in the k_z=0 plane of the Brillouin zone, enforced by the glide plane $\{2_{001} \text{ — } ½\ 0\ ½\}$ (in Seitz notation). Our calculations predict that the nodal ring is well-isolated from the nearest bands over a broad energy range of 0.8 eV. We verify that the nodal ring is protected by a nonzero Berry phase (winding number = –1), and therefore it is topologically nontrivial. The Fermi velocities, computed with DFT-LDA, range from 2.8–6.6x10^5 m/s, comparable to measured values for other verified Dirac semimetals, such as Na_3Bi [59] and Cd_3As_2 [60]. Topologically nontrivial electronic bands will lead to unique surface states arising from the bulk topological features. Although such surface states would be ostensibly challenging to probe experimentally, our DFT calculations of the *Pbca* (001) surface-projected band structure (Fig. 3.3(d)) verify the existence of the expected drumhead surface state bands connecting the bulk Dirac points [61, 62].

That high-pressure phases of solid Li possess topological band structures with pressure is notable, given its low atomic number. From a geometric perspective, we note that the *Pbca* structure can be viewed as consisting of distorted honeycomb layers, in approximate analogy with graphene, possessing two distortions relative to the pristine honeycomb lattice: the first is a buckling distortion that results in neighboring Li atoms displacing in opposite directions to each other, perpendicular to the atomic plane; the second is a bond stretching distortion that results in each lithium atom having one shorter and two longer bonds with

Table 3.1: Lattice parameters of *Pbca* structures at different pressures used in Fig. 3.4

Pressure (GPa)	Lattice constants	a (Å)	b (Å)	c (Å)
80		4.412	4.365	7.950
23		5.074	5.020	9.143
5		5.736	5.675	10.336
Wyckoff Positions		**Fractional Coordinates**		
Li1	8c	0.176	0.051	0.026
Li2	8c	0.421	0.155	0.174
Li3	8c	0.368	0.335	0.345

its nearest neighbors.

To understand the origin of the Dirac crossings and topological nature of the *Pbca* phase, we perform a computational experiment. Keeping the symmetry and Wyckoff positions fixed, we alter the volume of Li in the *Pbca* phase (see Table 3.1 for lattice parameters). We consider several lower pressures between 5 GPa and 80 GPa, the latter the pressure at which this phase is expected to be first preferred. In Fig. 3.4 we see that along the Γ–X direction, there is a band crossing close to the Fermi energy. As the pressure increases, the initially flat band shows increasing p-like character, leading to broadening of the band and a change in curvature where the band is now higher in energy at the zone center (Γ) than further towards the zone edge, until the band crossing point. An increase in p-orbital character in the near-Fermi energy band structure of Li and other alkali metals under pressure has been noted before [36, 63, 35]. This change in band character broadens the energy range over which we have linearly dispersing bands, and pushes trivial bands further from the Fermi level ensuring the nodal ring is well isolated from other bands. Although we only show the Γ–X direction in Fig. 3.4, we compute the same effect for the Dirac node along the Γ–Y direction as well. The increasing p-character in the bands in combination with the underlying nonsymmorphic crystalline symmetry gives rise to isolated Dirac crossings along these high symmetry lines at the Fermi level.

We compute that the band structures of the next three predicted phases at higher pressures – *Cmca-24*, *Cmca-56*, and $P4_2/mbc$ – also exhibit Dirac-like bands close to the Fermi energy (FIG. 3.5). While all three space groups – *Pbca, Cmca,* $P4_2/mbc$ – feature space groups with nonsymmorphic symmetries (glide planes) and inversion, the difference between *Pbca* and *Cmca* is the introduction of additional translation symmetry, and $P4_2/mbc$ includes a screw axis and reflection plane. Examining the computed Fermi surfaces of these structures at 100 GPa and 220 GPa, respectively, we note our DFT calculations predict that the *Cmca-24* phase has a Fermi surface composed of a 'pinched' nodal ring (viewed along [001] in FIG. 3.5(d)) with two flat lobes adjacent, but disconnected, at 100 GPa. Interestingly, this pinched nodal ring evolves into two perpendicular nodal rings as Li transitions

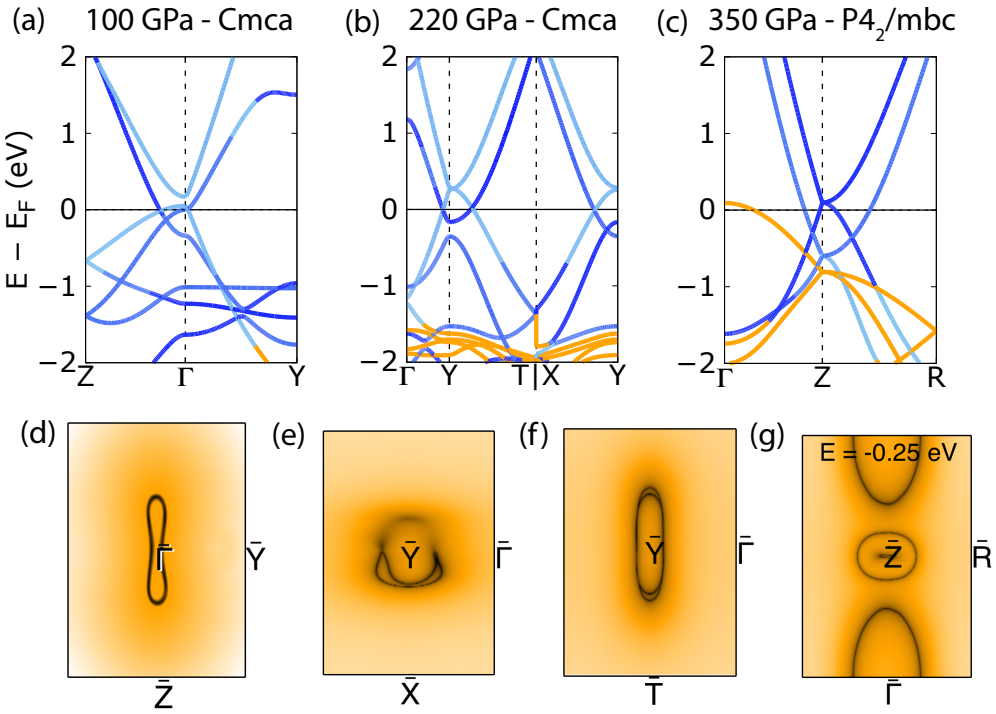

Figure 3.5: Band structures for higher pressure bulk phases for (a) *Cmca-24*; (b) *Cmca-56*; and (c) *P4$_2$/mbc*. The relative orbital contribution to the bands is shown where s-like is in orange and p-like in blue. The Dirac nodes are still present in the band structures, although as the pressure increases the s-like bands rise in energy relative to the Fermi level and the topological features are not as well-isolated from the trivial bands as in the *Pbca* case. The corresponding calculated Fermi surfaces projected on a 2D plane in the Brillouin zone are shown in (d)-(g) (The full 3D Fermi surfaces are shown in Fig. 3.7.) (d) *Cmca-24*: in the k$_z$=0 plane, the nodal loop is largely derived from the bands close to the Γ point and is much smaller in k-space than for the *Pbca* nodal ring; (e) *Cmca-56*: there are two nodal rings. The first nodal loop depicted in (e) is derived from the two crossings seen in the electronic band structure from Γ–Y and Y–X; the second nodal loop in (f) is spanned by the high symmetry directions from Γ–Y and Y–T seen at the Fermi energy in the electronic band structure.; (g) *P4$_2$/mbc*: at an energy 250 meV below E$_F$ there are two nodal loops centered at Z formed of the p-like bands as seen in the linear crossings in the corresponding band structure plot (c) at the same energy.

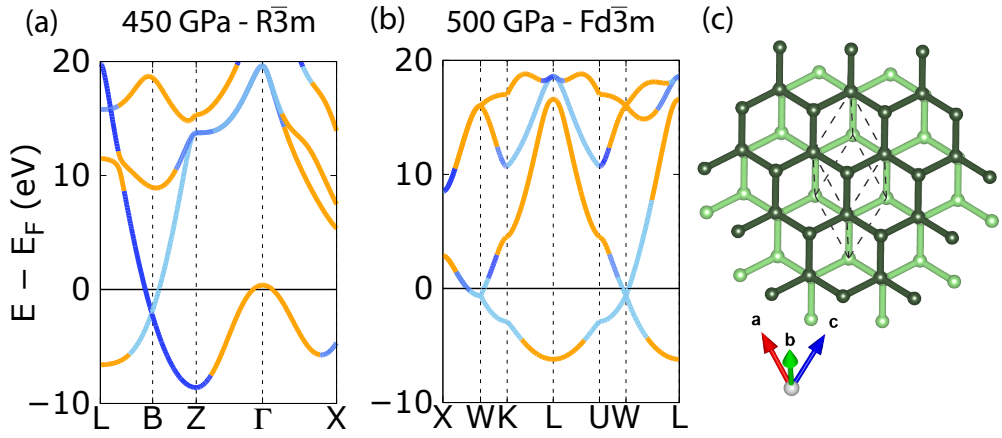

Figure 3.6: Band structures for higher pressure bulk phases for (a) $R\bar{3}m$; and (b) $Fd\bar{3}m$ where the coloring follows the same scheme as Fig. 3.3(b) and 3.5. We note the graphene-like Dirac crossing at the W point 1 eV below E_F in (b) and the bands have p-character. (c) $Fd\bar{3}m$ unit cell - coloring indicates different atomic layers which have the same buckling distortion perpendicular to the atomic plane in the hexagonal motifs similar to the *Pbca* structure; here the atoms are four-fold coordinated with their nearest neighbors and all bond lengths are 1.23 Å.

to *Cmca-56* at 220 GPa; these are not isoenergetic so appear faded in the top half of FIG. 3.5(e), and the second loop is spanned by the high symmetry directions from Γ–Y and Y–T as shown in FIG. 3.5(f). This Lifshitz transition [64, 65], or change in topology of the Fermi surface, can be seen in the constant energy cuts in Fig. 3.5 (d) – (f) as it evolves from a single loop centered at Γ to a double loop centered at the Y point. A Lifshitz transition was initially suggested to occur in metals under pressure [64]; while it has been observed experimentally in heavier elements [66, 67, 68, 69, 70, 71, 72, 73, 74, 75, 76, 77], we predict it to occur in lithium as well.

The nontrivial topological features for solid Li persist in the predicted high-pressure phases from 80–500 GPa, albeit with increasing contributions from trivial bands around the Fermi level as compared to *Pbca*. At higher pressures of 350 GPa, the near-Fermi energy Li band structure reverts to having more and more s-like character (shown in orange in Fig. 3.5 (c)), and in fact s-like character dominates at the Fermi level in the band structure of the $P4_2/mbc$ phase. Computing the electronic structure of this phase at 350 GPa, we find that the nodal rings are still present in this phase, but are now approximately 0.25 eV below the Fermi level in our DFT calculations (see Fig. 3.7). This is expected since the p-like bands are broadened more significantly under pressure reverting the order of the s- and p-like bands [78]; this has the effect of moving the Dirac nodes to lower energies relative to the Fermi level. As a growing number of states are present at the Fermi level, lithium has increasing metallic character at higher pressures compared to the *Pbca* phase at 80 GPa.

In the final two phases of the predicted pressure phase diagram, the lithium atoms are four-fold coordinated and the electronic structure exhibits highly-dispersive bands and metallic character at the Fermi level (Fig. 3.6). The $R\bar{3}m$ phase is symmorphic and its electronic structure is dominated by nearly-free electron-like bands. But as lithium adopts the $Fd\bar{3}m$ structure, the similarity to graphene becomes more pronounced in both its geometry and electronic structure: its structure consists of offset, hexagonal layers with all bond lengths approximately 1.23 (both within each hexagonal layer and between layers) and has the same 'buckling' motif, as described earlier for the *Pbca* phase. We note that at the W point on the Brillouin zone edge, where the bands are dominated by p-like character, there is a Dirac point, similar to graphene's Dirac point at its K point (which also lies on the Brillouin zone edge); albeit, here in lithium, it is 1 eV below the Fermi energy whereas in graphene it is at the Fermi level. Lithium can thus be seen to form a 3D analogue to graphene at this extremely high pressure, where again the crystallographic symmetry and dominant p-character at the Fermi level facilitates the formation of the Dirac crossing.

3.3 Structural analogy to graphene

We noted that several of the high pressure phases of lithium have hexagonal motifs, with buckling and stretching distortions. We examine the effect of these distortions on the band structure and suggest how finding materials with similar structural motifs would give rise to topological features similar to the Dirac crossing at the K point in graphene, and a degree of tunability using these structural parameters.

We show how this distorted layered honeycomb structure gives rise to a Dirac nodal line by considering a hypothetical, pristine, 2D symmetric honeycomb lattice of lithium, the Li analogue of graphene (lithene). If the lithium atoms are spaced by bond lengths of 2.70 Å, the band structure of graphene is closely reproduced, as in Fig. 3.9(a); the electron filling is different in lithium than in carbon so the Fermi level is lower in energy relative to graphene and the same Dirac crossing at the K point is found as in graphene, but at 3 eV above E_F . We then construct the bulk phase from the single layers with successive layers laterally offset by half a unit cell, shown in Fig. 3.8(c). As we decrease the lattice constants to match that of *Cmca-4*, the high pressure, undistorted, bulk phase retains the Dirac points at the Fermi level as seen in Fig. 3.9(c). Introducing the buckling and stretching distortions in the high pressure bulk phase in Fig. 3.9(d) isolates two of the Dirac crossings from the rest of the bands at the Fermi level, the feature which we observe in our calculations of the band structures for the high pressure lithium phases with these distorted, hexagonal layered motifs, namely *Pbca*, *Cmca-24* and *Cmca-56*, and $Fd\bar{3}m$.

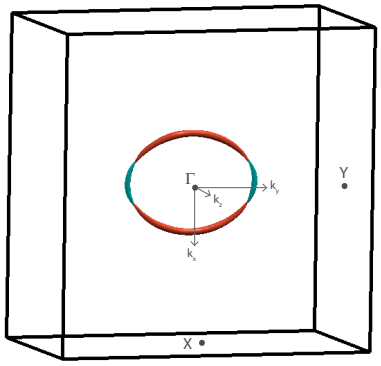

(a) Fermi surface for *Pbca* structure (k-grid density 101×101×101). The nodal ring is not isoenergetic and so an energy window of ±10 meV is included.

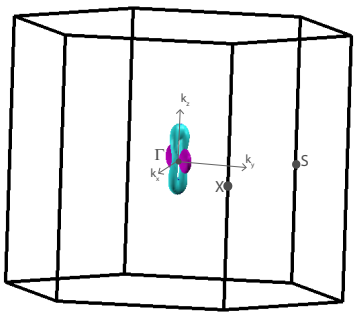

(b) Fermi surface for *Cmca-24* structure using a k-grid density of 101×101×101. The nodal loop lies parallel to the k_z axis with two flat lobes adjacent to the nodal loop.

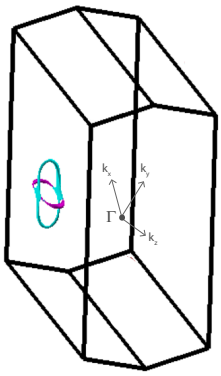

(c) Fermi surface of *Cmca-56* structure (k-grid density of 201×201×201). An energy window of ±10 meV is included; colors indicate different band contributions.

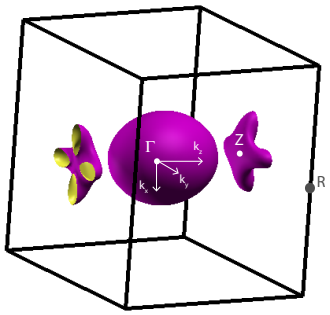

(d) Fermi surface at E = –0.25 eV of $P4_2/mbc$ structure (k-grid density of 101×101×101). Below E_F, there is a double nodal loop that spans the Brillouin zone edge, as well as a spherical contribution at the zone center.

Figure 3.7: Fermi surfaces computed with Wannier90 [21] for the high pressure phases of lithium indicating the persistence of nodal loops through a large pressure range.

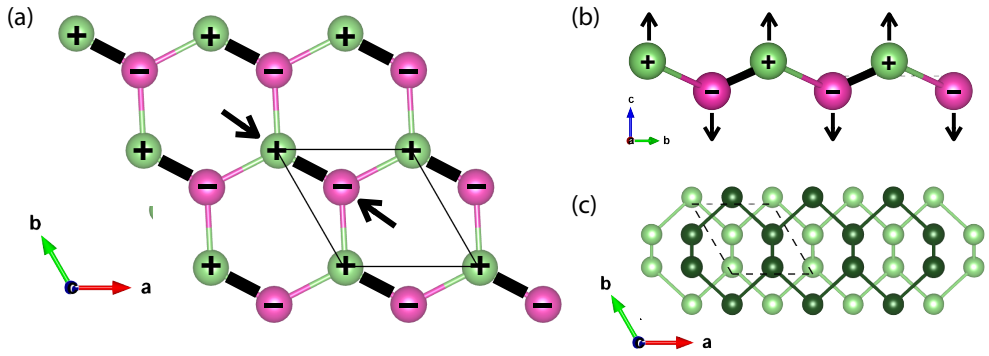

Figure 3.8: (a) Hexagonal layer of lithium, with green and pink representing the A and B sublattices. The thick black lines indicate shortened bonds showing where the bond stretching occurs as the two atoms indicated by the arrows move closer together. The buckling distortion is represented by a (+) indicating displacement out of the page and (–) displacement into the page. (b) Side view of a single layer with buckling and stretching distortions. (c) 4 atom *Cmca* structure where the different shades of green indicate two different layers in the c direction showing the half unit cell offset between subsequent layers.

3.4 Conclusions and outlook

We note that at low temperatures, topological properties are predicted appear at about 80 GPa and above, a pressure range recently probed for lithium [42]; pressures up to 400 GPa are experimentally achievable using diamond anvil cells [79], and 500 GPa appears to be within reach in the near future [80, 81, 82]. The closed loop in the Fermi surfaces, would lead to characteristic quantum oscillations in de Haas-van Alphen measurements for the *Pbca*, *Cmca*, and $P4_2/mbc$ structures (shown in Fig. 3.7). Given the small lithium mass, nuclear motion associated with zero-point and finite temperature effects would be expected to alter the structural phase diagram [83, 84, 85]; such effects may shift the zero-temperature structural phase transition pressures predicted in [3, 2] and used here. Future calculations, for example including anharmonic effects in calculations of structural energetics, as has recently been demonstrated for hydrogen [86], would be desirable. Additionally, appreciable electron-phonon interactions expected for lithium at high densities could potentially modify band dispersion, introducing satellites and kinks as has been reported in angle-resolved photoemission studies of graphene [87, 88]. Further theoretical and experimental studies will be important to explore these issues in detail and their consequences for the structural and electronic phase behavior of lithium at these high densities.

In summary, as lithium is subjected to higher and higher pressures, it favors lower coordinated phases with nonsymmorphic symmetries which enforce band stickings at high symmetry points, thus increasing the likelihood for crossings along high symmetry directions. The distorted hexagonal honeycomb structural motifs are reminiscent of graphene

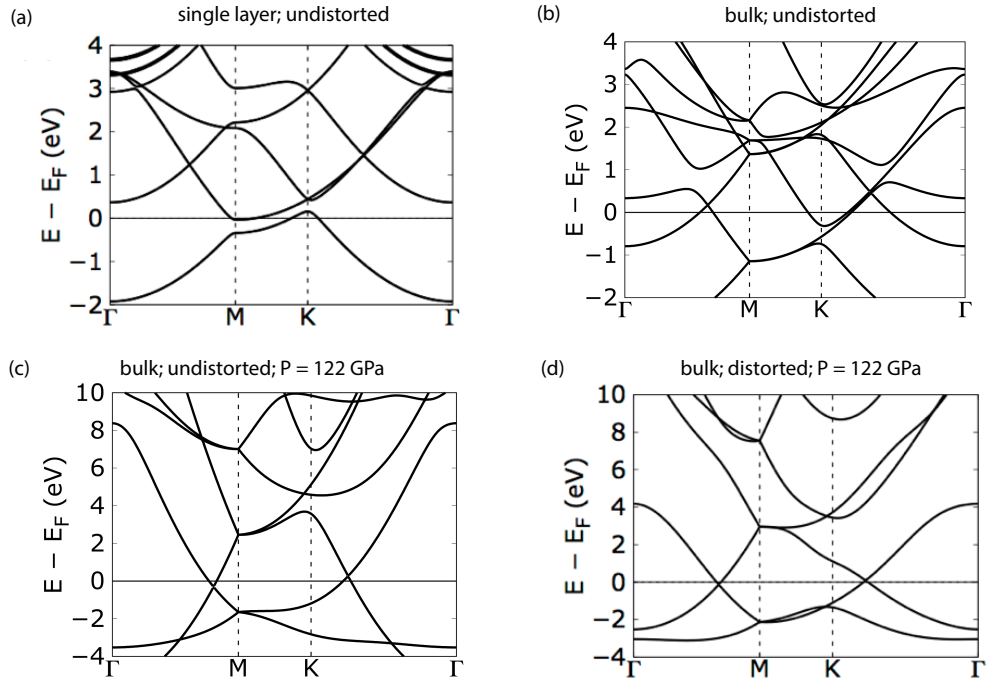

Figure 3.9: Band structures(where $E_F = 0$) for lithium in (a) undistorted single hexagonal layer at equilibrium lattice constants, (b) undistorted bulk phase at equilibrium lattice constants, (c) undistorted bulk phase with same lattice constants as *Cmca-4*), and (d) distorted bulk phase with same lattice constants as *Cmca-4*

and are consistent with the nonsymmorphic symmetries that guarantee the presence of band stickings. Furthermore, the pressures at which these structures are favored not only reorder the bands and lead to dominant p-orbital character near the Fermi level, but also shifts many of the trivial electronic bands away from the Fermi energy as they become more significantly broadened. These two effects in combination, the dominant p-character and the phase transitions to structures with nonsymmorphic symmetries, result in well-isolated Dirac nodes at the Fermi energy in high pressure lithium. When lithium assumes the *Cmca* symmetry, it undergoes a Lifshitz transition as seen by the change in Fermi surface topology between the two predicted structures. It then evolves to a more metallic $P4_2/mbc$ phase where the nodal line is slightly below the Fermi energy as the s- and p-like bands become reordered with pressure. At 500 GPa, lithium's structure consists of four-fold coordinated atoms in buckled hexagonal honeycomb layers, giving rise to a Dirac crossing 1 eV below the Fermi level as predicted by our DFT calculations. Using first-principles calculations, we show here that lithium's complex structural phase diagram also features topological electronic structure, suggesting similar features may be observed in other light elements under pressure, such as hydrogen as this author has begun to consider more. Indeed, more generally, pressure can be used to realize topological features in electronic structures in broad classes of materials.

Chapter 4

Tuning the band gap of $Cs_2AgBiBr_6$ through dilute alloying

"I have to talk like a physicist, I'm sorry"

February 16, 2018

This chapter is primarily adapted from [9].

Lead halide perovskites, with the general formula $APbX_3$ (A = monovalent cation, X = Br or I), have exhibited remarkable properties for use as solar absorbers [89, 90]; however, concerns regarding their long-term stability and the toxicity of water-soluble Pb^{2+} salts still need to be addressed [91, 92]. In order to identify lead-free materials that show similar optoelectronic properties to $APbX_3$, halide double perovskites have been introduced [5, 6, 7] as potential absorbers. In particular, $Cs_2AgBiBr_6$ displayed a long carrier lifetime, which is beneficial for charge extraction in a solar cell, and higher stability to heat and moisture compared to $(CH_3NH_3)PbI_3$ [5]. However, the large and indirect band gap of 1.95 eV in $Cs_2AgBiBr_6$ affords weak sunlight absorption (see Fig. 4.1). Recent work showed that the band gap of $Cs_2AgBiBr_6$ could be reconstructed through dilute Tl alloying [8]. Here, incorporation of Tl^+ resulted in a modest reduction in band gap, although the transition was calculated to be direct. Incorporation of less than 1 atom% of Tl^{3+}, on the other hand, resulted in approximately a 0.5 eV band gap reduction while retaining the indirect band gap of the host perovskite. Indeed Tl^{3+} alloying makes the optoelectronic properties of $Cs_2AgBiBr_6$ competitive with those of the $APbX_3$ absorbers. Although the use of toxic Tl, even at small concentrations, is undesirable for large-scale applications, this study provided the orbital basis for reconstructing the band gap of $Cs_2AgBiBr_6$ through dilute alloying.

Building on the understanding of the effects of Tl alloying, we sought a less toxic element that could provide similar band gap reconstruction in $Cs_2AgBiBr_6$. Our prior computational studies revealed that band gap reconstruction can be affected by both the filled 6s shell of Tl^+ and the empty 6s shell of Tl^{3+} [8]. With this knowledge guiding our search, we sought to

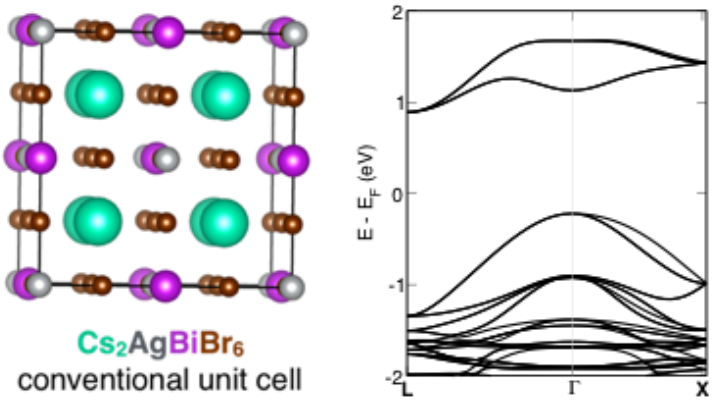

Figure 4.1: The conventional unit cell of $Cs_2AgBiBr_6$ is depicted on the left while the band structure calculated with DFT–PBE is on the right; as is expected, the band gap is underestimated at 1.11 eV and is indirect. We note that in the band structure of the primitive unit cell, the valence band maximum is unfolded from Γ to X.

incorporate Sn into $Cs_2AgBiBr_6$ because of the similar electronic configurations of Tl^+ and Tl^{3+} with Sn^{2+} and Sn^{4+}, respectively. Additionally, both Sn^{2+} and Sn^{4+} are known to form halide perovskites [93, 94]. Because both Sn^{2+} and Sn^{4+} are heterovalent with respect to Ag^+ and Bi^{3+}, this study presented the opportunity of understanding both possible substitution sites and charge-compensating defects in $Cs_2AgBiBr_6$, and how they depended on sample morphology and synthetic conditions. Heterovalent alloying has been studied in many other materials and is known to have a variety of effects on the host material, including modulating carrier concentrations [95], altering the kinetics of phase transformation [96, 97], lowering the ferroelectric transition temperature [97], inducing disorder and vacancies [98, 99], and affecting ionic conductivity [96, 98].

Although there have been numerous attempts at incorporating small amounts of monovalent and trivalent metals into the lead perovskites [100, 101, 102, 103, 104, 105, 106, 107, 108, 109, 110, 111], detailed experimental characterization of the resulting materials that provide a thorough understanding of the structural and electronic changes in the alloys are still needed. A recent study with a computational focus explored Pb^{2+} alloying of $Cs_2AgBiBr_6$, which resulted in a ∼0.1 eV decrease of the absorption onset [112]. In order to probe the complexities of heterovalent alloying in $Cs_2AgBiBr_6$, a combination of single-crystal and powder X-ray diffraction, optical absorption and photothermal deflection spectroscopy, elemental analysis and redox titration, nuclear magnetic resonance spectroscopy, X-ray absorption spectroscopy, scanning electron and atomic force microscopy, and band structure calculations are used to elucidate the structural and electronic effects of Sn alloying in $Cs_2AgBiBr_6$. We show here that Sn alloying substantially reduces the band gap of $Cs_2AgBiBr_6$, affording a low-band gap halide perovskite free of highly toxic elements.

4.1 Experimental measurements

The experimentalists were able to synthesize crystals and thin films of Sn–alloyed $Cs_2AgBiBr_6$ where the Ag and Bi sites were replaced with Sn (the thin films accommodated a higher Sn content from 1–4 atom %) [9]. Furthermore they found that the samples were stable for prolonged exposure to heat and moisture. Depending on the concentration of Sn in the crystals of Sn–alloyed $Cs_2AgBiBr_6$ the physical color of the crystal varies from red to black. The band gaps were determined by analyzing UV-vis diffuse reflectrance spectra and support either a direct band gap of 1.71 eV or an indirect band gap of 1.48 eV for a concentration of 1 atom% Sn. The absorption onset energy initially drops quickly with increasing Sn content at low alloying concentrations, then shows a slower reduction at high Sn concentrations, reaching a maximum redshift of ca. 0.5 eV [9]. Photothermal deflection spectroscopy (PDS) was used to ensure that the band gap shifts were not induced by sub-band gap trap states caused by Sn impurities, and indeed is arising due to a band gap reduction.

Sn can adopt a 2+ or 4+ oxidation state and given the Ag and Bi nominally have a 1+ and 3+ oxidation state, respectively, either Sn oxidation state can be introduced into $Cs_2AgBiBr_6$ with charge compensating vacancies. To determine the oxidation state of Sn in these alloyed crystals, X-ray absorption near-edge structure (XANES) spectra at the Sn L3- and K-edges in Sn–alloyed $Cs_2AgBiBr_6$ (1 atom% Sn) were compared to those of $CsSn^{II}Br_3$ and $Cs_2Sn^{IV}Br_6$ perovskite standards. The results indicated that there is a mixture of 2+ and 4+ oxidation states in the crystal samples. Further analysis using redox titration, magic-angle spinning solid-state 119Sn NMR all indicated a similar possible range of ratios of Sn^{2+} to Sn^{4+}, in agreement with the XANES results range. Both $CsSnBr_3$ and Cs_2SnBr_6 are stable; by comparing to those NMR spectra can yield insight into the oxidation state of Sn in the $Cs_2AgBiBr_6$ samples. To best approximation, a ratio of 2:1 Sn^{2+}:Sn^{4+} was assigned, although there is a degree of variability between samples and the uniformity of distribution of dopants/vacancies is not well characterized.

Given that heterovalent substitution of Sn in $Cs_2AgBiBr_6$ was expected to produce charge-compensating vacancies, inductively coupled plasma mass spectroscopy and optical emission spectroscopy (ICP-MS/ICP-OES) were used to quantify the elemental composition of Sn–alloyed $Cs_2AgBiBr_6$. The observed increase in the lattice parameters is consistent with Sn being introduced into $Cs_2AgBiBr_6$; furthermore, the analysis showed that while there is a slight decrease in the Bi concentration, there is a more substantial decrease in Ag content, more than the predicted value for a 1:1 substitution of Sn for Ag, suggesting that Ag vacancies are being formed as a charge–compensating mechanism with Sn alloying. Single crystal x-ray diffraction (SCXRD) also corroborates that there is a larger fraction of Ag than Bi missing, further corroborating the evidence that the majority of charge compensating vacancies are on the Ag sites.

The XANES, redox titration, NMR, ICP, and SC–XRD results, taken together, indicate that Sn^{2+} substitutes at the Ag^+ site while Sn^{4+} substitutes at the Bi^{3+} site with an approximate ratio of 2:1 Sn^{2+} to Sn^{4+}, collectively generating Ag^+ vacancies as the primary charge-compensating defect. Similar charge-compensating metal cation vacancies have been

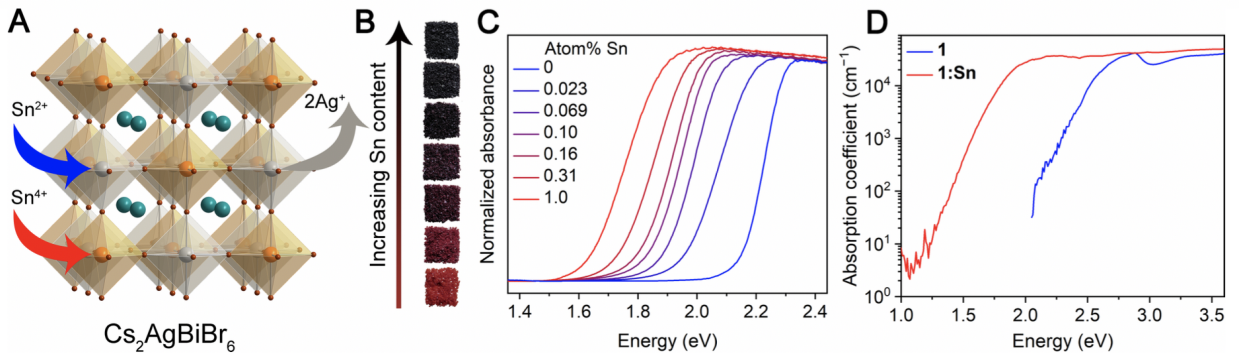

Figure 4.2: A) The crystal structure of $Cs_2AgBiBr_6$ and an illustration of the substitution mechanism of Sn in crystals to yield Sn–alloyed $Cs_2AgBiBr_6$. Orange, gray, turquoise, and brown spheres represent Bi, Ag, Cs, and Br atoms, respectively. B) Photographs of crystals of 1 and Sn–alloyed $Cs_2AgBiBr_6$. C) UV-vis absorbance spectra of crystallites of $Cs_2AgBiBr_6$ and Sn–alloyed $Cs_2AgBiBr_6$ converted from diffuse reflectance spectra using the Kubelka-Munk transformation. Atom% Sn was obtained from inductively coupled plasma analysis. D) Photothermal deflection spectroscopy (PDS) scans collected on thin films of $Cs_2AgBiBr_6$ and Sn–alloyed $Cs_2AgBiBr_6$ (4 atom% Sn; estimated from X-ray photoelectron spectroscopy). In the high-energy region (> 3.0 eV), PDS and UV-vis absorbance data were combined after normalization. Adapted from [9].

observed in oxide perovskites upon heterovalent substitution [113]. We assume substitution of Sn^{2+} at the Ag^+ site and Sn^{4+} at the Bi^{3+} site due to the large mismatch in valence between Sn^{4+} and Ag^+. Additionally, substitution of Sn^{2+} at the Bi^{3+} site would require a positively charged compensating defect, such as a Br- vacancy, which is not supported by the ICP nor the SC–XRD results. The modest decrease of Bi content with Sn alloying suggests that there is no significant density of Bi vacancies in Sn–alloyed $Cs_2AgBiBr_6$. We therefore propose the formula $Cs_2(Ag_{1(2a+b)}Sn_a^{II})(Bi_{1b}Sn_b^{IV})Br_6$ for Sn–alloyed $Cs_2AgBiBr_6$ crystals, where $0.0023(1) < a + b < 0.10(2)$. Similar to the host lattice $Cs_2AgBiBr_6$, which exhibits only very weak photoluminescence, the alloyed material Sn–alloyed $Cs_2AgBiBr_6$ does not photoluminesce, consistent with its computed indirect band gap. It is also possible that the lattice vacancies required for heterovalent alloying may act as nonradiative carrier recombination sites. Therefore, the carrier dynamics of Sn–alloyed $Cs_2AgBiBr_6$ should be studied to assess the feasibility of charge extraction from lattices containing metal cation vacancies.

4.2 Supercell geometries

The experimental synthesis yielded structures with less than 12% concentration of Sn atoms. In order to model these in our DFT calculations, we need to construct supercells of the

$Cs_2AgBiBr_6$ unit cell, and replace the Ag and/or Bi sites with an appropriate number of Sn and vacancies. Given that our calculations are periodic in all directions, one must create symmetrically similar unit cells (i.e. create 2×1×1 or 2×2×1 or 2×2×2 supercells of the conventional unit cell geometry of $Cs_2AgBiBr_6$ which contains 40 atoms) to ensure the symmetry of the supercell matches that of the original conventional unit cell. Since DFT scales as $\sim N^3$, with N being the number of atoms, increasing the number of atoms substantially creates calculations which can become prohibitively expensive. As such, we make a compromise between using a higher Sn concentration but determining the qualitative trends and effects on the electronic structure as a result of introducing Sn dopants. We tested the different configurations involving Ag and Bi substitutions that would correspond to Sn^{2+} and to Sn^{4+}. The $CsSnBr_3$ and Cs_2SnBr_6 compounds both have direct band gaps, with DFT–PBE level gaps of less than 1 eV. As such, one would expect that increasing the concentration of Sn will eventually lead $Cs_2AgBiBr_6$ to shift from an indirect to direct gap.

4.3 Electronic structure

Our DFT calculations are performed using the generalized gradient approximation of Perdew, Burke, and Ernzerhof (PBE) and the projector augmented wave formalism (PAW) as implemented in VASP [114, 115]. The PAW potentials used here include 9 valence electrons for Cs ($5s^25p^66s^1$), 11 for Ag ($4d^{10}5s^1$), 5 for Bi ($6s^26p^3$), 4 for Sn ($5s^25p^2$), and 7 for Br ($4s^24p^5$). For 80 atom supercells of $Cs_2AgBiBr_6$ we perform Brillouin zone integrations on 4×4×4 Γ-centered k-point meshes, scaled proportionally for the larger unit cells, as well as a plane-wave cutoff of 500 eV, with spin-orbit coupling taken into account self-consistently. The structural relaxations are performed without spin-orbit coupling (SOC), allowing the internal coordinates and volume to relax until Hellmann-Feynman forces are less than 0.01 eV/Å.

Given the nominal charge of Sn is even and those of Ag and Bi are odd, substitution of Sn for either Ag or Bi without including charge-compensating vacancies is expected to lead to a metallic system due to an excess of electrons. Since the measured sample is not metallic, and the experimental data suggest that the Ag and Bi sites have reduced occupation in Sn–alloyed $Cs_2AgBiBr_6$ relative to $Cs_2AgBiBr_6$, we introduced vacancies in addition to the Sn substitutions. We tested four different combinations of Sn substitutions and vacancies on Ag and/or Bi sites that would nominally result in a Sn^{2+} or Sn^{4+} oxidation state, assuming oxidation states of Ag^+ and Bi^{3+}. For each of these substitution cases, the total energies for each substitution of the Sn and vacancies on the different Ag and Bi sites in the supercells were compared. In all cases, the substitutions on adjacent sites are slightly energetically preferred (<100 meV), therefore, these configurations are used to report the calculated band gaps. The calculated band gap (calculated with DFT–PBE–SOC) can change by up to 0.14 eV based on the supercell configuration. However, comparison of the lowest- and highest-energy structures reveals that the general features of the band structures are similar, especially the orbital character of the bands at the band edges. We further

compare the relative formation energies based on these total energies of the relaxed structures relative to the solid elemental compounds as $E_{formation} = (E_{doped} - E_{undoped}) + \sum_\alpha n_\alpha \mu_\alpha$ with the results shown in Table B.5.

We calculated the band structures for Sn–alloyed $Cs_2AgBiBr_6$ to understand the electronic consequences of Sn^{2+} and Sn^{4+} alloying in 1. Our calculations were performed using DFT within the generalized gradient approximation of Perdew, Burke, and Ernzerhof (PBE) as implemented in the VASP code37, 38. Spin-orbit coupling (SOC) effects were treated self-consistently. The calculated band gap of an 80-atom supercell of 1 (we note that in the band structure of the primitive unit cell the valence band maximum is unfolded from Γ to X) using this method is 1.11 eV, underestimating the experimental value of 1.95 eV, as is expected for DFT–PBE–SOC and consistent with past calculations from similar computations for $(CH_3NH_3)PbI_3$.39 Accurate prediction of band gap energies requires a more rigorous treatment of exchange and correlation effects, including electron-hole interactions, that is currently prohibitive for the large unit cells considered here; however, our DFT–PBE–SOC calculations are expected to capture trends, sufficient for the present study (see Supporting Information for details).

For our DFT calculations of the band gap of Sn–alloyed $Cs_2AgBiBr_6$, we constructed supercells in which one or more of the B-site cations were substituted with Sn, where B-site refers to the octahedrally coordinated cation in the perovskite (Ag and Bi in 1). The insertion of heterovalent Sn – which may be considered to assume nominal charges of Sn^{2+} or Sn^{4+} – into the structure of $Cs_2AgBiBr_6$ necessitates a charge-compensating mechanism to maintain charge neutrality, such as the formation of cation vacancies. Because of the numerous permutations of possible substitution scenarios and the computational expense of using such large supercells, we used our experimental results to guide our choice of calculations: we considered four separate cases that could arise in nominal Sn^{2+} and Sn^{4+} substitutions, assuming the Sn atoms and vacancies substitute only at the Ag and Bi sites, consistent with our experimental evidence.

Case 1: Two Ag atoms were removed and replaced with one Sn and one vacancy, respectively, to model nominal Sn^{2+} substitution at the Ag site with Ag vacancies as the charge-compensating defect. The supercell consisted of 80 atoms, corresponding to 1.25 atom% Sn substitution. In this supercell, there were 8 different Ag sites for substitution, thus 7 different relative arrangements of the Sn and vacancy on these sites were considered. For all arrangements, the lattice parameters and internal coordinates were relaxed (without spin-orbit coupling) until the forces were converged to 10 meV/Å. The arrangement with Sn and the vacancy occupying adjacent B-sites was computed to have the lowest energy (see B.2 for details.) The calculated band structure of this arrangement, including spin-orbit coupling, revealed a direct band gap with a modest reduction of <0.1 eV from the DFT–PBE–SOC band gap of $Cs_2AgBiBr_6$ (Fig. 4.3).

Case 2: One Bi atom was replaced with one Sn atom and one Ag vacancy was introduced to model nominal Sn^{4+} substitution at the Bi site with Ag vacancies as the charge–compensating defect. The supercell consisted of 80 atoms for a 1.25 atom% concentration of Sn. After considering several arrangements of the Sn and vacancy (see Supporting Informa-

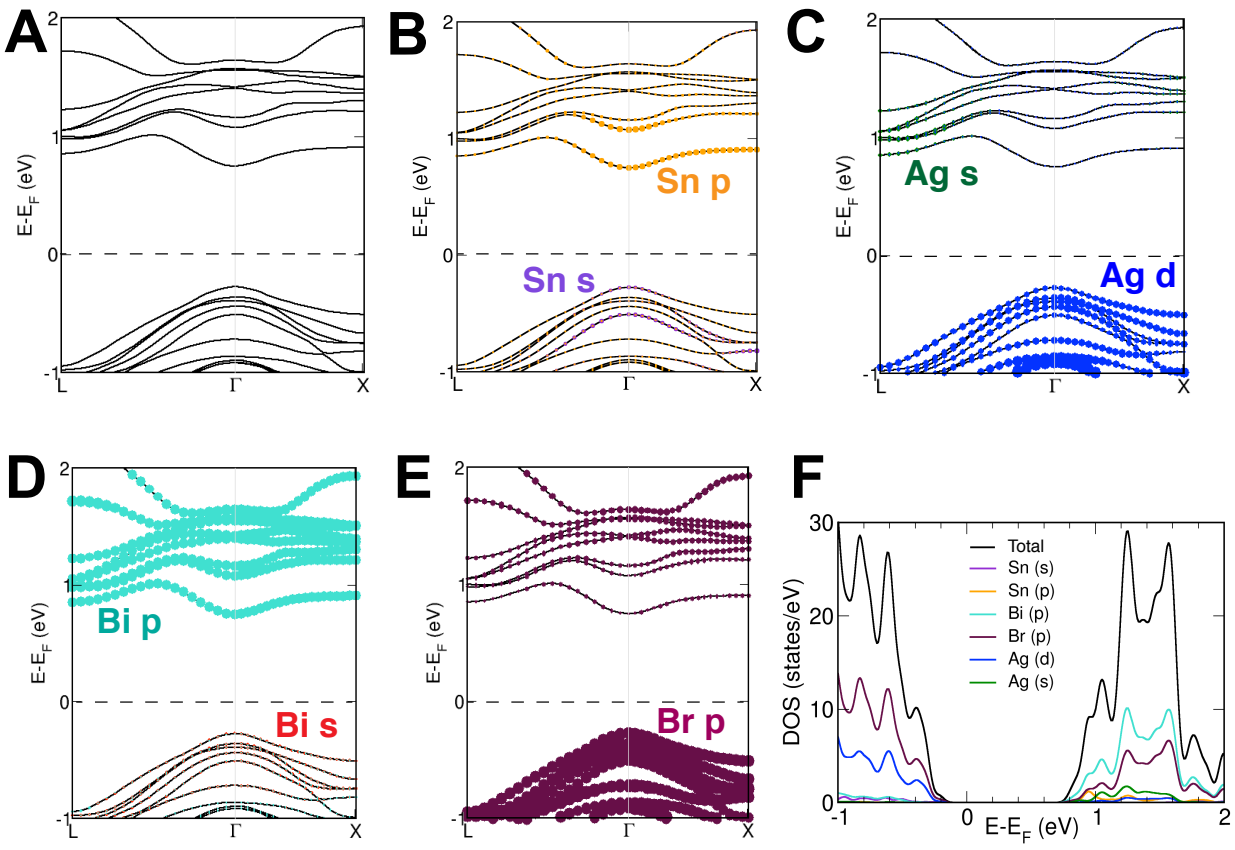

Figure 4.3: DFT–PBE–SOC band structure of Sn–alloyed $Cs_2AgBiBr_6$ (1.25 atom% Sn) with two Ag atoms removed and replaced with one Sn and one vacancy, nominally resulting in a Sn^{2+} oxidation state. The band gap at the DFT–PBE–SOC level is computed to be 1.02 eV. Projections of the orbital character of the bands are shown in color in A-E), with the projected density of states in F). Here, E_F indicates the Fermi energy.

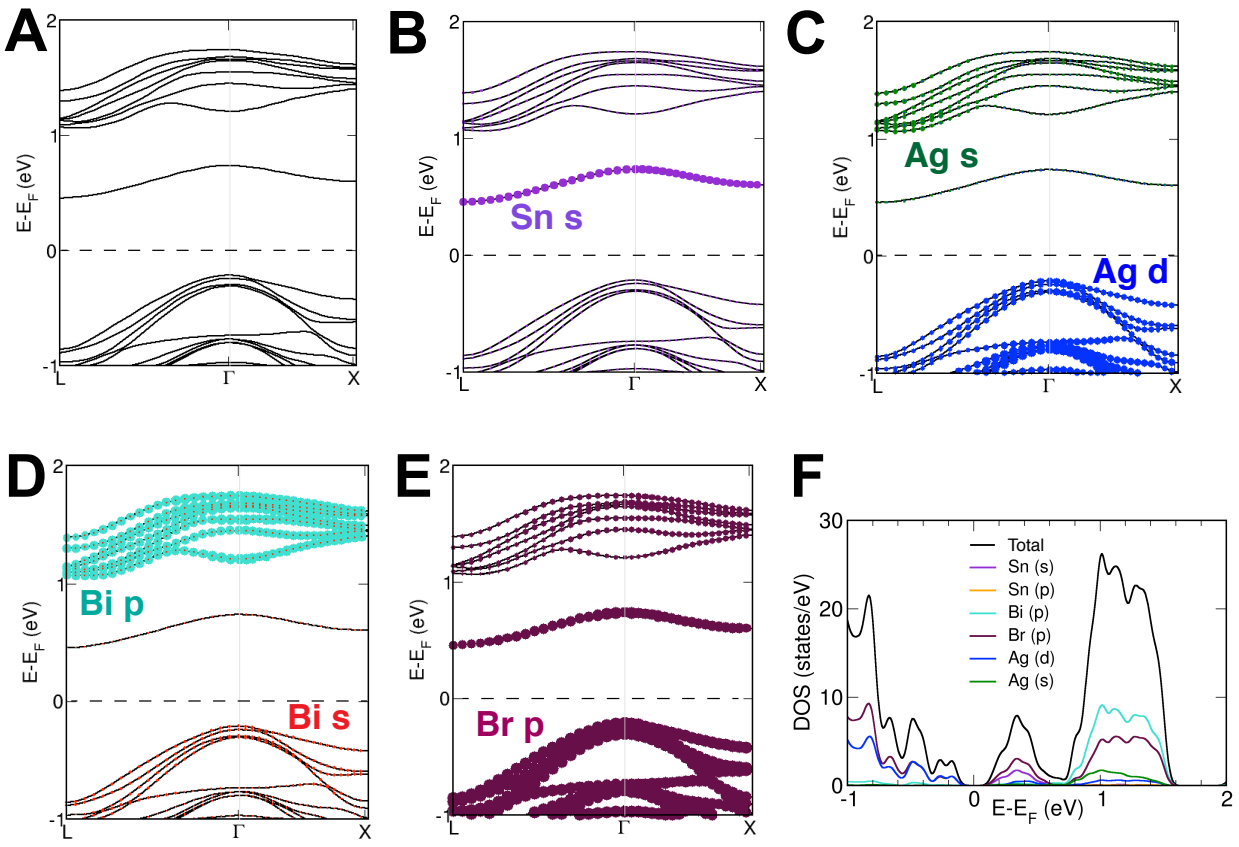

Figure 4.4: DFT–PBE–SOC band structure of Sn–alloyed $Cs_2AgBiBr_6$ (1.25 atom% Sn) with one Ag atom replaced by a vacancy and one Bi atom replaced by Sn, nominally resulting in a Sn^{4+} oxidation state. The band gap at the DFT–PBE–SOC level is computed to be 0.67 eV. Projections of the orbital character of the bands are shown in color in A-E), with the projected density of states in F). Here, E_F indicates the Fermi energy.

tion for details), the structure placing Sn and the vacancy at adjacent B–sites was computed to be the lowest-energy structure, similar to Case 1. In contrast to Case 1, Case 2 resulted in an indirect but substantially reduced DFT–PBE–SOC band gap (by 0.44 eV), in qualitative agreement with the experimentally determined band gap reduction of 0.5 eV in crystals of Sn–alloyed $Cs_2AgBiBr_6$ (1 atom% Sn; Fig. 4.4).

Case 3: Four Bi atoms were replaced with three Sn atoms and one vacancy to model nominal Sn^{4+} substitution at the Bi site with Bi vacancies as the charge-compensating defect. The supercell consisted of 160 atoms for a 1.875 atom% concentration of Sn. After comparing the DFT–PBE energies of 8 relaxed structures with substitutions on different Bi sites in the supercell, the lowest energy configuration was computed to be one in which the Sn atoms

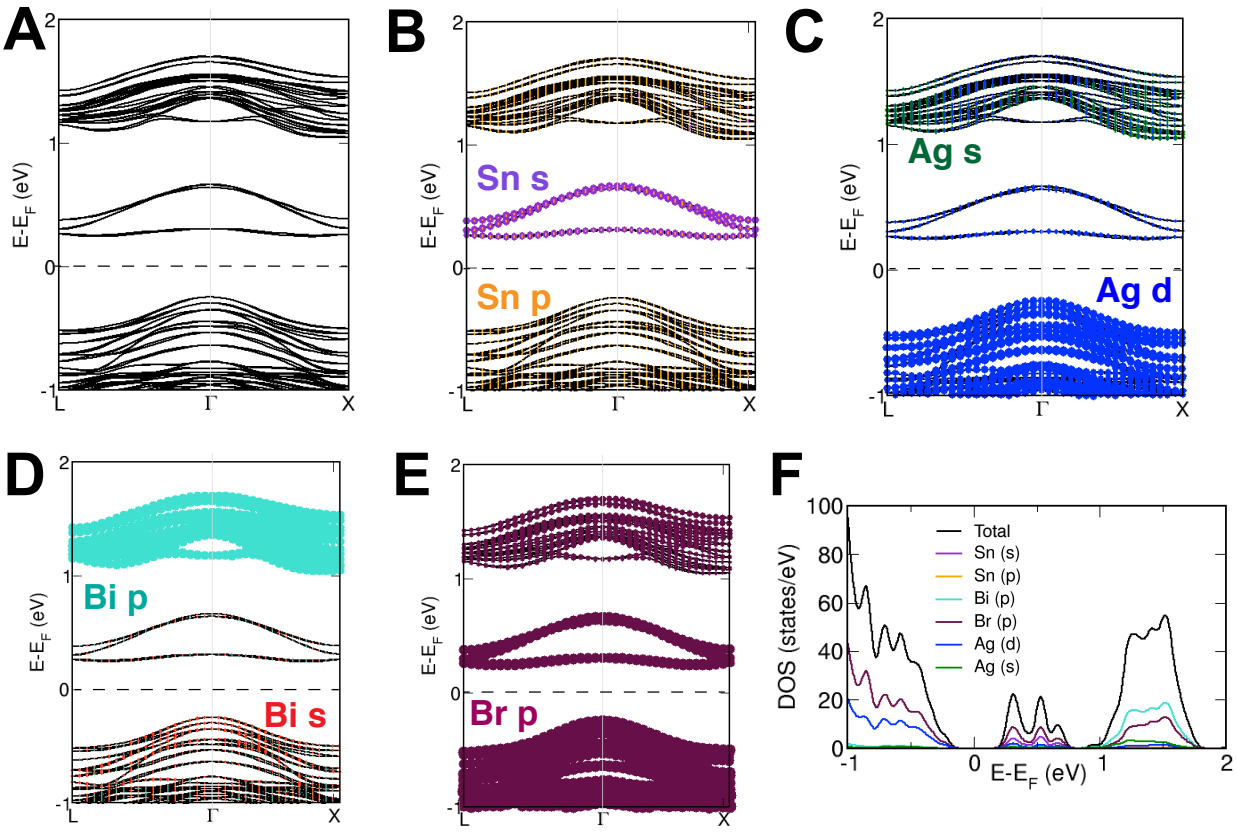

Figure 4.5: DFT–PBE–SOC band structure of Sn–alloyed $Cs_2AgBiBr_6$ (1.875 atom% Sn) with four Bi atoms replaced by one vacancy and three Sn atoms, nominally resulting in a Sn^{4+} oxidation state. The band gap at the DFT–PBE–SOC level is computed to be 0.49 eV. Projections of the orbital character of the bands are shown in color in A-E). Here E_F indicates the Fermi energy

and vacancy occupy adjacent sites, similar to the previous cases. The calculated DFT–PBE–SOC band structure in this scenario had a slightly indirect band gap, while the conduction band had a very narrow bandwidth compared to the other cases. The band gap was reduced by 0.61 eV compared to 1, in qualitative agreement with the experimentally determined reduction (Fig. 4.5). This could be due to the high concentration of Sn considered in the computation, which is in excess of the concentration experimentally achieved in crystals of Sn–alloyed $Cs_2AgBiBr_6$. Nevertheless, we expect the band structure trends from these higher-concentration Sn supercells to be relevant to our measurements.

Case 4: One Ag and one Bi atom were each replaced with Sn atoms to model nominal Sn^{2+} substitution at equivalent concentrations at each B-site. The supercell consisted of 80

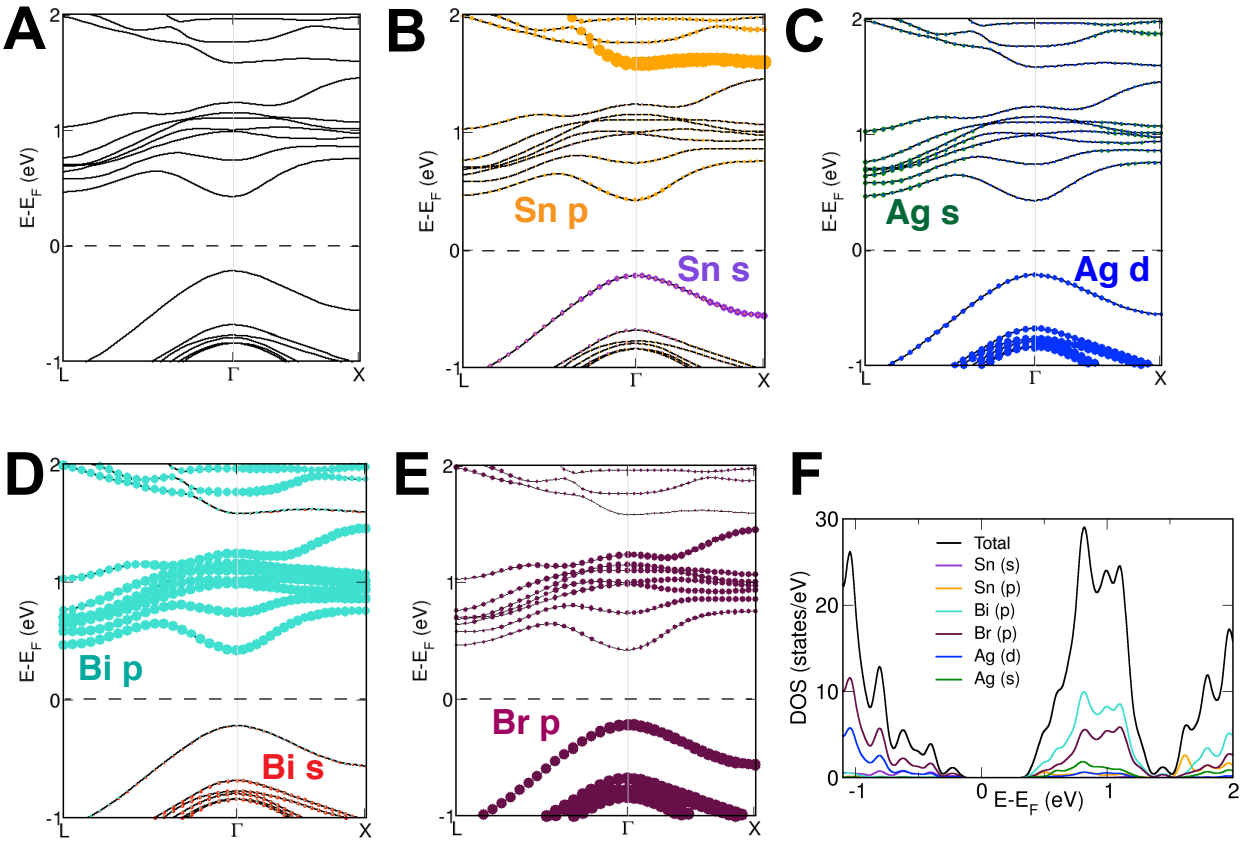

Figure 4.6: DFT–PBE–SOC band structure of Sn–alloyed $Cs_2AgBiBr_6$ (2.5 atom% Sn) with one Ag and one Bi atom each replaced by an Sn atom, nominally resulting in a Sn^{2+} oxidation state. The band gap at the DFT–PBE–SOC level is computed to be 0.64 eV. Projections of the orbital character of the bands are shown in color in A-E), with the projected density of states in F). Here E_F indicates the Fermi energy.

atoms, giving an overall concentration of 2.5 atom% Sn. The lowest-energy arrangement contained Sn atoms on adjacent Ag and Bi sites (see Supporting Information for details). A largely computational study of Pb^{2+} alloying in 1 proposes a similar mechanism.28 The DFT–PBE–SOC band gap in this case was calculated to be direct, and reduced by 0.47 eV relative to the band gap of $Cs_2AgBiBr_6$ (Fig. 4.6).

In Case 1, our DFT calculations indicate the direct band gap results from the introduction of Sn $5p^0$ character and Sn $5s^2$ character at Γ. In contrast, in Case 2, the Sn substitution at the Bi site results in the introduction of a band below the CBM with Sn $5s^0$ character at L, resulting in a more reduced but slightly indirect band gap (Fig. 4.4 and Table B.1). To confirm that the direct band gap afforded by Sn^{2+} alloying contributes to optical absorption, we

calculated the magnitudes of the transition dipole matrix elements in the independent particle approximation for $Cs_2AgBiBr_6$, Sn^{2+}-alloyed $Cs_2AgBiBr_6$ (Cases 1 and 4), and the direct band gap semiconductor $CsPbBr_3$ for comparison. Although the magnitudes of the transition dipole matrix elements for Sn–alloyed $Cs_2AgBiBr_6$ are smaller than those of $CsPbBr_3$, they are significantly greater than the negligible magnitude for $Cs_2AgBiBr_6$, supporting the presence of an optically active direct band gap in Sn^{2+}-alloyed $Cs_2AgBiBr_6$ (Fig. 4.8). We additionally calculated the imaginary part of the dielectric function as a function of energy in the independent particle approximation for $Cs_2AgBiBr_6$ and Sn^{2+}-alloyed $Cs_2AgBiBr_6$ (Cases 1 and 4) to approximate their absorption spectra. These calculations show a lowering in the onset energy of the dielectric functions, offering further support for the band gap reconstruction in Sn^{2+}- alloyed $Cs_2AgBiBr_6$ (Fig. 4.9).

Because the $5s^0$ orbital from nominal Sn^{4+} substitutions is expected to be lower in energy than the $5p^0$ orbital from Sn^{2+} substitutions, a sample comprising both Sn^{2+} and Sn^{4+} in comparable amounts, as is the case for Sn–alloyed $Cs_2AgBiBr_6$ crystals, would therefore be expected to have a substantially reduced indirect band gap. In order to assess the effect of nominal mixed valence substitution, we constructed a 320-atom supercell of $Cs_2AgBiBr_6$ and did the following substitution in order to mimic a 2:1 Sn^{2+}:Sn^{4+} alloying concentration (see Table B.4). Given the large number of atoms, we chose a representative substitution pattern based on the other calculations suggesting that the Sn and vacancies energetically prefer to substitute on nearby sites rather than try all possible cases and compare the energies. The internal coordinates were allowed to relax (again without including SOC) and then the band structure was computed including SOC (Fig. 4.7). We find indeed that the bands hybridized with Sn s orbitals are lower in energy than those with Sn p contributions as expected. At very low alloying concentrations, Sn impurities should act as point-defects with relatively flat in-gap bands. With increasing concentration, the Sn hybridizes with the $Cs_2AgBiBr_6$ bands and forms more dispersive bands which alter the electronic structure in these alloyed cases, as corroborated through PDS measurements of Sn–alloyed $Cs_2AgBiBr_6$ films and as we calculate here.

4.4 Transition dipole matrix elements and band folding

When using supercells, the Brillouin zone is necessarily folded from the Brillouin zone corresponding to the primitive unit cell. Therefore, there are instances where band edges appear at different high symmetry points for the band structure of the supercell as compared to the true primitive unit cell, such as is the case for $Cs_2AgBiBr_6$ that the valence band maximum appears at Γ in the band structure for the supercell, but in the primitive unit cell is unfolded to X. This is particularly important to take into account when studying these alloyed materials since a direct or indirect gap is of interest for their potential optoelectronic applications.

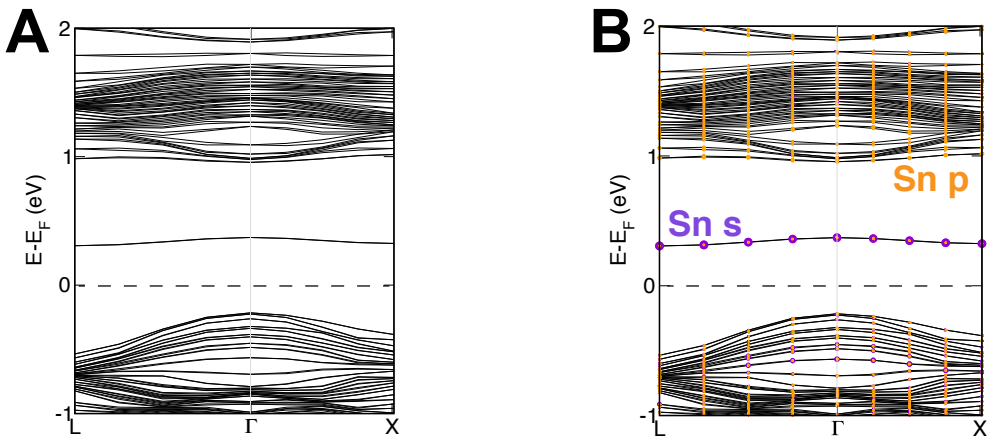

Figure 4.7: DFT–PBE–SOC band structure of Sn–alloyed $Cs_2AgBiBr_6$ with two Ag and one Bi atom each replaced by Sn atoms, and 3 Ag atoms replaced by vacancies, nominally resulting in a 2:1 ratio of Sn^{2+}: Sn^{4+} in a 320 atom unit cell of $Cs_2AgBiBr_6$. The band gap at the DFT–PBE–SOC level is computed to be 0.52 eV between the VBM at Γ and the CBM at L. Projections of the Sn s and p character of the bands are shown in color in B. Here E_F indicates the Fermi energy. Note that due to the computational expense, a coarser k-grid density was used with 5 k-points computed along each of the high symmetry directions.

However, the process of band unfolding, while exact for an undoped unit cell, or in the limit of a substitutional defect representing a weak perturbation, is not necessarily rigorous when considering higher concentrations of alloying. There is a question as to when the 'supercell' of the alloyed structure is truly the smallest unit cell, and to reduce it back to the primitive unit cell would be an approximation, since the material possesses lower symmetry than the primitive unit cell of the undoped structure. Certainly in the case of point defects this would seem to be valid, but with alloying concentrations above 10%, it is less obvious whether it is truly a weak perturbation. When using the software BandUP to unfold the band structure of Case 1, for instance, we see faint contributions both at Γ and at X. One could either interpret this as suggesting that there are transitions allowed at both momentum points, or one could argue that unfolding is inappropriate and that the supercell does represent the smallest unit cell of this doped compound. In principle, one could study this more carefully, for instance, by choosing a material where say at Γ in the undoped material the gap is dipole forbidden but in the fully alloyed structure it is dipole allowed. Then one could systematically reduce the doping concentration and unfold the band structures studying the changes, however we leave this to future work.

In the case of the Sn–alloyed $Cs_2AgBiBr_6$ we want to know if what appears to be a direct gap at Γ in the Sn alloyed $Cs_2AgBiBr_6$ is truly a dipole allowed transition. If the band structure should be unfolded, then the gap would not be dipole allowed. As such, we calculate

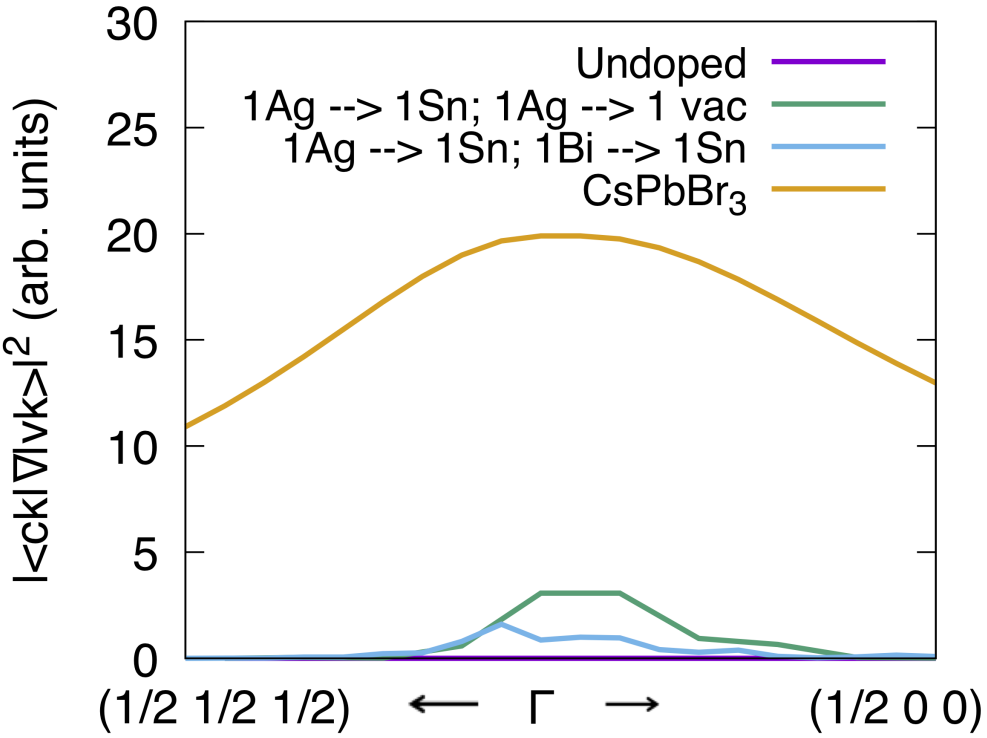

Figure 4.8: The magnitude of the transition dipole matrix elements of direct transitions between the highest lying valence and lowest lying conduction band in the vicinity of Γ for $Cs_2AgBiBr_6$, Sn–alloyed $Cs_2AgBiBr_6$ (alloying Cases 1 and 4, which are predicted to give direct gaps), and for $CsPbBr_3$, a direct band gap perovskite. Equivalent k points are denoted; (1/2, 1/2, 1/2) corresponds to L and R in the double perovskites and in $CsPbBr_3$, respectively. The range of k-points plotted is from (0, 0, 0) to (0.1, 0.1, 0.1), corresponding to the direction from Γ towards L or R, and from (0, 0, 0) to (0.1, 0.0, 0.1), corresponding to the direction from Γ towards X.

the dipole transition matrix elements and compare them along the high symmetry directions for the different alloyed compounds. Due to the computational expense, we do this in the independent particle approximation, ignoring any electron–hole interactions and ignoring local field effects. We suspect if one were to calculate these matrix elements and optical spectra with the Bethe-Salpeter equation [116] (including electron-hole interactions), there would be more quantitative agreement with experiment, but due to the large computational cost, we use the independent particle approximation which should suffice for qualitative trends.

We provide a detailed analysis of how the optoelectronic properties of the halide double perovskite $Cs_2AgBiBr_6$ can be tuned through Sn alloying. Our results are consistent with the following primary substitution pathway for crystals: Sn^{2+} substitutes at the Ag^+ site

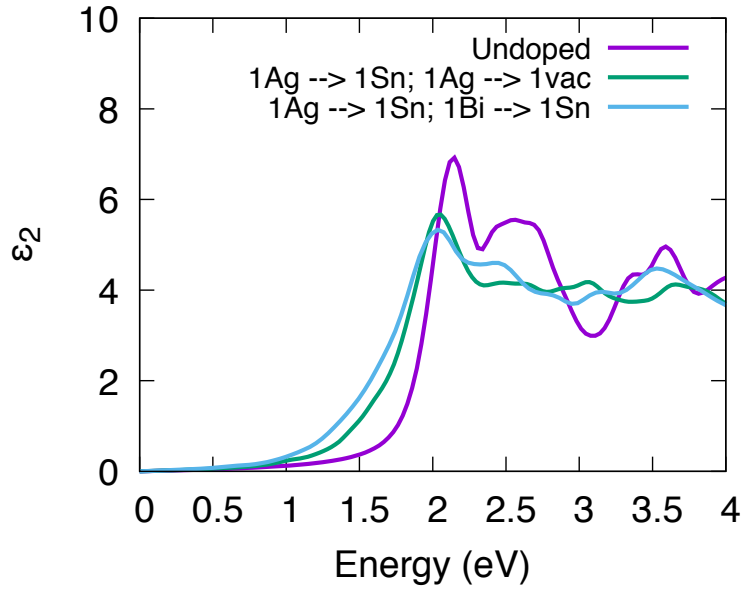

Figure 4.9: The imaginary part of the dielectric function as a function of energy is computed within the independent particle approximation. The undoped $Cs_2AgBiBr_6$ and two substitution patterns are computed showing a decrease in the energy onset.

while Sn^{4+} substitutes at the Bi^{3+} site, collectively generating anionic Ag^{+} vacancies as the dominant charge-compensating defect. The DFT calculations of the band structure show that the introduction of new bands with Sn^{4+} $5s^0$ impurity character below the conduction band minimum of the host lattice effects the large band gap reduction seen in Sn–alloyed $Cs_2AgBiBr_6$ (1 atom% Sn), successfully mimicking the band gap reduction resulting from Tl^{3+} incorporation in $Cs_2AgBiBr_6$ [8] in a nontoxic composition (Fig. 4.3). Thus, heterovalent alloying further expands the considerable compositional diversity of double perovskites for finding functional analogues to the lead perovskites.

Chapter 5

High compression-induced conductivity in $(EA)_2CuBr_4$

> "You have to make an offering to the Hubbard U gods and pray that they give you a value"
>
> *September 12, 2019*

This chapter is primarily adapted from [117].

Layered or two-dimensional (2D) Cu-Cl perovskites are translucent yellow insulators. These crystalline solids have been examined under pressure for decades, revealing their pronounced structural and electronic evolution upon compression [118, 119, 120, 121, 122, 123, 124, 125]. Motivation for their study has come, in part, from their similarities to the cuprate superconductors, whose superconducting transition temperatures (T_c) show a large pressure response [126, 127, 128]. In addition, the possibility of mechanically suppressing the Jahn-Teller (JT) distortion of the Cu(II) centers has motivated numerous high-pressure studies [118, 119, 120, 121, 122, 123, 124, 125]. This JT distortion results from the Cu $3d^9$ electronic configuration that drives a tetragonal elongation of the corner-sharing Cu-X (X = halide) octahedra (Fig. 5.1), where the elongated bonds lie along the inorganic sheets. Although the singly occupied Cu $d_{x^2-y^2}$ orbitals could produce a half-filled electronic band, this conduction pathway is disrupted by the antiferrodistortive alignment of the elongated X-Cu-X axes [129, 130]. The poor overlap between copper-derived half-filled orbitals therefore yields an electronic structure that is almost molecular in nature. Indeed, 2D Cu-X perovskites order ferromagnetically within their inorganic layers below T_c values as high as 72 K due to the orthogonality of the orbitals containing unpaired spins [131]. Prior efforts to remove this orbital orthogonality through material compression [118, 120] have elicited strong structural and piezochromic responses. At $\sim$ 4 GPa, 2D Cu-Cl perovskites turn translucent red and structural studies have provided evidence for phase transitions resulting in octahedral tilting (rotations) [119,

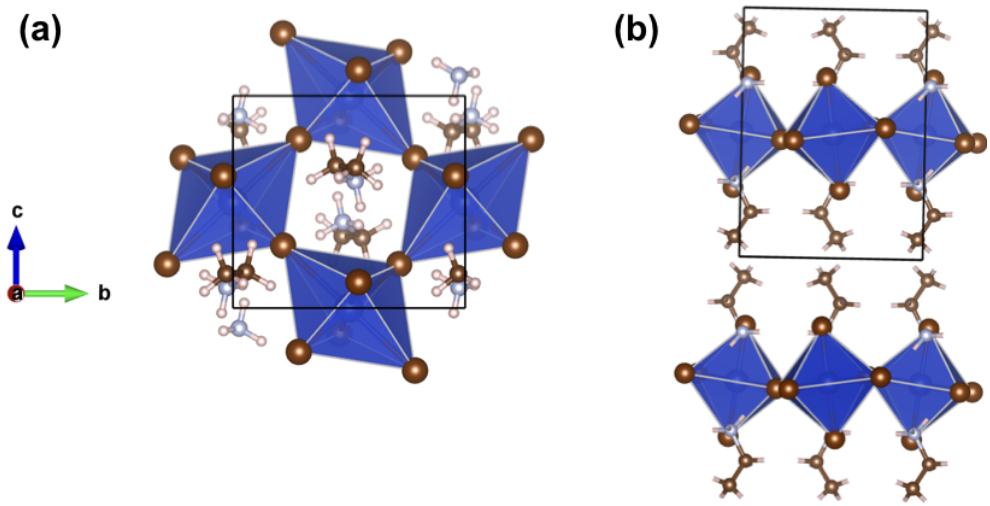

Figure 5.1: Ambient-pressure DFT-optimized structure of $(EA)_2CuBr_4$ using PBE + TS vdW functional. The Cu atoms are at the center of the octahedra in blue, Br atoms are shown in brown, and the organic ethyl-ammonium molecular link the inorganic layers.

121, 122], which can induce partial overlap between Cu $d_{x^2-y^2}$-derived orbitals. However, the materials remained insulating at these pressures. The first example of electronic transport in a layered Cu-Cl perovskite was reported in [132], albeit at very high pressure [123]. This conductivity was attributed to a combination of Cu-Cl bond compression and octahedral tilting, which in concert could provide a conduction pathway. By $\sim$ 12 GPa, the Cu-Cl perovskite $(EDBE)CuCl_4$ (EDBE = 2,2-(ethylenedioxy)bis(ethylammonium)) appeared opaque black and at 51 GPa a maximum conductivity of 2.9×10^4 S·cm^1 was measured with an activation energy of conduction (E_a) of 0.218(5) eV [123]. Herein we show that the pressure required to obtain appreciable electronic conductivity in Cu-X layered perovskites can be reduced by more than 50 GPa upon replacement of Cl with Br. Electronic conductivity as high as $1.98(8) \times 10^3$ S·cm^1 can be attained at only 2.6 GPa in a 2D Cu-Br perovskite. Replacement of Cl with Br also yields a large decrease in the ligand-to-metal charge-transfer (LMCT) band gap from $\sim$ 2.6 to 1.7 eV at ambient pressure. Compression of the CuBr perovskite affords a large band gap reduction, leading to a band gap of $\sim$0.3 eV at 65 GPa, which is projected to close at 77 GPa.

5.1 Experimental results

The $(EA)_2CuBr_4$ samples were found to undergo several structural phase transitions with increasing pressure applied using diamond-anvil cells (DACs) as discussed in [117]. Powder x-ray diffraction measurements (PXRD) were used to find that the volume of the α phase

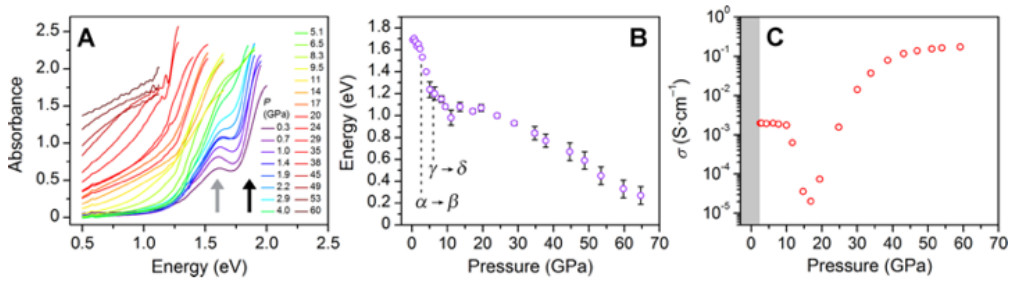

Figure 5.2: (A) Variable-pressure absorption spectra for $(EA)_2CuBr_4$ at visible and IR wavelengths, showing the redshift of the band gap with increasing pressure up to 60 GPa. The d-d (gray arrow) and LMCT transitions (black arrow) are clearly resolved at lower pressures. B) Estimated band gaps from the absorbance spectra in (A) as a function of pressure. Dotted lines indicate structural transition pressures, which coincide with changes in the slope. C) Variable-pressure conductivity of $(EA)_2CuBr_4$. The gray area denotes the lack of measurable conductivity (σ) below 2.6 GPa ($\sigma < 10^8 S \cdot cm^1$). Figure adapted from [117]

(ambient pressure structure) decreases up to 1.5 GPa at which point there is a first-order phase transition to the β phase which is complete at 2.6 GPa. Above 4 GPa there is increased stiffness and reduced compressibility suggestive of a second-order, isostructural phase transition to a γ phase. Another first-order phase transition occurs above 6 GPa as indicated by significant diffraction peak splitting to a δ phase. While there are hypotheses as to the space group symmetries of these higher pressure phases, only the α phase is reliably determined and has a P21/c space group.

The band gap is approximately 1.6 eV and hypothesized to arise due to a Cu d–d transition, analogous to the Cu–Cl perovskites. There is a stronger absorption onset at $\sim$ 1.7 eV which was assigned to a ligand-to-metal charge-transfer (LMCT) transitions from orbitals with bromide p character to one with mostly Cu d character. This LMCT band has a higher-energy onset of $\sim$ 2.6 eV in CuCl perovskites, due to the lower-energy Cl 3p orbitals compared to the Br 4p orbitals. Thus, replacement of Cl with Br decreases the LMCT band gap by 0.9 eV, reflected in the color of these solids, with Cu-Cl perovskites appearing translucent yellow and Cu-Br perovskites appearing dark purple with a metallic luster. With increasing pressure, the band gap is greatly reduced from 1.7 eV under ambient conditions to $\sim$ 0.3 eV at 65 GPa (Fig. 5.2). The rate of band gap change with pressure also tracks with the perovskite's structural relaxation, with changes in slope occurring at similar pressures to the $\alpha \rightarrow \beta$ and $\gamma \rightarrow \delta$ phase transitions. After the structural phase transition at 2.6 GPa there is an onset of conductivity with a very high value of 1.98(8) $\times$ 10^3 S·cm^1; an order of magnitude higher than the maximal value of the Cu–Cl perovskite which was measured at 51 GPa.

Method	a (Å)	b (Å)	c (Å)	$\beta(^\circ)$	Volume ($Å^3$)	Cu–Br equatorial bond lengths (Å)
Experimental (unrelaxed)	11.40	7.95	7.72	109.6	658.50	2.43 / 3.14
PBE	12.29	8.14	7.72	110.3	725.05	2.44 / 3.26
PBE + TS vdW	11.90	7.99	7.45	111.6	658.52	2.43 / 3.12
PBE + D3 vdW	11.80	7.79	7.39	112.2	628.68	2.46 / 2.96

Table 5.1: Calculated lattice parameters and Cu–Br bond lengths comparing different exchange-correlation functionals. Van der Waal's corrections improve the lattice parameters as expected for this hybrid organic-inorganic halide material, and in particular PBE + TS vdW provides very good agreement with the experimental volume and Cu–Br bond lengths, the main difference being the **a** lattice parameter is overestimated by 4%, which is along the direction of the organic ethyl-ammonium molecules.

5.2 Calculation details and results

The DFT calculations were done within the VASP–PAW formalism. Two different exchange-correlation functionals were used: 1) PBE with van der Waals corrections according to Tkachenko–Scheffler and a Hubbard U correction of 8 eV and 2) the HSE06 functional. We find the spin–orbit coupling has a minimal effect of the reported results and so was not included. The energy cutoff is 520 eV and a Γ-centered k-grid of 4×6×6 is used. The pseudopotentials for the calculations include 11 valence electrons for Cu ($3d^{10}4p^1$), 7 for Br ($4s^24p^5$), 5 for N ($2s^22p^3$), and 4 for C ($2s^22p^2$). The structural relaxations are performed without SOC, allowing the internal coordinates and volume to relax, until Hellmann–Feynman forces are less than 0.01 eV/Å. Calculated and experimental structural parameters can be found in Table 5.1.

The structure was relaxed, allowing the volume and internal coordinates to relax, using spin–polarized (FM ordering on Cu atoms) until the Hellmann–Feynman forces are less than 0.1 meV/Å. Different exchange–correlation functionals were tested and PBE + TS vdW was found to most closely reproduce the experimental structure volume (see Table 5.1 and the Cu–Br bond lengths in the inorganic octahedral layers, while the organic ethylammonium molecules were found to be more compressed in the DFT relaxed structure compared to the experimental structure. To accurately calculate the electronic structure, we tested different magnetic orderings and Hubbard U corrections on the Cu d orbitals. We find, in agreement with prior experimental and similar theoretical works on analogous copper chloride systems [133, 134, 135], that ferromagnetic ordering is the preferred magnetic ground state at T = 0 K with no applied pressure (for values of U from 0 to 8 eV applied to the Cu d states, see Fig. 5.3). The coupling between the magnetic atoms is found to be weak, as evidenced by the similarity in electronic structure between FM and AFM ordering (see below), and we therefore use spin–polarized calculations, initialized with ferromagnetic ordering, for the

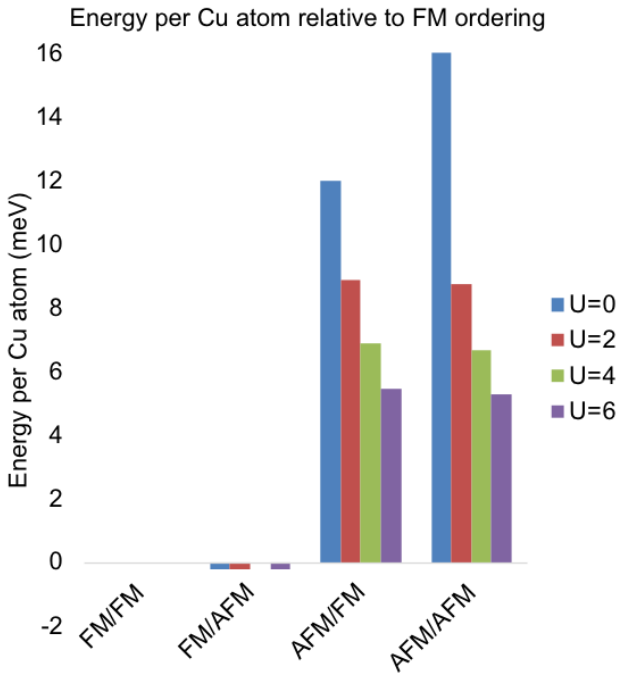

Figure 5.3: Energies per Cu atom for different magnetic orderings (listed in terms of intraplane/interplane) relative to having all the Cu atoms ferromagnetically aligned. The out-of-plane coupling is weak, and the ferromagnetic ordering in-plane is slightly preferred, for all U values calculated, over antiferromagnetic ordering.

subsequent HSE and pressure–dependent calculations presented here. We include a Hubbard U correction of 8 eV on the Cu d states to more closely reproduce the experimental and HSE gap for the DFT–PBE + vdW + U calculations of $(EA)_2CuBr_4$ under pressure and with different magnetic orderings. The HSE06 calculation uses a reduced cutoff energy of 400 eV to reduce computational expense, and is used for the density of states for both $(EA)_2CuBr_4$ and the analogous Cu–Cl perovskite.

We calculated the electronic properties of $(EA)_2CuBr_4$ and performed structural relaxations were performed PBE + TS vdW [136, 137]. Comparing calculated total energies for nonmagnetic, ferromagnetic (FM) and antiferromagnetic (AFM) orderings, FM order was found to be energetically preferred, as observed experimentally below a T_c of 11 K [138] (see Fig. 5.3). It is important to include spin explicitly, as seen in Fig. 5.6 where performing a non-spin-polarized (nonmagnetic) calculation results in a metallic state whereas a spin–polarized calculation opens up a gap between the predominantly Cu–d states around the Fermi energy. For both FM and AFM orderings, similar density of states are observed in Fig. 5.7 indicating the weak coupling between Cu atoms. We show the computed density of states (DOS) of the AFM and FM ordered structure at zero pressure, including a Hubbard U correction [139]. of 8 eV on the Cu d orbitals to account for the on-site Coulomb repulsion of

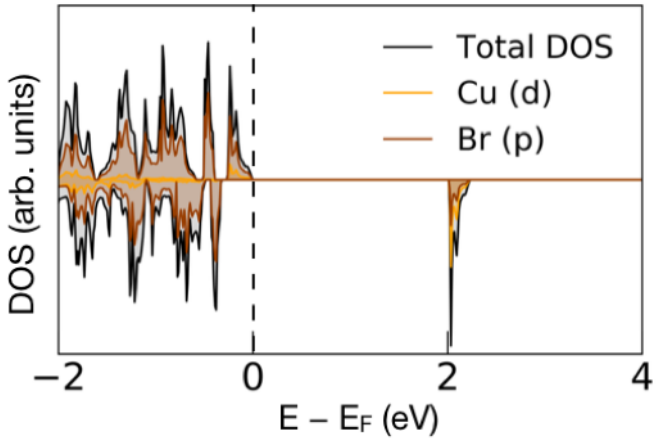

Figure 5.4: Spin-polarized density of states for $(EA)_2CuBr_4$ calculated with HSE06.

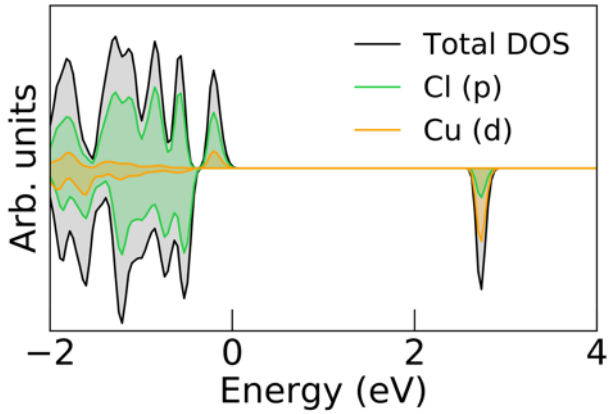

Figure 5.5: Spin-polarized density of states for $(EA)_2CuCl_4$ calculated with HSE06.

localized electrons, in Fig. 5.7. The computed DOS is qualitatively consistent with Laporte forbidden Cu d-d transitions as the lowest-energy transition, although the states involved also have significant halide character, as expected for anti–bonding metal–ligand orbitals. The next highest energy occupied states below the Fermi energy have mostly Br p character, which are consistent with dipole-allowed transitions to the conduction band minimum (CBM) and a nominal LMCT gap. The next set of unoccupied states are 4 eV above the Fermi energy.

We find that the Cu d states are spin split, with spin–up and spin–down orbitals below and above the Fermi energy, respectively. We quantify the orbital contributions using our HSE [140] calculations of the DOS for the FM phase at zero pressure (see Fig. 5.4), which agree well with our PBE+vdW+U calculations (Fig. 5.7). The highest–energy filled state,

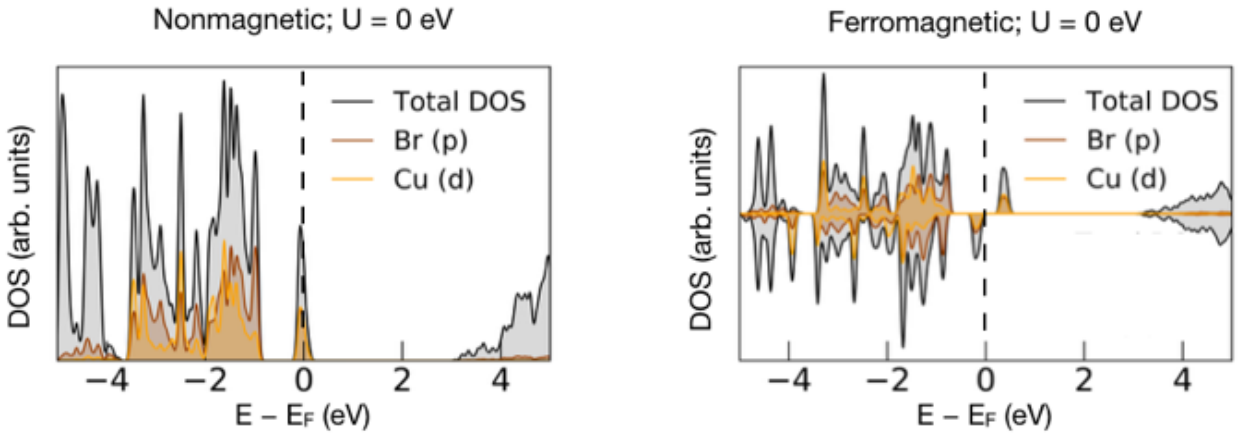

Figure 5.6: Density of states for $(EA)_2CuBr_4$ calculated with DFT-PBE+vdW for nonmagnetic (left) and ferromagnetic ordering (right).

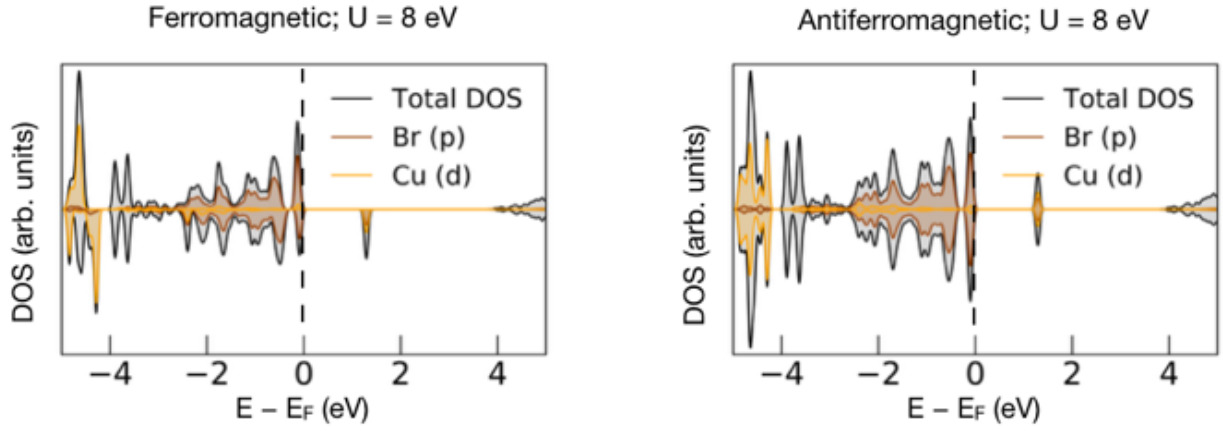

Figure 5.7: Density of states for $(EA)_2CuBr_4$ calculated with DFT-PBE+vdW+U for ferromagnetic (left) and antiferromagnetic ordering (right) with U = 8 eV.

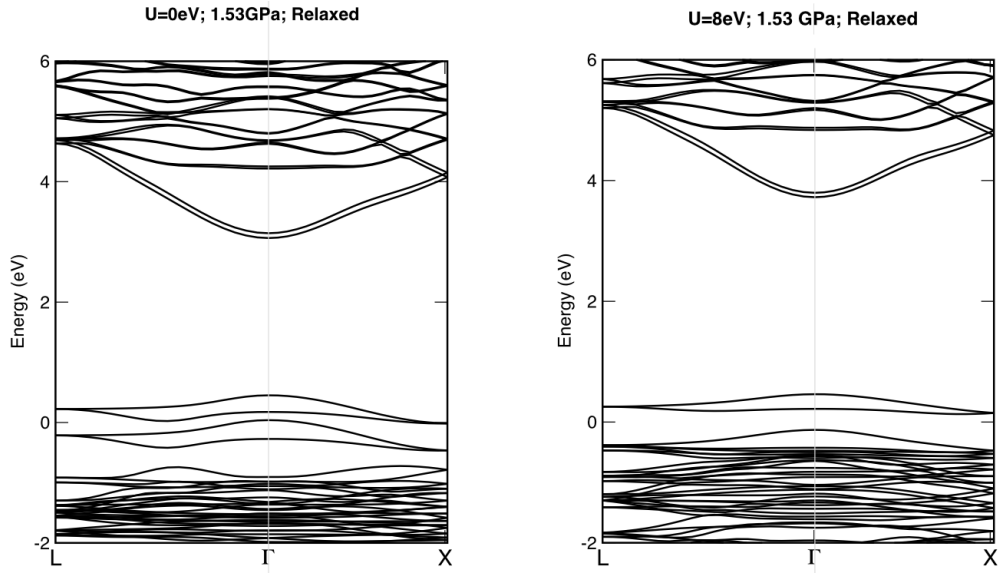

Figure 5.8: Electronic band structures for $(EA)_2CuBr_4$ calculated with DFT–PBE + TS vdW + U = 8 eV (on the Au d states) for ferromagnetic ordering at 0 (left) and 1.53 GPa (right).

or valence band maximum (VBM), has 75% Br p orbital character and 22% Cu d character whereas the conduction band minimum (CBM) has 63% Cu d orbital character and 35% Br p contributions. In the analogous Cu-Cl perovskite (Fig. 5.5), the relative contributions of Cl and Cu states in the CBM are 30% and 69% respectively, and the VBM has 27% Cu d character and 72% Cl p character, consistent with prior calculations [133, 134, 135]. The greater halide contribution in the predominantly d–orbital bands of the Cu-Br perovskites compared to the Cu-Cl perovskites corroborates the hypothesis that the Br compound possesses greater covalency, consistent with the enhanced conductivity of the Cu-Br perovskite.

To further investigate the effect of pressure on the structure, we relaxed the structure with increasing isotropic pressure. We performed constant–pressure relaxations, and optimizing the cell volume and internal coordinates at fixed pressure using PBE + TS vdW with U = 8 eV included on the Cu d orbitals. Here, for consistency with the DFT predicted ground state of FM ordering, we continue only using FM ordering. Within the predicted pressure stability range of the α phase below 2.6 GPa, we note a slight reduction in both the JT distortion and octahedral tilting with increased pressure. We find the ratio of long and short equatorial bond lengths from our DFT calculations for the Cu-Br octahedra to be reduced from 1.28 to 1.17. The slightly decreased octahedral tilting is evidenced by the increase of the in–plane Cu-Br-Cu angle from 160° to 165°. At a computed pressure of 20 GPa, the DFT relaxed α phase structure continues to exhibit a reduction in JT distortion, approaching nearly equal equatorial bond lengths, with a bond length ratio of 1.03. The computed in–plane Cu-Br-Cu angle increases slightly to 168°. These calculations do not include the observed phase

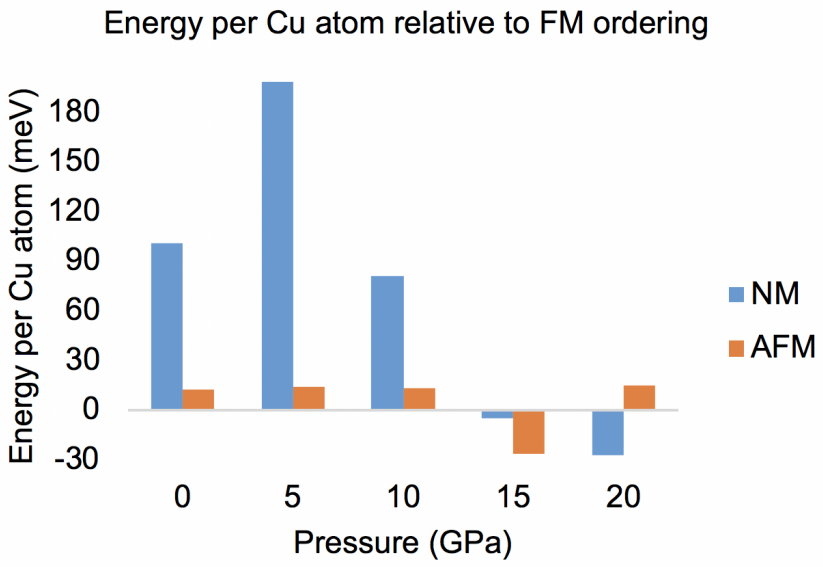

Figure 5.9: Comparison for energy per Cu atom with nonmagnetic vs. antiferromagnetic ordering as a function of pressure from 0 to 20 GPa.

transitions that are likely associated with large changes in octahedral tilting, which could not be considered here without knowledge of the atomic coordinates of the β and γ phases.

We also investigated the preferred magnetic ordering and at ambient pressure it is found that ferromagnetic ordering is preferred. The in-plane AFM ordering is only 10 meV/Cu atom higher in energy, and the intralayer magnetic ordering had negligible effect on the total energies. With increasing pressure, the ferromagnetic ordering is preferred up to 10 GPa at which point the nonmagnetic ordering becomes competitive (see Fig. 5.9 indicating a magnetic–nonmagnetic transition. We note that the structure is relaxed at pressures between 0 to 20 GPa in 5 GPa intervals, with the α phase structure as a starting point. Thus, loss of ferromagnetism is also consistent with the loss of orthogonality between the primarily $d_{x^2-y^2}$ orbitals, suggesting this as a possible explanation of the emergence of greater conductivity as the JT distortion is suppressed, though more information is needed to strongly make this conclusion.

5.3 Conclusion

Layered Cu-Cl perovskites have shown appreciable electronic conductivity of $10^4 S \cdot cm^1$ only at pressures exceeding 50 GPa, whereas their conductivity is $\sim 10^9$ at 7 GPa. Herein we demonstrate a six order–of–magnitude increase in conductivity in copper–halide perovskites, upon moderate compression, through replacement of Cl with Br. A conductivity of $10^3 S \cdot cm^1$

can be obtained in layered Cu-Br perovskites at only 2.6 GPa, with the highest conductivity of $10^1 S \cdot cm^1$ measured at 59 GPa. These dramatic improvements in pressured-induced properties may be attributed to a more facile structural response to mechanical compression and increased orbital overlap due to higher–energy and more diffuse Br orbitals relative to the Cl analogues.

We attribute the sudden onset of electronic conductivity at 2.6 GPa in $(EA)_2CuBr_4$ to octahedral tilting in the $\alpha \rightarrow \beta$ phase transition that can partially remove the orthogonality between singly occupied $d_{x^2-y^2}$–derived orbitals and provide a conduction pathway, albeit with thinly dispersed electronic bands. The sudden onset of conductivity is more likely due to the pressure-induced formation of half–filled electronic bands by partially relieving the orthogonality between singly occupied molecular orbitals composed of Cu d and Br p orbitals. At higher pressures, particularly in the γ phase when the perovskite's compressibility suddenly decreases 4–fold, we expect Cu–Br bond compression to drive the increase in conductivity through both a reduction in band gap and increase in band dispersion.

Chapter 6

Compositional effects on optoelectronic properties of $A_8B_5X_{23}$ halide perovskites

"Not to beat a dead horse, but..."

February 23, 2019

In this last chapter related to halide perovskites, we studied a material which demonstrates how different connectivities are possible within the 3D bulk perovskite structure. If one considers a 2×2×2 supercell of a conventional ABX_3 perovskite and remove the face-center octahedra, then one is left with corner sharing octahedra around the supercell face edges and an unconnected octahedra in the centre. In the material studied, the octahedra along the edges are formed of Au atoms on the B site and Cl atoms as the halide anion. Interestingly, the experiment indicates that these are only fully occupied octahedra and there is only 5/6 of the nominal Cl charge surrounding these Au atoms, which will be discussed further in the calculation details. The central octahedron is fully coordinated, but the B site was synthesized with both Bi and In. These were also synthesized with Br instead of Cl as the halide anion. This presents a certain amount of complexity for modeling these materials, as based on charge counting the Au atoms is actually d^8 and the lack of fully coordinated corner octahedra means that we must introduce a vacancy, since if we include 6 Cl atoms the system is no longer charge balanced and indeed has metallic character when calculated. As such, we treat spin explicitly and perform spin polarized calculations in order to accommodate the open d shell of the Au atoms and need to carefully consider the effect of disorder on the optoelectronic properties calculated.

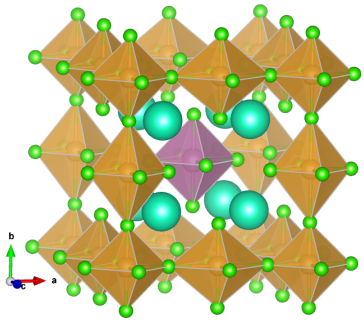

Figure 6.1: $Cs_8Au_4InCl_{23}$ structure. The Au, Cl, In, and O atoms are denoted by orange, green, purple, and turquoise respectively. This structure is achieved by starting from a conventional 3×3×3 supercell of a halide perovskite, ABX_3, and removing the octahedra on the face centers. As such, there is a corner-sharing network or $AuCl_6$ octahedra around the edges surrounding an isolated $InCl_6$ octahedron in the body-center. In order to be charge neutral, one of the octahedra actually has 5/6 electron occupancy in order to achieve the unique chemical formula of $A_8B_5X_{23}$ in the case where the B-site cation has a 3+ oxidation state. In this $Cs_8Au_4InCl_{23}$ case, the corner Au–Cl octahedra is found to have 5/6 electronic occupancy by experiment. There is chemical flexibility in terms of the composition of this material, and it has synthesized with In, Bi, and Sb occupying the center of the body-center octahedra (here depicted with In).

	$Cs_8Au_4InCl_{23}$	$Cs_8Au_4BiCl_{23}$	$Cs_8Au_4InBr_{23}$	$Cs_8Au_4BiBr_{23}$	$Cs_8Au_{4+x}In_{1-x}Cl_{23}$
E_g (expt.)	1.97 eV	1.79 eV	1.49 eV	1.55 eV	1.26 eV (x = 0.12)

Table 6.1: The measured band gaps of different $Cs_8Au_4XCl_{23}$ chemical compositions: comparing different center B-site cations; X = In, Bi; and Au alloying on the In site.

6.1 Experimental results

Experimentally, a number of related structures were synthesized [141] with different central octahedra B-site cations (In, Bi, and Sb) as well as different halide anions (Cl and Br). These changes had noticeable effects on the measured band gap as shown in Table 6.1.

6.2 Structural details and electronic structure

We perform calculations with VASP–PBE with an energy cutoff of 500 eV and a $7 \times 7 \times 7$ k-grid density. We include 13 electrons as valence for In; 9 for Cs; 11 for Au; and 5 for

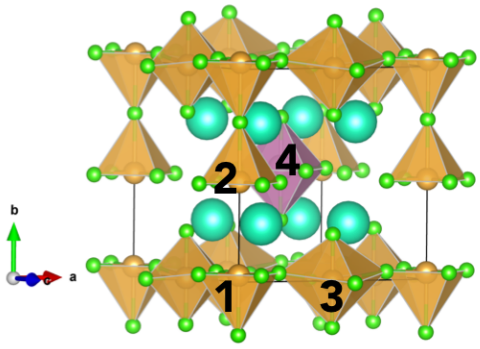

Figure 6.2: $Cs_8Au_4InCl_{23}$ structure. We test removing a Cl atom from the four different octahedral environments: corner, two edge-centers, and body-center which are labeled 1, 2, 3, and 4 respectively.

Bi in our pseudopotentials. Interestingly, Au is nominally in a 3+ oxidation state (from a simple counting argument – in order for the structure to be charge neutral, since there are $\{8\times Cs^{1+}\}$ + $\{In^{3+}/Bi^{3+}\}$ + $\{23\times Cl^{1-}\}$ this leaves the 4 Au atoms to assume the remaining 12+ charge). Therefore, this implies that Au has an open d shell and can be in a high or low spin state with its 6 d electrons. We perform spin-polarized calculations, including a Hubbard U = 3 eV on the Au d states. We find that even when initializing the spins on the Au atoms with a high spin configuration that it relaxes to having negligible magnetic moment, suggesting that initializing in a low spin configuration is reliable. We also tested the effect of spin-orbit coupling, given that the material contains heavy elements, and while it does have a small effect on the electronic structure as discussed later, the atomic structure is not affected by the inclusion of SOC.

One unique challenge in calculating this material, is that with 23 chlorine atoms, one of the gold octahedra is not fully coordinated. The experimentalists find that there is disorder such that there is 5/6 electron occupancy for the corner octahedron. We decide to model this by removing one of the chlorine atoms such that the corner octahedra are five-fold coordinated. While this may result in a change in the connectivity, we tested the effect on the energetics depending on which chlorine is removed from that corner octahedra, and furthermore in comparison with removal of the chlorine from different octahedra. We compared removing the Cl from different octahedra in the crystal structure by calculating the total energy using the high symmetry, cubic structure without relaxation. We find that removing the Cl from the corner octahedron, labeled 1 in Fig. 6.2, is energetically preferred by 23 meV/atom over removal from the edge-center octahedra (labeled 2 and 3 in Fig. 6.2) and by 39 meV/atom over removal from the body-center octahedron (4); these trends did not change upon constant volume relaxation. This is in line with the experimental structural refinement suggesting that it is the corner octahedron which has 5/6 Cl occupancy. One can rationalize this since the corner octahedra has the least orbital overlap with the central octahedra and

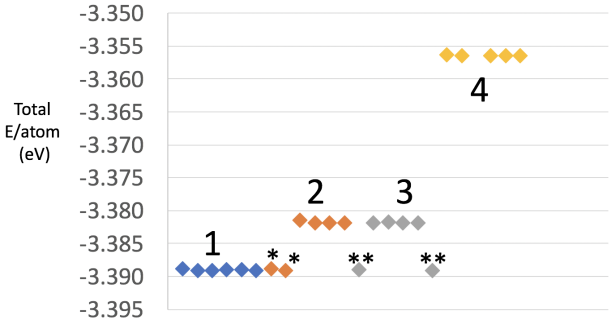

Figure 6.3: The total energy per atom of the $Cs_8Au_4InCl_{23}$ structure with the Cl atom removed from the different octahedra, labeled in accordance with 6.2. There is little variation depending on which chlorine atom from a given octahedron is removed; the exception being the cases denoted by: $*$ where the Cl is that which is shared on the **c** direction with 1 and $**$ where the Cl is that which is shared on the **a** direction with 1. The difference in energy between removal from octahedron (2 or 3) and 1 is 23 meV, between removing Cl from octahedra 4 and 1 is 39 meV, suggesting that it is slightly energetically preferred for the Cl to be removed from the corner octahedron.

is only influenced by the Au–Cl scaffolding. Furthermore the Jahn-Teller distortion is less pronounced in the corner octahedra as compared to the edge-center octahedra, as further explicated below in the structural comparison.

In the experimental synthesis, both fast and slow cooling was used during the sample preparation with slightly varying results. As such, both a high-symmetry, cubic $Pm\bar{3}m$ structure and a lower-symmetry, tetragonal $P4mm$ structure are reported. It is believed that during the fast cooling, the halide vacancies remain disordered throughout the sample and there is an averaging of their spatial locations resulting in a cubic structure. However, during the slow cooling there appears to be a symmetry reduction based on the PXRD patterns measured on the powder samples. This tetragonal distortion is likely due to an ordering of the halide vacancies on the corner octahedra. There is a distortion of the Au–Cl bond lengths in the corner octahedra which reflects this with the corner Au has equatorial bond lengths of 2.29 Å and the axial bond length opposite the vacancy is 2.92 Å; however due to the small change in lattice parameters the SC–XRD was not sufficiently precise to determine the change in lattice parameters.

It was found that including the Hubbard U correction on the Au d states and spin–orbit coupling did not have a large effect on the structural relaxations (see Table 6.2 and Table 6.3). We performed relaxations starting from both the cubic and tetragonal lattice parameters provided from experiment. The main difference between these relaxations are that when starting from the tetragonal structure, the compression along the direction of the vacancy was slightly smaller, but only by less than 0.5% of the lattice parameter. As

	Expt Cubic $Pm\bar{3}m$	Expt P4mm	Relaxed from $Pm\bar{3}m$ (no U/no SOC)	Relaxed from $Pm\bar{3}m$ (with U/with SOC)	Relaxed from P4mm (no U/no SOC)
a (Å)	10.48	10.42	10.82	10.81	10.82
b (Å)	10.48	10.38	10.68	10.67	10.72
c (Å)	10.48	10.42	10.82	10.81	10.82
volume (Å^3)	1150.07	1147.65	1250.33	1246.15	1255.75
E_g (eV)	0.13	0.69	0.68	0.73	

Table 6.2: The computed DFT–PBE lattice parameters for the experimental lattice parameters (first two columns; resulting from the slow and fast cooled synthesis processes) and after relaxation (remaining three columns; starting from the experimental cubic lattice parameters in columns 3 and 4 and the experimental tetragonal lattice parameters in the final column) and computed band gaps for $Cs_8Au_4InCl_{23}$, initialized in a low–spin configuration. The experimental band gap is measured to be 1.97 eV.

	Experimental Cubic $Pm\bar{3}m$	relaxed from $Pm\bar{3}m$ (no U / no SOC)
a (Å)	10.51	10.85
b (Å)	10.51	10.74
c (Å)	10.51	10.85
volume (Å^3)	1161.93	1264.05
E_g	0.31 eV	0.76 eV

Table 6.3: DFT–PBE lattice parameters after relaxation and computed band gaps for $Cs_8Au_4BiCl_{23}$, initialized in a low–spin configuration. The experimental band gap is measured to be 1.79 eV. Since starting from either set of experimental lattice parameters had minimal effect on the fully relaxed structure of $Cs_8Au_4InCl_{23}$, and including a U on the Au d electrons and including SOC also had minimal effect, here we simply start from the cubic lattice parameters and use PBE for the relaxation.

one might expect given the difference in atomic size, the lattice parameters with Bi in the isolated body-center octahedron are slightly larger than the analogous structure with In. We find these effects to make a difference in terms of the degree of octahedral tilting in the structure as discussed later.

The difference in our calculated DFT–PBE band gaps are small, where the $Cs_8Au_4InCl_{23}$ gap is only 80 meV smaller than the $Cs_8Au_4BiCl_{23}$ gap; as one would expect using PBE we are underestimating the experimental band gaps. Qualitatively the trends are in contrast to the experimental results which indicate that the $Cs_8Au_4BiCl_{23}$ gap is smaller by 180 meV. The structural differences between the fully relaxed tetragonal phases of these two materials

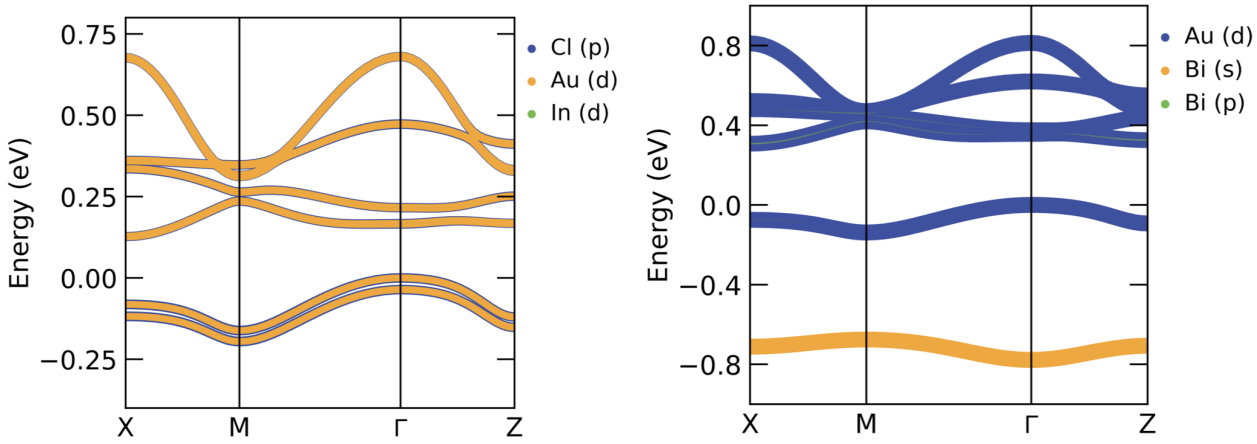

(a) DFT–PBE orbital projected band structure for $Cs_8Au_4InCl_{23}$.

(b) DFT–PBE orbital projected band structure for $Cs_8Au_4BiCl_{23}$.

Figure 6.4: The DFT–PBE orbital projected band structures for (a) $Cs_8Au_4InCl_{23}$ and (b) $Cs_8Au_4BiCl_{23}$. The Fermi energy is set to zero in both cases (note the y-axes are of different scales). In both cases, the center B site (In or Bi) do not contribute at the band edges. The In contributions are negligible in the vicinity of the Fermi energy (less than $< 1\%$ and the Bi s are hybridized with bands that are $\sim$0.8 eV below the Fermi energy, below the VBM which lies nearly at E_F. This suggests that the structural effects due to the different lattices strongly influence the band gap.

are rather small, mainly resulting in the difference in the lattice parameters. With the larger Bi atom, one would expect larger lattice parameters in agreement with our calculations. As such, the orbital overlap is reduced and therefore the dispersion of the bands in the calculated electronic band structure is reduced, resulting in slightly flatter bands and therefore a slightly larger band gap. In contrast, a smaller lattice leads to more orbital overlap, greater dispersion, and slightly smaller band gap. This geometrical argument appears to be sufficient to explain the small differences in band gaps in our calculations, if not the experimental results. We also examine the projections of the orbital character of the bands (see Fig. 6.4) and find that neither indium nor bismuth contribute to the VBM or CBM, suggesting that while they do change the lattice parameters since they have different atomic sizes, so the $Cs_8Au_4BiCl_{23}$ lattice is slightly larger than that of $Cs_8Au_4InCl_{23}$, they do not directly affect the band edge properties due to their chemistry.

However, we note that during the relaxation from cubic to tetragonal the change in octahedral tilting, therefore orbital overlap and band gap, do change significantly. For both $Cs_8Au_4InCl_{23}$ and $Cs_8Au_4BiCl_{23}$ we begin from the cubic phase and linearly interpolate the structure to the relaxed structure, which include octahedral tilting as depicted in Fig. 6.5. Computing the band structure, we see a significant opening of the band gap, and slight flattening of the bands, as the distortion increases shown in Fig. 6.6 for the cubic/tetragonal

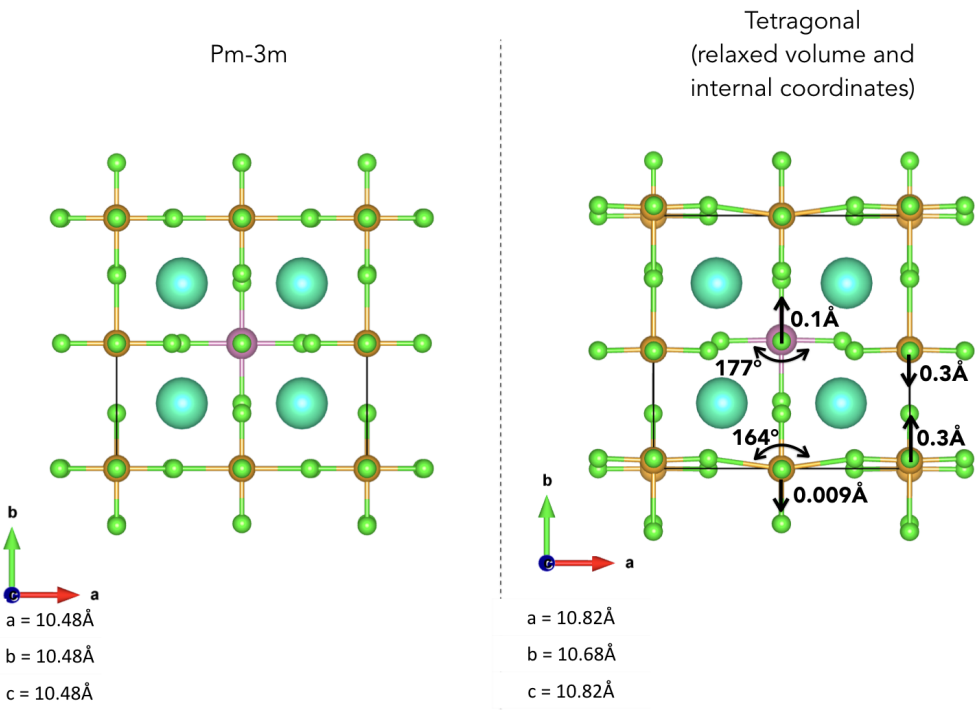

Figure 6.5: Structural distortion that occurs when relaxing using DFT–PBE from the cubic structure, the final structure is a tetragonal *P4mm* structure. We note that the octahedral tilting that occurs is similar to that of $Cs_8Au_4BiCl_{23}$, and we see a compression along the axis of the missing Cl atom.

endpoints of $Cs_8Au_4InCl_{23}$ and for $Cs_8Au_4BiCl_{23}$ in Fig. 6.7. As such, it suggests that the degree of structural disorder in the samples, depending on the synthesis where how quickly it is cooled determines whether the structure is able to form the high symmetry cubic phase or the lower symmetry tetragonal phase, would have an effect on its optoelectronic properties.

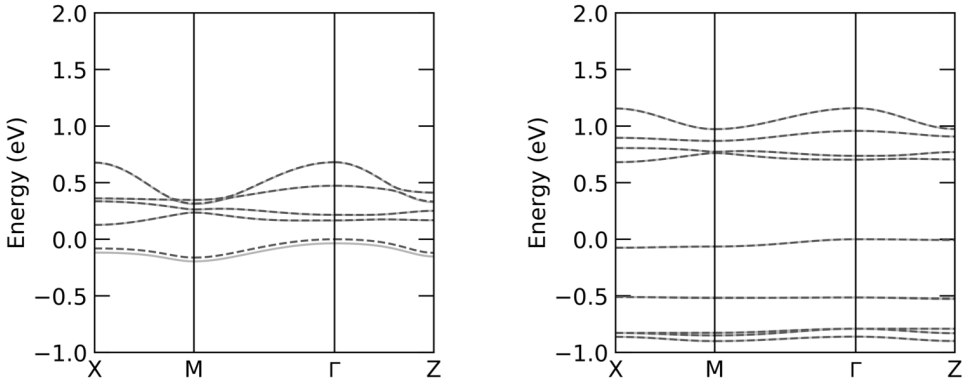

Figure 6.6: Here we show the DFT–PBE computed band structures of $Cs_8Au_4InCl_{23}$ in the cubic phase on the left and in the relaxed tetragonal phase on the right. The internal coordinates are allowed to relax while keeping the volume constant. we find that the octahedral tilting results in slightly flatter bands and an opening up of the band gap.

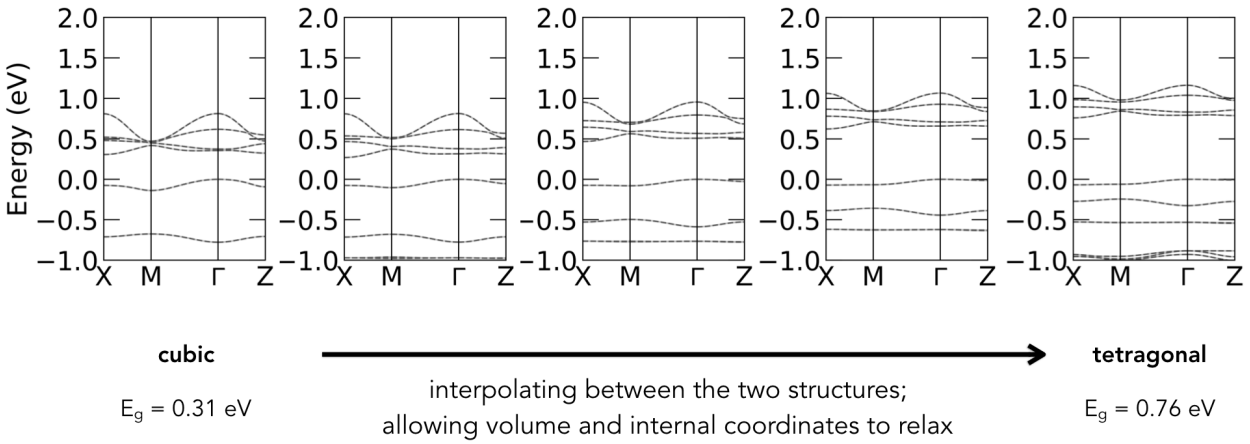

Figure 6.7: Similar to Fig. 6.6, here we show more interpolated structures from the cubic to tetragonal structure but for the $Cs_8Au_4BiCl_{23}$ structure and we see a similar effect to $Cs_8Au_4InCl_{23}$. The increased tilting causes a flattening of the bands and an opening of the band gap.

Chapter 7

Design of low work function perovskite oxide heterostructures

"Back in the good ol' days of 2015"

October 19, 2018

7.1 Motivation for thermionic devices

Understanding and controlling work functions, or band edge energies, is of interest for a variety of applications in optoelectronics and energy conversion. In particular, while recent advances in device design have improved the feasibility of thermionic generators, new low work function materials are needed to enable their widespread use. Current state of the art technology involves layers of Cs or W(001) surfaces or other such coverage-based approaches [142], however these elements can be reactive and coat the inner surface of a device. We thus approach the problem of designing a low work function material through designing heterostructures such that a coating layer is not needed. In the simplest model the work function is related to the dipole moment at the surface, or polarization per unit area, and so the problem is reduced to designing a material with a large out-of-plane polarization at the surface. Without compensating metallic electrodes enforcing short-circuit boundary conditions, electrostatics generally inhibits a large dipole moment via the depolarization field with the boundary conditions at the surface ($D = 0$), which is also known to reduce the Callen effective charges by almost an order of magnitude when compared to the bulk Born effective charges.

Perovskite-based oxides (ABO_3) are a diverse class of materials that, depending on the transition metal atoms on the A and B sites, can give rise to myriad emergent and collective phenomena. Our aim is to lower the work function by creating a strong dipole moment at the surface of the material. We use DFT calculations to examine how the work function of one such oxide, $SrRuO_3$, can be tuned by polar or near-polar ultra-thin overlayers in order to

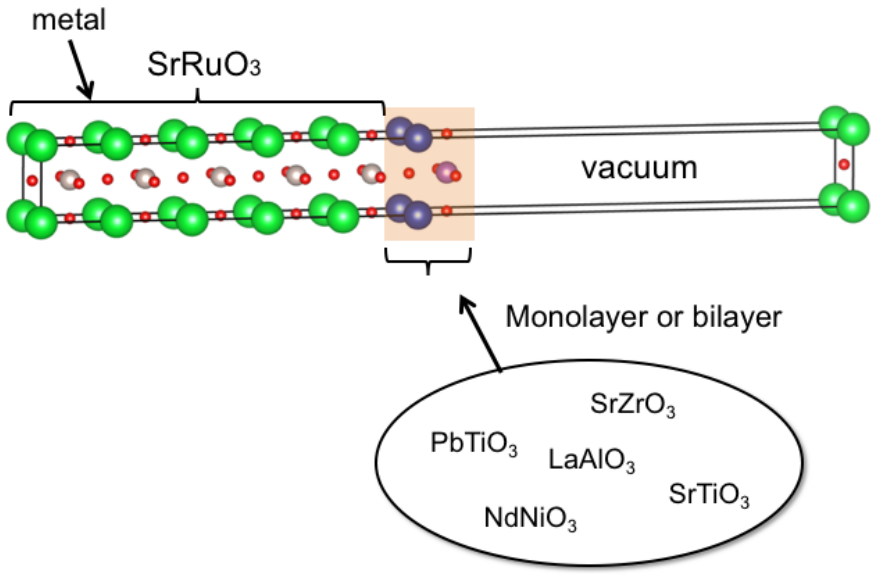

Figure 7.1: A slab of $SrRuO_3$ is constructed with 15 Å of vacuum between slabs. A monolayer or bilayer of a ferroelectric, or near-ferroelectric, perovskite oxide is layered on the surface. A dipole correction is introduced in the vacuum layer to correct for spurious interactions between slabs.

overcome the D=0 boundary conditions and create a polar surface structure with a positive dipole moment in order to achieve a lower work function. This is achieved through chemical substitution that will naturally break the compositional inversion symmetry at the surface with a thin perovskite oxide overlayer, either a monolayer or bilayer.

All of the calculations are done with the VASP–PAW formalism using the PBE exchange-correlation functional with spin-polarization. The plane-wave energy cutoff was 520 eV. The structure for the 5 atom $Pm\bar{3}m$ unit cell for $SrRuO_3$ was optimized with an 11×11×11 Monkhorst-Pack k-point mesh while the slab calculations were done with only 1 k-point in the direction of the vacuum layer, including a dipole correction in the vacuum layer to account for the spurious electric field arising from the periodic boundary conditions. Density functional perturbation theory (DFPT) as implemented in VASP was used to calculate the Born effective charges.

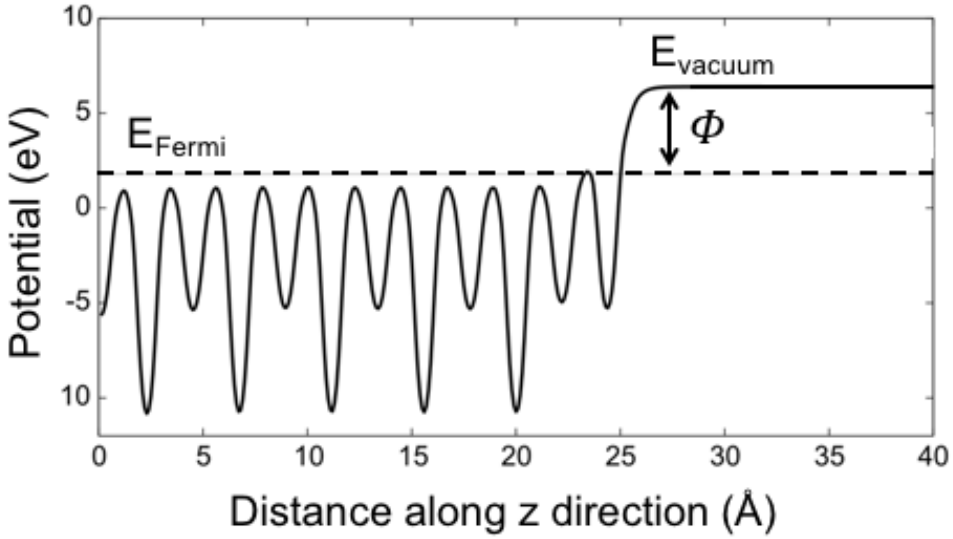

Figure 7.2: We average the electrostatic potential along the z-direction, here assumed to be the direction perpendicular to the slab surface. Computing the work function (the difference between the Fermi energy and the vacuum energy) for either termination is not affected by the symmetric or asymmetric terminations of the slab with a thick enough layer of $SrRuO_3$ and the dipole correction included.

7.2 Intuition from electrostatics

We explore how ultrathin films can be used to tune the work function of an oxide. Using a monolayer on the $SrRuO_3$ substrate we break the inversion symmetry by varying the surface chemical motif. Due to this and the lattice mismatch between the different oxides we assume any net polarization will be along the z-direction, where the surface will tend towards a pattern analogous to ferroelectric ordering with the oxygen octahedra and A/B cations displacing in opposite directions. These distortions along the z-direction would contribute to a surface dipole moment affecting the heterostructure's work function. There is a linear relationship between the change in work function Φ and dipole moment p based on electrostatics $\Delta\Phi \approx 4\pi\Delta p/A$ from the 1D solution to Poisson's equation. Therefore in order to achieve as large a reduction as possible it follows the surface polarization should be as large as possible since polarization $\vec{P}$ is related to the dipole moment through $\vec{P} = \vec{p}/\Omega$. Based on this, as a rough estimate one would need a polarization on the order of $2\mu\mathrm{C/cm}^2$ to achieve a 1 eV reduction in the $SrRuO_3$ work function. This is a relatively small polarization for a typical ferroelectric, considering that the well known example of $BiFeO_3$ has a polarization close to 100 $\mu C/cm^2$. Therefore that a ferroelectric with a far more modest polarization would in principle result in such a large reduction of the work function suggests that ferroelectric overlayers are promising for work function tuning; since the polarization is coupled

to the structural order parameter, one could conceivably vary the change in work function by coupling to that structural order parameter.

We initially consider a monolayer of $SrTiO_3$ on the $SrRuO_3$ substrate, where a monolayer is considered to be one unit cell consisting of individual SrO and TiO_2 layers. The $SrRuO_3$ substrate was found to match the experimental work function value at a thickness of five unit cells and 15 Å of vacuum was used between slabs, including a dipole correction [143] to account for the spurious electric field arising between adjacent slabs. The $SrTiO_3$ in-plane lattice parameters were constrained to 3.99 Å to match $SrRuO_3$ then allowed to relax out of plane. Upon relaxation, we find the monolayer increased the work function by only +0.12 eV, which is significantly lower in magnitude than would be expected based on the bulk properties. We can understand the variation in work function through the polarization of the $SrTiO_3$ monolayer, which can be estimated by analyzing the effective charges and displacements of the atoms. Effective charges are calculated using DFPT and they are referred to differently depending on the boundary conditions under which they are calculated. The Born (transverse) and Callen (longitudinal) effective charges denoted $Z^{*(T)}$ and $Z^{*(L)}$ respectively, are appropriate for bulk and surface boundary conditions, respectively, and are defined to first order as follows

$$Z^{*(T)}_{\kappa,\alpha\beta} = \Omega_0 \frac{\partial P_\alpha}{\partial \tau_\beta}|_{\mathcal{E}=0} \tag{7.1}$$

$$Z^{*(L)}_{\kappa,\alpha\beta} = \Omega_0 \frac{\partial P}{\partial \tau \beta}|_{D=0} \quad = \sum_j Z^{*(T)}_{\kappa,\alpha j} \frac{1}{\epsilon^{\infty}_{\beta j}} \tag{7.2}$$

for an atom κ, where α, β denote the Cartesian directions, Ω is the unit cell volume, P the polarization, τ the displacement, $\mathcal{E}$ and D the electric and electric displacement field respectively, and ϵ the dielectric function. We compute these quantities for the atoms in the overlayers using DFPT in order to understand the computed change in work function. As implemented in VASP, the static dielectric matrix is computed from the linear Sternheimer equation. From the dielectric matrix, Z^* can be computed as derivates of the Hellmann-Feynman forces using finite-differences [144].

7.3 Monolayers and bilayers

The Born effective charges illustrate the coupling between atomic displacements and polarization. They can be anomalously large in perovskite oxides, almost twice the nominal ionic charge indicating that perovskites have a large potential for developing significant polarizations with small atomic displacements. We focus on the $Z^*_{3,3}$ component, the component of the Callen charge tensor perpendicular to the slab surface, since we only need to consider the out-of-plane components to determine the changes in work function. As an aside, the diagonal components in bulk are identical and the surface components parallel to the slab are also essentially the Born effective charges[145]. However, as seen in Table 7.1, the effective

	$Z^*_{3,3}(bulk)$	$Z^*_{3,3}(surface)$
Sr	2.53	0.23
Ti	7.74	1.20
O1	-6.19	-0.96
O2	-2.04	-0.30

Table 7.1: The effective charges for $SrTiO_3$ comparing the 3,3 components of the effective charge tensor for the atoms in the bulk versus at the surface, demonstrating that the boundary conditions have a large effect on the magnitude of the effective charges.

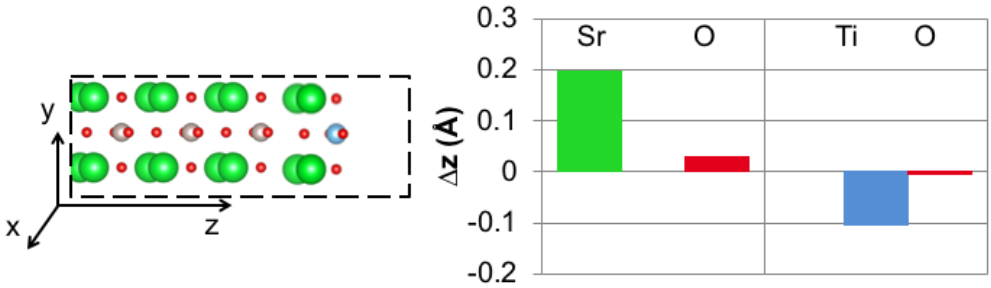

Figure 7.3: The panel on the left indicates the setup of the slab surface where a single monolayer of $SrTiO_3$ is on the slab of $SrRuO_3$ (the total unit cell calculated includes 5 unit cells of $SrRuO_3$ and 1 unit cell of $SrTiO_3$ with 15 Å of vacuum) while the panel on the right indicates the atomic displacements upon relaxation of the $SrTiO_3$ monolayer on $SrRuO_3$.

charges are strongly affected by boundary conditions [145]. At the surface where D=0 they are reduced by almost an order of magnitude from the bulk Born effective charges.

Furthermore, in the case of a single layer of $SrTiO_3$ the displacement of the atoms compensate for the difference in magnitude between atomic effective charges and so these two effects are in competition with each other resulting in a negligible dipole moment at the surface. Although there are large distortions, the net dipole moment is close to zero and therefore we see a minimal shift in work function.

This combination of oxides does not yield a strong deviation from the ideal centrosymmetric structure and so we tested if we could enhance the effect using heterovalent and chemical substitution by using a monolayer of $LaAlO_3$. We do see a reduction with $\Delta\Phi$ =-0.15 eV following the same method as before, constraining the $LaAlO_3$ layer to only relax perpendicular to the surface along the z-direction. Again, the effective charges and atomic displacement are such that the overall dipole moment is small, showing the tendency for the system to relax to a non-polar ground state which is consistent with what one expects from a depolarization field counteracting any surface polarization according to the electrostatic

	$Z^*_{3,3}(e)$ (bulk)	$Z^*_{3,3}(e)$ (surface)	$Z^*_{3,3}(e)$ (monolayer on $SrRuO_3$)	Δz (Å)
Sr	+2.53	+0.23	+0.06	+0.20
Ti	+7.74	+1.20	+0.49	−0.10
O1	−6.19	−0.96	−0.69	+0.03
O2	−2.04	−0.30	−0.50	−0.01
La	+4.50	+0.91	+0.37	+0.34
Al	+2.90	+0.65	+0.64	−0.06
O1	−2.50	−0.44	−0.32	+0.08
O2	−2.43	−0.48	−0.66	−0.05

Table 7.2: The 3,3 component of the effective charge tensor for $SrTiO_3$ and $LaAlO_3$ in three different structures: bulk, surface, and as a monolayer on a slab of $SrRuO_3$. The last column shows the displacement of atoms after relaxation along the direction perpendicular to the surface.

boundary conditions.

Bilayers

A single monolayer does not break the inversion symmetry at the slab surface enough for a significant polar ground state to form. We thus move towards using bilayers composed of two different oxides in an effort to more strongly break the inversion symmetry at the surface. Our 10 atom unit cell bilayer lacks chemical inversion symmetry and this ensures that the ground state of the overlayer is inherently polar. As seen in this paper [146] investigating $(A_{1/3}A'_{1/3}A''_{1/3})BO_3$ and $A(B_{1/3}B'_{1/3}B''_{1/3})O_3$ structures that the different compositional ordering can lead to "self-poling" in the bulk. In our heterostructures, the reference structure is already polar ensuring a nonzero dipole moment at the surface. We again try to increase the structure's polarization through chemical substitution on the A and B site as well as exploring isovalent and heterovalent substitutions. Since these effects depend strongly on the cell volume [147] we construct the bilayer as follows as shown in Fig. 7.4: each material to be used in the bilayer is first optimized in a bulk cubic phase. A bulk bilayer unit cell is then formed with a single 5 atom unit cell of each perovskite oxide, constrained to match the in-plane lattice parameters of $SrRuO_3$ but allowed to relax along the z-direction while keeping the total (doubled) unit cell volume constant. The bilayer is then placed on 5 unit cells of $SrRuO_3$ to form the final slab structure after which the bilayer is again allowed to relax along the z-direction. When denoting the bilayers, the first one named is that which is adjacent to the $SrRuO_3$ substrate and the second is adjacent to the vacuum layer.

Given the difference in valence charge states one might have expected a larger effect on the surface dipole moment by including $LaAlO_3$, however the more critical variable seems to be ion size mismatch as seen in comparing the tolerance factor to dipole moment in Fig. 7.5.

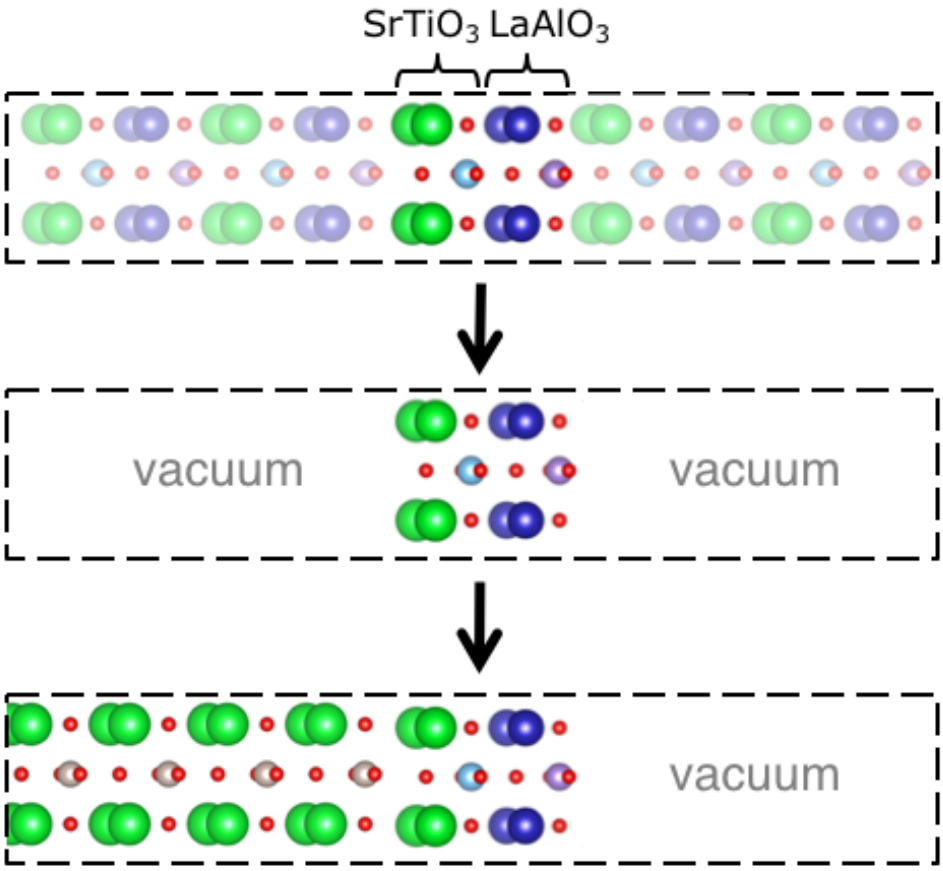

Figure 7.4: The idealized cubic geometry for the bilayers is constructed as shown above. A cubic unit cell is constructed from monolayers of each overlayer material which is relaxed constraining the in-plane lattice parameters to that of $SrRuO_3$. This is then placed on the $SrRuO_3$ slab and allowed to relax again along the z-direction, and the atomic displacements are taken from this last step. For consistency moving forwards, when denoting the bilayer the material listed first is adjacent to $SrRuO_3$ and the second is adjacent to vacuum i.e. this is an $SrTiO_3/LaAlO_3$ bilayer.

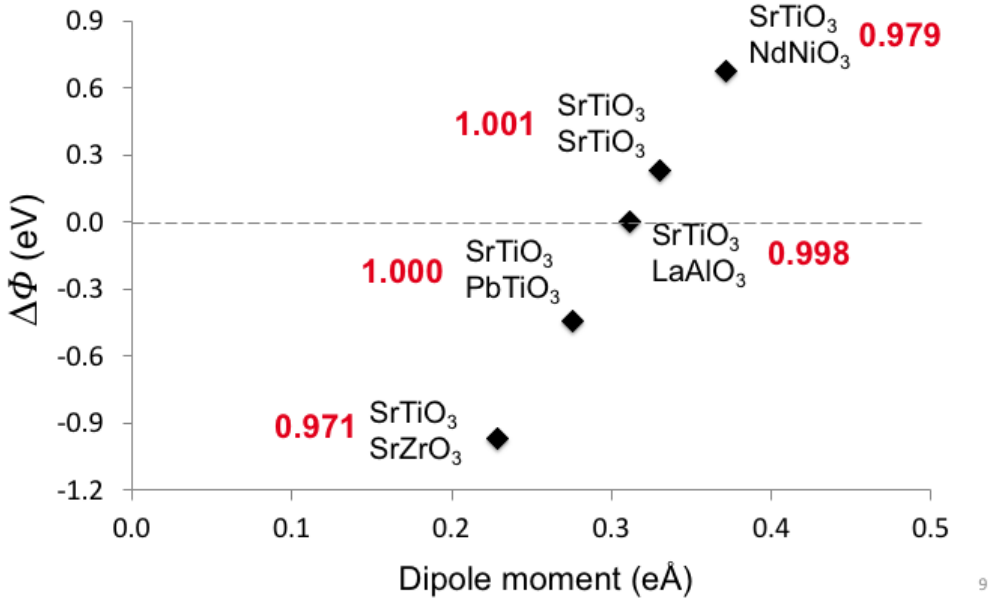

Figure 7.5: Change in bulk $SrRuO_3$ work function with the bilayer compared to the dipole moment of the 10 atom bilayer. The bilayers are also labeled with the tolerance factor (in red) which were calculated for the ideal 10 atom cubic unit cell of the bilayer.

The tolerance factor (defined as $t = \frac{r_A + r_O}{\sqrt{2}(r_B + r_O)}$ for an ABO_3 perovskite), which can be used to determine the degree of distortion in a perovskite structure, is very close to unity for the $LaAlO_3/SrTiO_3$ 10 atom unit cell. We also find the $SrTiO_3/SrTiO_3$ bilayer further shifts the work function close to the bulk $SrTiO_3$ value; as the thickness of the overlayer increases the work function will tend towards the overlayer's bulk Φ value.

Examining several different bilayer configurations, as shown in Fig. 7.5, shows that we are able to achieve changes in work function approaching 1 eV and these are for the bilayers which present the greatest deviation from unity of the tolerance factor. Although all the bilayers have a certain degree of distortion, similar to the monolayers, with large size mismatch and deviations in unity for the tolerance factor, the short range forces associated with local bonding environment overcome the long-range electrostatics driving the polarization to zero.

If we look at two of these cases more closely, we can see the competition between the effective charges and atomic displacements. In the case of the $SrTiO_3/LaAlO_3$ bilayer, the atoms which have large effective charges, La and the oxygen in the TiO_2 layer and AlO_2 layers, negate each other's effects. Meanwhile, Al and Ti have the largest effective charges but have minimal displacements upon relaxation. The net result is a minimal dipole moment and so the work function remains nearly the same as for the $SrRuO_3$ slab alone.

It is interesting to compare the trends with the monolayers in the previous section to the bilayer composed of $SrTiO_3$ and $LaAlO_3$ (see Fig. 7.7). The bilayers are severely dis-

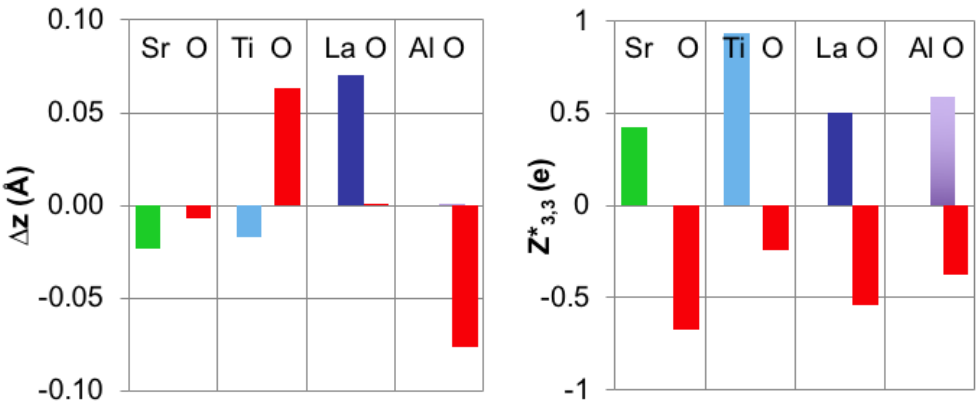

Figure 7.6: The atomic displacements of the $SrTiO_3/LaAlO_3$ bilayer from the ideal cubic unit cell are shown on the left. The atomic layers go from SrO (which is adjacent to the $SrRuO_3$ substrate), TiO_2 (the two oxygens have the same values but only one column is shown here), LaO, and AlO_2 (adjacent to vacuum). The right panel indicates the (3,3) component of the effective charge tensor for each atom in the $SrTiO_3/LaAlO_3$ bilayer.

torted upon relaxation on the substrate and display similar displacement patterns to the individual monolayers. However, the distortions effectively limit the polarization since the positively charged cations displace in opposite directions and the oxygens generally have small displacements. In the situation the oxygen does displace significantly, the magnitude of their respective effective charges are such that they compensate for the positive ion displacements so the sum of the all the ionic contributions, approximated to first order as $P_z \approx \frac{e}{\Omega} \sum_{atoms} Z^*_{3,3} u_3$, effectively limits the net dipole moment. This again results in a small effect on work function where the $SrTiO_3/LaAlO_3$ bilayer yields $\Delta\Phi \approx 0.02$ and comparatively, the inverted bilayer, $LaAlO_3/SrTiO_3$, results in $\Delta\Phi = +0.2$ eV. The larger changes from the inverted bilayer is likely due to the lattice mismatch between $LaAlO_3$ and $SrRuO_3$, being closer to 3% compared to the <1% difference between $SrTiO_3$ and $SrRuO_3$. In having $LaAlO_3$ adjacent to the substrate and constraining the in-plane lattice parameters to match $SrRuO_3$, there is more distortion in the bilayer along the z-direction forming a larger dipole moment than in the $SrTiO_3/LaAlO_3$ bilayer.

However, the $SrTiO_3/SrZrO_3$ bilayer results in a work function decrease of 0.97 eV. Again, while Ti has a large effective charge, its displacement is minimal. However, the ZrO_2 layer features large displacements and large effective charges, and while the displacements are in the same direction, they do not completely negate each other as in the previous case.

This suggests that only looking for atoms with large effective charges is insufficient to finding an overlayer which would change the work function. Rather the atomic displacements, which are influenced by the atomic sizes (and therefore reflected in the tolerance factor) are potentially more important. The ion size mismatch is consistent with the finding that larger

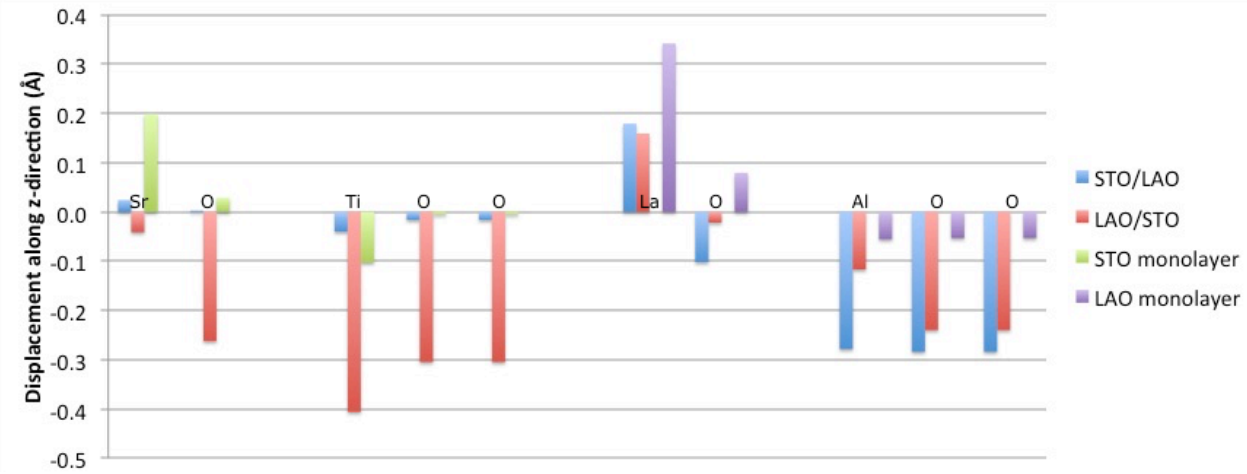

Figure 7.7: Change in the atomic positions along the z-direction upon relaxation on the $SrRuO_3$ substrate.

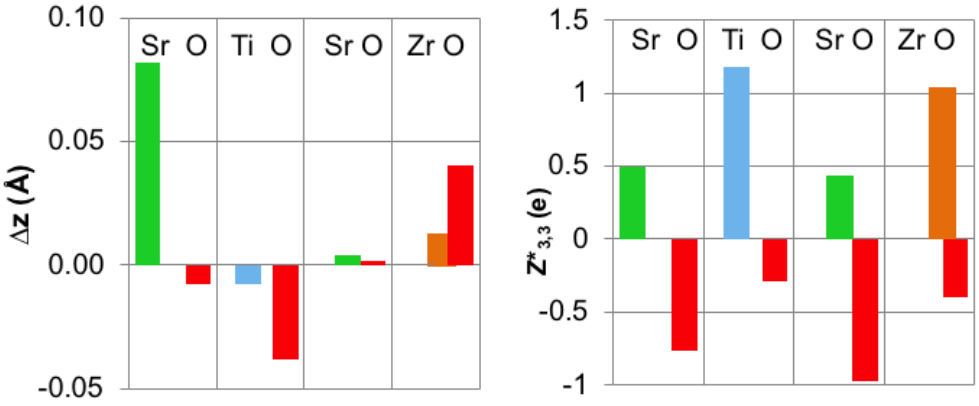

Figure 7.8: The atomic displacements of the $SrTiO_3/SrZrO_3$ bilayer from the ideal cubic unit cell are shown on the left, in analogy to Fig. 7.6. The right panel indicates the (3,3) component of the effective charge tensor for each atom in the $SrTiO_3/SrZrO_3$ bilayer.

deviations from unity of the tolerance factor correspond to larger bilayer dipole moments Fig. 7.5. The atomic sizes of Ni < Ti < Ru < Zr and the trend of decrease in the work function with those overlayers corresponds to those with larger ionic radii. Therefore, one strategy could be to aim for a larger B site cation adjacent to the vacuum so that upon relaxation it will displace into the vacuum in order to accommodate the difference in size, and thereby cause a reduction in the work function.

Furthermore, the ion size mismatch has been suggested as a signifier of non-centrosymmetric metals [148] and hyperferroelectrics [149]. Traditional ferroelectrics are characterized by an unstable TO mode. A new class of materials, originally predicted for the ABC semiconductor family, termed hyperferroelectrics, are predicted to sustain a nonzero polarization under D = 0 boundary conditions whereas any polarization in a traditional ferroelectrics would be negated if the depolarization field is unscreened. This property of the hyperferroelectrics is typified by having an unstable LO mode as well as an unstable TO mode [149]. Recently [150] has proposed a group of Li based perovskite oxides as belonging to this class of hyperferroelectrics; although the $LiBO_3$ materials in [150] are not cubic, it would be interesting to examine the effect of constraining them to the $SrRuO_3$ substrate and other possible non-centrosymmetric metals, also known as "polar metals" (though both are used in the literature, the latter is potentially more confusing since because they are still metallic they don't present a macroscopic polarization in bulk). An unstable LO mode would indicate the system is impervious to $D = 0$ long range fields that act against the polarization and hence such systems are in principle well-suited to this problem.

Chapter 8

High throughput workflow for discovery of ferroelectric and multiferroic materials

"Back in the day of artisanal calculations instead of these mass-produced ones"

October 6, 2017

Multiferroic materials are those which display more than one ferroic ordering at the same time. This can be any combination of ferroelasticity, ferroelectricity, or ferromagnetism (see Figure 8.1. We are particularly interested in those which combine ferroelectricity with magnetism, not only ferromagnetic (aligned spins) but also antiferromagnetic (anti-aligned spins) and ferrimagnetic (anti-aligned spins with unequal magnetic moments) orderings. These materials are actively researched since they have promising application in technological devices. In current nanodevices, the magnetic degree of freedom is used to store information, while the electric degree of freedom is used to transmit information. Having a material which can be used to control both these degrees of freedom not only would lead to miniaturization of such devices, but also towards more energy efficient devices if one can achieve electric field control of magnetic degrees of freedom. When there is an explicit low-order coupling between the electric and magnetic degrees of freedom, then it is a magnetoelectric multiferroic material, which is particularly exciting for the prospect of electric field control of magnetic properties since electric fields require less energy to generate than magnetic fields. While this is an active area of research and there has been much work in designing multiferroic functionality in thin films, heterostructures, and domain walls, there remains a dearth of bulk, single-phase materials that display large electric and magnetic polarizations at room temperature. We took the approach of developing a fully automated workflow to screen material databases for magnetic and ferroelectric properties to try to find new single-phase

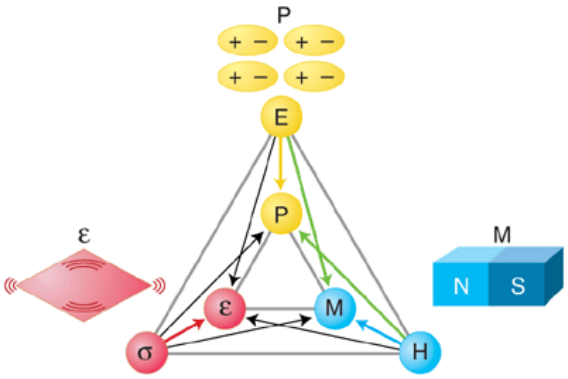

Figure 8.1: Mulitferroic materials are those which simultaneously display more than one ferroic ordering. Ferroelectrics, ferromagnets, and ferroelastics are characterized by having a spontaneous polarization P, magnetization M, or strain ϵ respectively. These in turn are controlled by electric fields E, magnetic fields H, and stress σ. Beyond coexistence, there can also be cross-coupling between these different order parameters, such as in a magnetoelectric multiferroic where the polarization can be controlled by a magnetic field or the magnetization by an electric field. Figure adapted from [151].

multiferroic materials.

The first two sections of this chapter are largely adapted from [11].

8.1 High-throughput calculations

High throughput screening of materials databases is an increasingly popular and powerful approach to search for new materials with desired properties. In order to be efficient, one has to balance performing electronic structure theory calculations which are accurate enough to capture the desired property but also relatively computationally inexpensive such that it is possible to perform the calculations on tens of thousands of materials. Furthermore, automation of these calculations to not only submit, run, and identify errors in the calculations is essential to minimize the time a user needs to spend actively involved in performing the calculations. Automation of the post-processing analysis is also beneficial to this end. High-throughput calculations have been successful for such properties as batteries and thermoelectrics. We are also developing a workflow to screen for multiferroic materials, those which simultaneously exhibit magnetism and ferroelectricity which is further discussed in Chapter 8. Below we outline some of the software tools and general process in developing a high-throughput workflow. A workflow is simply a series of calculations to be performed if certain specified criteria are met.

The Materials Project (MP) database [152] provides structural information on both experimentally known and theoretically proposed materials. The MP API allows one to interac-

tively query the MP database and there are several software tools that have been specifically developed to interface with MP, though are general enough to apply to other databases as well. These are pymatgen [153], which provides analysis of electronic structure theory calculations, fireworks [154], a code which can be used to develop, run, and manage workflows, and atomate [155]. atomate allows one to use a preexisting workflow, and modify it if needed, as well as design one's own workflow. A firework is made up of individual firetasks – such as writing input files, submitting a calculation, moving the output files to a new directory – and each firework should therefore be thought of as one DFT step that one wants to perform. An atomate workflow is then comprised of several fireworks with conditions that have to be met for each successive firework to be executed. One example would be to calculate the band structure of a material, one would have a firework to do a static DFT calculation, another to do a non-self-consistent calculation with the band structure path, and then one could include a post-processing step to create a plot, extract information such as the band gap.

8.2 Ferroelectric workflow overview

High-throughput screening of material databases integrated with first-principles calculations has been increasingly successful in the discovery of new functional materials [156, 157, 158, 159]. A remaining challenge is that while many of the individual components for performing high-throughput searches exist, the infrastructure needed to connect and automate all the necessary components is still under development. The identification of ferroelectrics through symmetry arguments has been an active area of research [160, 161, 162, 163, 164, 165, 166, 167, 168, 169, 170, 171]. Moreover, lists of known ferroelectrics have been previously curated [172, 173, 174, 175, 176, 177, 178]. However, the identification of new ferroelectrics has yet to be automated in a manner readily applicable to emerging materials databases [179, 180, 181, 182, 183, 184, 185]. Automated high-throughput searches for ferroelectric candidates would provide a valuable guide for in-depth computational studies and experimental efforts.

Ferroelectrics have important technological applications, such as in tunable capacitors, non-volatile random access memory devices, and electro-optical data storage. In addition, ferroelectrics are capable of displaying couplings between their electronic degrees of freedom with magnetic or lattice degrees of freedom in multiferroic materials. Ferroelectricity often arises from a structural phase transition between a high-symmetry nonpolar structural phase to a low-symmetry polar structural phase with decreasing temperature, resulting in the emergence of a spontaneous polarization [186, 187, 188]. In this scenario, the atomic geometry of the nonpolar structure can continuously distort such that the new polar structure has a subset of the symmetries of the original structure, satisfying the requirements of a second-order phase transition; in these cases, the polar space group must be an isotropy subgroup of the nonpolar space group, which is a stronger requirement than they only share a simple group-subgroup relation [189, 190, 191].

Thus, certain ferroelectrics can be systematically screened by searching for pairs of nonpolar and polar structures related by a small symmetry-breaking distortion. In the late

1980s, Abrahams performed some of the earliest searches for ferroelectrics in crystallographic databases using symmetry criteria [160, 161]. More recently, automated searches for new ferroelectric candidates have used symmetry arguments to identify nonpolar reference structures for existing polar materials [162, 163, 164]. Other studies have used a combination of group theoretic and first-principles calculations to propose ferroelectric candidates [165, 166, 167]. Bennett and co-workers proposed using high-throughput calculations to perform chemical substitution into structures of known classes of ferroelectrics [168, 169, 170]. Recent work used high-throughput phonon calculations to identify ferroelectrics through polar soft phonon modes of nonpolar phases [171].

In this work, we integrate density functional theory (DFT), crystal structure databases, symmetry tools, workflow software, and a custom analysis toolkit to build a workflow capable of generating libraries of known, previously-proposed and newly-proposed ferroelectrics. This workflow is general and can be used with any crystal structure dataset. This automated workflow has three stages: symmetry analysis, first-principles calculations, and post-processing. Recent work has also developed a separate automated, high-throughput workflow to screen for the magnetic ground state of inorganic materials [192] which includes ferromagnetic, antiferromagnetic, and ferrimagnetic orderings. Through adapting these workflows we can screen the Materials Project database for multiferroics, by first finding those materials which pass our symmetry checks, find their magnetic ground state and compute their polarization from first-principles, and perform further post-processing analysis.

We present the results from performing the ferroelectric workflow on the Materials Project database of inorganic crystal structures [179]. We screened over all the 67 000 materials, the number which were present in the Materials Project database at the time, using symmetry relations between nonpolar and polar structure pairs and calculating the polarization from first-principles calculations. We identify 255 ferroelectric candidates, of which 200 are labeled as "high-quality" by the post-processing analysis. We discuss a few of the candidates which result from this search, in particular $BiInO_3$ and $BiAlO_3$ which have previously been predicted to be ferroelectric, mechanistically similar to $BiFeO_3$, but of which there is little experimental literature on their synthesis. We then outline the ongoing work to integrate the magnetic ground state search. The dataset is open source and the code to perform the workflow has been contributed to the open-source python packages atomate and pymatgen so others can conduct searches of their own and build directly on this work [153, 155].

Prior work developed the first fully automated workflow to search for ferroelectric properties [11]. While representing a major development in screening for these properties and automating calculations of polarization using the Berry phase approach, it still missed several well-known ferroelectric, and also by consequence multiferroic, materials due to some limitations in the approach. While the calculations were spin-polarized, only ferromagnetic ordering was assumed, which is not necessarily the magnetic ground state ordering for many materials and when assigned can lead to metallic band structures for materials which nominally are insulating in their correct magnetic ground state. Furthermore, the effect of U has not been benchmarked and while the calculations are done at the level of PBE+U, the U values used are based on a specific benchmark which may not be the most appropriate to

capture the magnetic ordering.

We start by choosing a crystal structure database on which to perform the search. We emphasize that any crystallographic database (e.g. any of the databases described in [179, 180, 181, 182, 183, 184, 185]) can be used to perform our workflow, as long as the atomic coordinates and lattice parameters of the structures are provided. The automated nature of our ferroelectric search relies on strict symmetry criteria. As described in the Structure Selection section, we pre-screen our candidate nonpolar-polar structure pairs using the symmetry tools in pymatgen and spglib to ensure that these pairs satisfy preliminary group-subgroup relationships. We then use the Structure Relations symmetry tool provided by the Bilbao Crystallographic Server (BCS) [193, 194, 195] to impose the symmetry criteria described in the Workflow Overview, namely, to obtain a transformation matrix connecting the lattice parameters and atomic coordinates of the structure pair [196, 197]. The BCS has a freely available web interface for accessing a wide variety of symmetry tools. We create python scripts to automate interaction with and scrape returned data from the BCS to perform our symmetry checks using the python package mechanize [198]. This symmetry requirement is motivated by Landau theory of second-order phase transitions. One could relax this symmetry criteria, since a ferroelectric switching between its two polar states does not follow such a structural distortion through the high-symmetry phase, (though using the high-symmetry nonpolar structure does facilitate calculation of the polarization from first-principles) and as such one could simply use the polar structure and its enantiomorph in future work.

Within the chosen database, we perform a symmetry analysis to find candidate materials possessing nonpolar-polar structure pairs related by a continuous symmetry deformation. Any such pairs found to satisfy the symmetry deformation criteria are stored in the Distortion Database as being deformable by symmetry. This criteria includes the following conditions: 1) The polar structure belongs to a space group that is a subgroup of the space group of the nonpolar structure; and 2) There exists a transformation matrix between the high-symmetry setting of the nonpolar structure to the low-symmetry setting of the polar structure. The latter imposes that the distortion of the lattice parameters and atomic coordinates between the nonpolar and polar structures is continuous, meaning the polar structure belongs to an isotropy subgroup of the nonpolar structure.

We then carry out DFT calculations on the candidate pairs to extract the changes in the band gaps, total energies, and polarization along the nonpolar-polar distortion. These results are stored in a Workflow Database and then accessed by our Computing Resources to perform the calculations. Next, the information stored in the Distortion, Workflow, and Calculation Databases is used together to post-process quantities such as the computed spontaneous polarization and to validate ferroelectric candidates using experimental and previous first-principles results. The information needed to assess the quality and properties of the candidates is then added to the Candidate Database where it can be accessed by our web interface for viewing the candidate materials in aggregate. Finally, candidates are screened to ensure the polarization and energy profile across the nonpolar-polar distortion are smooth and continuous, meaning that all calculations ended correctly and provide reliable results.

The Materials Project database is largely based on structures from the Inorganic Crystal Structure Database (ICSD) [182, 183] and includes hypothetical structures created through stoichiometric substitution and we use this database for our workflow. Our results for the Materials Project are not intended as the most general curated list of ferroelectrics; however, as an automatically obtained list of ferroelectrics, they uncover new candidates and provide a starting point for further studies. More elaborately curated lists may be constructed by applying our workflow to additional databases in future studies, since it is modular and open-source, for instance using less stringent symmetry requirements or as we describe below to search for multiferroics.

The ferroelectric workflow presents 413 nonpolar-polar structure pairs in the Materials Project database that are compatible with a second-order phase transition as ferroelectric candidates and DFT calculations of total energy, band gap, and polarization were performed for these structures pairs. The dataset generated offers the first opportunity to compare a large number of known, previously proposed, and new ferroelectrics side by side with the same methodology. We believe by setting strict criteria for ferroelectricity and casting a wide-net using high-throughput searches, we will find candidates that challenge and advance our understanding of ferroelectric phenomena. The infrastructure provided by the Bilbao Crystallographic Server, FireWorks, pymatgen, and atomate is crucial to being able to perform these types of searches efficiently.

$BiInO_3$ and $BiAlO_3$

The workflow uses symmetry requirements and first-principles calculations to find candidate materials which are insulating and either have nonmagnetic or ferromagnetic, it does not assume any other magnetic ordering. This workflow resulted in 255 material candidates, of which 126 are not previously reported as ferroelectric. Based on Landau theory of phase transitions, a nonpolar and polar structure pair are identified which can undergo a second order phase transition, and using these structure pairs the DFT total energy difference, polarization, distance of the maximum atomic distortion are reported. The DFT-PBE + U band gap is also reported for the polar structure of the material.

To validate these predictions, information such as the stability of these predicted phases is an important consideration. One can restrict the results to those which had an energy above the convex hull of less than 50 meV and sort the materials based on predicted spontaneous polarization values. Doing so leads to $BiAlO_3$ and $BiInO_3$, which from the workflow is predicted to have a polarization of 80.3 $\mu C/cm^2$ and 64.7 $\mu C/cm^2$ respectively and while previous theory papers have identified as a potential ferroelectric material with a similar mechanism to $BiFeO_3$, there is little information on the synthesis of these materials.

The high-throughput workflow identified two separate polar-nonpolar structure pairs which obeyed the symmetry criteria for a second-order phase transition and passed through the workflow criteria. Both have the $Pna2_1$ as the polar structure, however in one case the nonpolar reference structure is $Pm\bar{3}m$ which has a 0.465 eV energy difference between it and the polar structure and the energy above the convex hull of the $Pm\bar{3}m$ phase is nearly 0.5

eV. The other structure pair involves $Pna2_1$ and an orthorhombic $Pnma$ nonpolar reference structure which is only 40 meV above the convex hull, there is a smaller distortion pathway to the polar structure with only an 11 meV total energy difference. We studied this structure pair for $BiInO_3$ in more detail.

Our density functional theory calculations are similarly calculated to the high-throughput workflow, using PBE [16]. We perform Brillouin zone integrations on a 4×3×4 Γ-centered k-grid and a plane-wave cutoff of 520 eV. However, unlike the workflow, spin-orbit coupling is taken into account self-consistently. Given that $BiInO_3$ contains heavy elements which would likely have strong spin-orbit coupling effects, we recalculated the energy per atom across the distortion pathway, again simply done by linearly interpolating the atomic positions between the polar and nonpolar structures in eight steps.

The polarization is computed from first-principles by linearly interpolating the atomic positions between the nonpolar and polar structure. Eight interpolations are performed from which the polarization branch is reconstructed and the energy per atom is also reported along the distortion pathway, which for a typical ferroelectric would form a double well potential where the nonpolar phase is higher in energy than the polar structures. In this case, there is a large energy barrier along this distortion pathway suggestive of an antiferroelectric transition, but the size of the barrier is approximately 160 meV suggesting this is energetically difficult to switch. Upon recalculating this energy barrier including spin-orbit coupling, we find that it remains close to 160 meV, consistent with the observation by experiment that even upon large electric field application the nonpolar structure cannot be switched to the polar structure; the band gap of the polar structure is slightly reduced to 2.52 eV. $BiAlO_3$ does not have this energy barrier and indeed its energy profile is more indicative of a typical ferroelectric, but we cannot ascertain from these calculations why the experimental synthesis is difficult to achieve.

This suggests that while the results from the workflow are promising, careful scrutiny should be paid to the energy profile along the distortion pathway from the nonpolar to polar structure, since large energy barriers are prohibitive to practical switching. Furthermore, while the workflow identifies candidates, further calculations should be done to validate the materials which include heavy elements since the energy barrier and band gap can change upon inclusion of spin-orbit coupling. While not relevant for $BiInO_3$ or $BiAlO_3$, materials which are suspected to have other magnetic orderings should also be further validated by checking whether an antiferromagnetic ordering is energetically preferred to ferromagnetic, since this is not checked in the workflow [11].

8.3 Including search for other magnetic orderings

As previously mentioned, recent work [192] developed an automated high-throughput workflow to screen materials for their magnetic ground state. This is a complicated process, since the unit cell to accommodate the magnetic ordering can be larger than the primitive unit cell of the material. As such, at a very high-level overview, it first identifies the atoms in

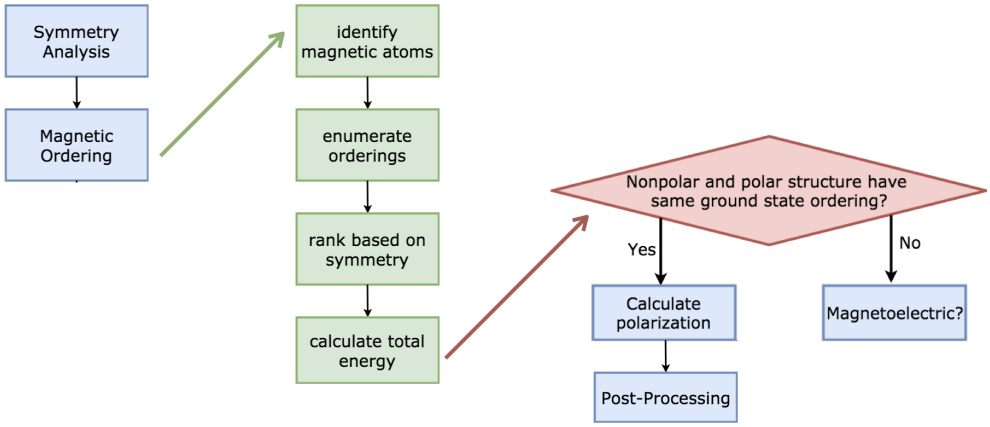

Figure 8.2: A high-level overview of the strategy to screen for multiferroics.

a material that are likely to be magnetic, based on presets from the Materials Project. Labeling those atoms separately, it enumerates different collinear magnetic orderings, always including FM ordering, and then enumerates different AFM orderings within the original unit cell, then creates increasingly larger supercells which can accommodate other AFM orderings (see details in [192]). These possible orderings are ranked from most symmetric to least symmetric and structural relaxations followed by static calculations are performed on the eight most symmetric orderings using DFT–PBE + U. The magnetic ordering which yields the lowest total energy is taken to be the ground state ordering. The Hubbard U values are not tuned, and are only taken from the Materials Project default settings, and it is known that this can have a large influence on the ordering. As well, some well-known Type-II multiferroics have noncollinear magnetic orderings which would not be captured by this workflow since we are restricted to collinear orderings. As such, while this workflow should not be taken to definitively determine the magnetic ground state, it does correctly identify if an AFM ordering is preferred over FM correctly in over 95% of the benchmark set (comprised of 64 materials with experimentally known, collinear magnetic orderings from the MAGNDATA dataset [199], mostly involving d electrons but also materials with Gd and Eu are included) and correctly identifies the experimentally verified magnetic ordering in over 60% of cases. As such, this is sufficient for our purposes to identify materials which do have a magnetic ordering and would continue through the remainder of the ferroelectric workflow.

One potential issue is in a case where the polar and nonpolar materials are predicted to have different magnetic orderings. One option could be to interpolate the magnetic moments as well as the structures in the distortion pathway when computing the polarization. However, it is not necessarily true that in a physical system when a ferroelectric material is switched, the material actually goes through this high-symmetry nonpolar structure and rather it is a construct used to calculate the polarization from first-principles and follows from

a Landau argument for a second-order phase transition. As such, it is not really physical to assume the magnetic moments would similarly undergo such an artificial transition as well. Therefore, instead materials that fall into this case would be flagged as a possible magnetoelectric – since the different magnetic orderings for different symmetries suggest a possible coupling between the ferroelectric and magnetic degrees of freedom – and the polar structure's magnetic ordering will be applied to all interpolated structures when computing the polarization. As with all the results from these high-throughput workflows, we aim to perform accurate enough calculations to capture if the desired property is likely to occur in a material, but expect to need to perform more rigorous calculations on the final candidates.

Another consideration is ensuring the polar and nonpolar structures are the same sized unit cell after determining the magnetic ground state. The magnetic ordering may require a supercell of the original unit cell of the polar or nonpolar structure. However, to perform the interpolation we match the atomic positions of the polar and nonpolar structure and linearly interpolate between them. If, for instance, the polar structure requires a larger supercell to accommodate the magnetic ordering, we must first determine the transformation matrix used to generate the supercell and apply it to the nonpolar structure before continuing with the interpolation procedure.

Chapter 9

Conclusions

"I feel basically I'm too tired to say anything"

October 19, 2018

In this dissertation, we have used advanced electronic structure methods to study materials away from their bulk ground states. Pressure, strain at interfaces, and chemical substitutions can all be used to manipulate materials to exhibit properties different from those present under ambient conditions. While pressure was previously known to yield surprisingly complex structures for elemental lithium, we find that it also leads to topologically nontrivial behavior above 80 GPa, suggesting that pressure can be used to achieve interesting topological features in other light elemental solids. A structurally diverse set of halide perovskite materials were studied. Dilute alloying with Sn was shown to successfully reduce the band gap of $Cs_2AgBiBr_6$ demonstrating that heterovalent alloying can further expand the compositional diversity in these systems; halide substitution affects the structure of $(EA)_2CuBr_4$ and helps enable an enormous change in conductivity with applied pressure; and chemical and structural changes in $Cs_8Au_4InCl_{23}$ also strongly affect its optoelectronic properties. Similarly, perovskite oxides are a diverse materials class and atomically thin layers can tune the work function of a $SrRuO_3$ substrate by almost 1 eV; coupling to a ferroelectric structural order parameter could further enhance the variation in work function. Lastly we explore how high throughput computation can be used to discover new materials with desirable properties through carefully chosen symmetry and first-principles based criteria. The wide variety of materials studied, from elemental solids to doping with heavy elements in a quaternary system, displays the generality and flexibility of the Kohn-Sham DFT formalism to predict novel, experimentally relevant properties of real and complex materials.

Bibliography

[1] R. M. Martin. *Electronic structure: Basic Theory and Practical Methods*. Cambridge University Press, 2004.

[2] Chris J. Pickard and R. J. Needs. "Dense Low-Coordination Phases of Lithium". In: *Phys. Rev. Lett.* 102 (14 Apr. 2009), p. 146401. DOI: 10.1103/PhysRevLett.102.146401. URL: https://link.aps.org/doi/10.1103/PhysRevLett.102.146401.

[3] Jian Lv et al. "Predicted novel high-pressure phases of lithium". In: *Phys. Rev. Lett.* 106.1 (2011), p. 015503.

[4] Matthew D. Smith, Bridget A. Connor, and Hemamala I. Karunadasa. "Tuning the Luminescence of Layered Halide Perovskites". In: *Chemical Reviews* 119.5 (2019). PMID: 30689364, pp. 3104–3139. DOI: 10.1021/acs.chemrev.8b00477. URL: https://doi.org/10.1021/acs.chemrev.8b00477.

[5] A. H. Slavney et al. "A Bismuth-Halide Double Perovskite with Long Carrier Recombination Lifetime for Photovoltaic Applications". In: *J. Am. Chem. Soc.* 138.7 (2016), pp. 2138–41. ISSN: 1520-5126 (Electronic) 0002-7863 (Linking). DOI: 10.1021/jacs.5b13294. URL: https://www.ncbi.nlm.nih.gov/pubmed/26853379.

[6] Eric T. McClure et al. "Cs2AgBiX6(X = Br, Cl): New Visible Light Absorbing, Lead-Free Halide Perovskite Semiconductors". In: *Chem. Mater.* 28.5 (2016), pp. 1348–1354. ISSN: 0897-4756 1520-5002. DOI: 10.1021/acs.chemmater.5b04231. URL: http://dx.doi.org/10.1021/acs.chemmater.5b04231%20files/72/acs.chemmater.html%20files/468/acs.chemmater.html%20http://pubs.acs.org/doi/pdfplus/10.1021/acs.chemmater.5b04231.

[7] G. Volonakis et al. "Lead-Free Halide Double Perovskites via Heterovalent Substitution of Noble Metals". In: *J. Phys. Chem. Lett.* 7.7 (2016), pp. 1254–9. ISSN: 1948-7185 (Electronic) 1948-7185 (Linking). DOI: 10.1021/acs.jpclett.6b00376. URL: https://www.ncbi.nlm.nih.gov/pubmed/26982118.

[8] A. H. Slavney et al. "Defect-Induced Band-Edge Reconstruction of a Bismuth-Halide Double Perovskite for Visible-Light Absorption". In: *J. Am. Chem. Soc.* 139.14 (2017), pp. 5015–5018. ISSN: 1520-5126 (Electronic) 0002-7863 (Linking). DOI: 10.1021/jacs.7b01629. URL: https://www.ncbi.nlm.nih.gov/pubmed/28353345.

[9] Kurt P. Lindquist et al. "Tuning the bandgap of Cs2AgBiBr6 through dilute tin alloying". In: *Chem. Sci.* (2019). DOI: 10.1039/C9SC02581B. URL: http://dx.doi.org/10.1039/C9SC02581B.

[10] Robert Palgrave. *Perovskite Alignment Chart*. https://twitter.com/Robert_Palgrave/status/1095366599698194433. Accessed: 2019-12-06. 2019.

[11] T.E. Smidt et al. "An automatically curated first-principles database of ferroelectrics". In: *under review* (2019).

[12] P. Hohenberg and W. Kohn. "Inhomogeneous Electron Gas". In: *Phys. Rev.* 136 (1964), B864–B871.

[13] W. Kohn and L. J. Sham. "Self-Consistent Equations Including Exchange and Correlation Effects". In: *Phys. Rev.* 140 (1965), A1133–A1138.

[14] Marvin L. Cohen and Steven G. Louie. *Fundamentals of Condensed Matter Physics*. Cambridge University Press, 2016. DOI: 10.1017/CBO9781139031783.

[15] John P. Perdew. "Density-functional approximation for the correlation energy of the inhomogeneous electron gas". In: *Phys. Rev. B* 33 (12 June 1986), pp. 8822–8824. DOI: 10.1103/PhysRevB.33.8822. URL: https://link.aps.org/doi/10.1103/PhysRevB.33.8822.

[16] J. P. Perdew, K. Burke, and M. Ernzerhof. "Generalized Gradient Approximation Made Simple." In: *Physical review letters* 77.18 (Oct. 1996), pp. 3865–3868. ISSN: 1079-7114. URL: http://www.ncbi.nlm.nih.gov/pubmed/10062328.

[17] Jochen Heyd, Gustavo E Scuseria, and Matthias Ernzerhof. "Hybrid functionals based on a screened Coulomb potential". In: *The Journal of Chemical Physics* 118.18 (2003), pp. 8207–8215.

[18] Felix Bloch. "Über die Quantenmechanik der Elektronen in Kristallgittern". In: *Zeitschrift fur Physik* 52.7-8 (July 1929), pp. 555–600. DOI: 10.1007/BF01339455.

[19] G. H. Wannier. "The Structure of Electronic Excitation Levels in Insulating Crystals". In: *Phys. Rev.* 52 (1937), pp. 191–197.

[20] Nicola Marzari and David Vanderbilt. "Maximally localized generalized Wannier functions for composite energy bands". In: *Phys. Rev. B* 56 (20 Nov. 1997), pp. 12847–12865. DOI: 10.1103/PhysRevB.56.12847. URL: https://link.aps.org/doi/10.1103/PhysRevB.56.12847.

[21] AA Mostofi et al. "An updated version of wannier90: A tool for obtaining maximally-localised Wannier functions". In: *Comput. Phys. Commun.* 185 (2014), pp. 2309–2310. DOI: 10.1016/j.cpc.2014.05.003. URL: http://dx.doi.org/10.1016/j.cpc.2014.05.003.

[22] Liang Fu and Charles L Kane. "Topological insulators with inversion symmetry". In: *Phys. Rev. B* 76.4 (2007), p. 045302.

[23] R. Resta. "Theory of the electric polarization in crystals". In: *Ferroelectrics* 136.1 (Nov. 1992), pp. 51–55. DOI: 10.1080/00150199208016065. URL: https://doi.org/10.1080/00150199208016065.

[24] R. D. King-Smith and David Vanderbilt. "Theory of polarization of crystalline solids". In: *Phys. Rev. B* 47 (1993), R1651–R1654.

[25] David Vanderbilt and R. D. King-Smith. "Electric polarization as a bulk quantity and its relation to surface charge". In: *Physical Review B* 48.7 (Aug. 1993), pp. 4442–4455. DOI: 10.1103/physrevb.48.4442. URL: https://doi.org/10.1103/physrevb.48.4442.

[26] Raffaele Resta. "Macroscopic polarization in crystalline dielectrics: the geometric phase approach". In: *Reviews of Modern Physics* 66.3 (July 1994), pp. 899–915. DOI: 10.1103/revmodphys.66.899. URL: https://doi.org/10.1103/revmodphys.66.899.

[27] K. M. Rabe and U. V. Waghmare. "First-principles model hamiltonians for ferroelectric phase transitions". In: *Ferroelectrics* 136.1 (1992), pp. 147–156. DOI: 10.1080/00150199208016074. eprint: https://doi.org/10.1080/00150199208016074. URL: https://doi.org/10.1080/00150199208016074.

[28] Raffaele Resta and David Vanderbilt. "Theory of Polarization: A Modern Approach". In: *Physics of Ferroelectrics: A Modern Perspective*. Berlin, Heidelberg: Springer Berlin Heidelberg, 2007, pp. 31–68. ISBN: 978-3-540-34591-6. DOI: 10.1007/978-3-540-34591-6_2. URL: http://dx.doi.org/10.1007/978-3-540-34591-6_2.

[29] Nicola A Spaldin. "A beginner's guide to the modern theory of polarization". In: *Journal of Solid State Chemistry* 195 (2012), pp. 2–10. DOI: 10.1016/j.jssc.2012.05.010.

[30] R. Resta and D. Vanderbilt. "Theory of Polarization: A Modern Approach". In: *Topics Appl. Physics* 105 (2007), pp. 31–68.

[31] Alexey A Soluyanov and David Vanderbilt. "Computing topological invariants without inversion symmetry". In: *PRB* 83.23 (2011), p. 235401.

[32] Dominik Gresch et al. "Z2Pack: Numerical implementation of hybrid Wannier centers for identifying topological materials". In: *Phys. Rev. B* 95 (7 Feb. 2017), p. 075146. DOI: 10.1103/PhysRevB.95.075146. URL: https://link.aps.org/doi/10.1103/PhysRevB.95.075146.

[33] Stephanie A. Mack, Sinead M. Griffin, and Jeffrey B. Neaton. "Emergence of topological electronic phases in elemental lithium under pressure". In: *Proceedings of the National Academy of Sciences* 116.19 (2019), pp. 9197–9201. ISSN: 0027-8424. DOI: 10.1073/pnas.1821533116. eprint: https://www.pnas.org/content/116/19/9197.full.pdf. URL: https://www.pnas.org/content/116/19/9197.

[34] J.B. Neaton and N.W. Ashcroft. "Pairing in dense lithium". In: *Nature* 400.6740 (1999), pp. 141–144.

[35] J. B. Neaton and N. W. Ashcroft. "On the Constitution of Sodium at Higher Densities". In: *Phys. Rev. Lett.* 86 (13 Mar. 2001), pp. 2830–2833. DOI: 10.1103/PhysRevLett.86.2830. URL: https://link.aps.org/doi/10.1103/PhysRevLett.86.2830.

[36] J. C. Boettger and S. B. Trickey. "Equation of state and properties of lithium". In: *Phys. Rev. B* 32 (6 Sept. 1985), pp. 3391–3398. DOI: 10.1103/PhysRevB.32.3391. URL: https://link.aps.org/doi/10.1103/PhysRevB.32.3391.

[37] Bruno Rousseau and N. W. Ashcroft. "Interstitial Electronic Localization". In: *Phys. Rev. Lett.* 101 (4 July 2008), p. 046407. DOI: 10.1103/PhysRevLett.101.046407. URL: https://link.aps.org/doi/10.1103/PhysRevLett.101.046407.

[38] Philip Richard Wallace. "The band theory of graphite". In: *Physical Review* 71.9 (1947), p. 622.

[39] AH Castro Neto et al. "The electronic properties of graphene". In: *Rev. Mod. Phys.* 81.1 (2009), p. 109.

[40] Michael Hanfland et al. "New High-Pressure Phases of Lithium". In: *Nature* 408 (Dec. 2000), pp. 174–8.

[41] BQ Lv et al. "Observation of Weyl nodes in TaAs". In: *Nature Physics* 11 (2015), pp. 724–727.

[42] Christophe L Guillaume et al. "Cold melting and solid structures of dense lithium". In: *Nat. Phys.* 7.3 (2011), pp. 211–214.

[43] G. Kresse and J. Hafner. "Ab initio molecular dynamics for liquid metals". In: *Phys. Rev. B* 47 (1993), pp. 558–561.

[44] G. Kresse and J. Furthmüller. "Efficient iterative schemes for ab initio total-energy calculations using a plane-wave basis set". In: *Phys. Rev. B* 54.16 (Oct. 1996), pp. 11169–11186.

[45] QuanSheng Wu et al. "WannierTools: An open-source software package for novel topological materials". In: *Computer Physics Communications* 224 (2018), pp. 405–416. ISSN: 0010-4655. DOI: https://doi.org/10.1016/j.cpc.2017.09.033. URL: http://www.sciencedirect.com/science/article/pii/S0010465517303442.

[46] M. Z. Hasan and C. L. Kane. "*Colloquium* : Topological insulators". In: *Rev. Mod. Phys.* 82 (4 Nov. 2010), pp. 3045–3067. DOI: 10.1103/RevModPhys.82.3045. URL: http://link.aps.org/doi/10.1103/RevModPhys.82.3045.

[47] Xiangang Wan et al. "Topological semimetal and Fermi-arc surface states in the electronic structure of pyrochlore iridates". In: *Phys. Rev. B* 83.20 (2011), p. 205101.

[48] Steve M Young et al. "Dirac semimetal in three dimensions". In: *Phys. Rev. Lett.* 108.14 (2012), p. 140405.

[49] Alexey A Soluyanov et al. "Type-II Weyl semimetals". In: *Nature* 527.7579 (2015), pp. 495–498.

[50] Youngkuk Kim et al. "Dirac line nodes in inversion-symmetric crystals". In: *Phys. Rev. Lett.* 115.3 (2015), p. 036806.

[51] Hongming Weng, Xi Dai, and Zhong Fang. "Topological semimetals predicted from first-principles calculations". In: *J. Phys. Condens. Matter* 28.30 (2016), p. 303001.

[52] Motoaki Hirayama et al. "Topological Dirac nodal lines and surface charges in fcc alkaline earth metals". In: *Nat. Commun.* 8 (2017), p. 14022.

[53] Ronghan Li et al. "Dirac node lines in pure alkali earth metals". In: *Phys. Rev. Lett.* 117.9 (2016), p. 096401.

[54] Ivan I Naumov, Ronald E Cohen, and Russell J Hemley. "Graphene physics and insulator-metal transition in compressed hydrogen". In: *Phys. Rev. B* 88.4 (2013), p. 045125.

[55] Ivan I Naumov and Russell J Hemley. "Topological surface states in dense solid hydrogen". In: *Phys. Rev. Lett.* 117.20 (2016), p. 206403.

[56] Frederick Seitz. "The Theoretical Constitution of Metallic Lithium". In: *Phys. Rev.* 47 (5 Mar. 1935), pp. 400–412. DOI: 10.1103/PhysRev.47.400. URL: https://link.aps.org/doi/10.1103/PhysRev.47.400.

[57] Steve M Young and Charles L Kane. "Dirac semimetals in two dimensions". In: *Phys. Rev. Lett.* 115.12 (2015), p. 126803.

[58] Benjamin J Wieder et al. "Double Dirac semimetals in three dimensions". In: *Phys. Rev. Lett.* 116.18 (2016), p. 186402.

[59] ZK Liu et al. "Discovery of a three-dimensional topological Dirac semimetal, Na_3Bi". In: *Science* 343.6173 (2014), pp. 864–867.

[60] Madhab Neupane et al. "Observation of a three-dimensional topological Dirac semimetal phase in high-mobility Cd3As2". In: *Nat. Commun.* 5 (2014), p. 3786.

[61] A. A. Burkov, M. D. Hook, and Leon Balents. "Topological nodal semimetals". In: *Phys. Rev. B* 84 (23 Dec. 2011), p. 235126. DOI: 10.1103/PhysRevB.84.235126. URL: https://link.aps.org/doi/10.1103/PhysRevB.84.235126.

[62] W. B. Rui, Y. X. Zhao, and Andreas P. Schnyder. "Topological transport in Dirac nodal-line semimetals". In: *Phys. Rev. B* 97 (16 Apr. 2018), p. 161113. DOI: 10.1103/PhysRevB.97.161113. URL: https://link.aps.org/doi/10.1103/PhysRevB.97.161113.

[63] J. C. Boettger and R. C. Albers. "Structural phase stability in lithium to ultra-high pressures". In: *Phys. Rev. B* 39 (5 Feb. 1989), pp. 3010–3014. DOI: 10.1103/PhysRevB.39.3010. URL: https://link.aps.org/doi/10.1103/PhysRevB.39.3010.

[64] I.M. Lifshitz. "Anomalies of Electron Characteristics of a Metal in the High Pressure Region". In: *Sov. Phys. JETP* 11.5 (1960), p. 1130.

[65] G. E. Volovik. "Topological Lifshitz transitions". In: *Low Temperature Physics* 43.1 (2017), pp. 47–55. DOI: 10.1063/1.4974185.

[66] A.Vl. Andrianov. "Electronic topological transition of the Lifshitz type and complex magnetic structures in heavy rare-earth metals". In: *Low Temp. Phys.* 40.4 (2014), pp. 323–327. DOI: 10.1063/1.4871743. eprint: https://doi.org/10.1063/1.4871743. URL: https://doi.org/10.1063/1.4871743.

[67] P. Di Pietro et al. "Emergent Dirac carriers across a pressure-induced Lifshitz transition in black phosphorus". In: *Phys. Rev. B* 98 (16 Oct. 2018), p. 165111. DOI: 10.1103/PhysRevB.98.165111. URL: https://link.aps.org/doi/10.1103/PhysRevB.98.165111.

[68] Weiwei Sun et al. "Anisotropic distortion and Lifshitz transition in α-Hf under pressure". In: *Phys. Rev. B* 95 (11 Mar. 2017), p. 115130. DOI: 10.1103/PhysRevB.95.115130. URL: https://link.aps.org/doi/10.1103/PhysRevB.95.115130.

[69] Y. P. Gaidukov, N. P. Danilova, and M. B. Shcherbina-Samoilova. "Electronic transition of order 2 $\frac{1}{2}$ in bismuth following simple dilatation". In: *Sov. Phys. JETP* 50 (Nov. 1979), p. 1018.

[70] N.B. Brandt et al. "Anomalies of thermoelectric power and of resistance in eletronic topological transitions in bismuth and its alloys". In: *Sov. Phys. JETP* 06 (June 1985), p. 1303.

[71] D. R. Overcash et al. "Stress-Induced Electronic Transition (2.5 Order) in Al". In: *Phys. Rev. Lett.* 46 (4 Jan. 1981), pp. 287–290. DOI: 10.1103/PhysRevLett.46.287. URL: https://link.aps.org/doi/10.1103/PhysRevLett.46.287.

[72] Yu P Gaidukov, NP Danilova, and MB Shcherbina-Samoilova. "Phase transition of order 2 $\frac{1}{2}$ in zinc". In: *JETP Lett* 25 (1977), p. 479. URL: http://www.jetpletters.ac.ru/ps/1415/article_21473.pdf.

[73] SL Bud'ko et al. "The Fermi surface of cadmium at an electron-topological phase transition under pressure". In: *Sov. Phys. JETP* 59.2 (1984), pp. 454–457.

[74] Charles Lee Watlington, JW Cook Jr, and MJ Skove. "Effect of large uniaxial stress on the superconducting transition temperature of zinc and cadmium". In: *Phys. Rev. B* 15.3 (1977), p. 1370.

[75] J. E. Schirber and J. P. Van Dyke. "Pressure-Induced "Electron Transition" in As". In: *Phys. Rev. Lett.* 26 (5 Feb. 1971), pp. 246–249. DOI: 10.1103/PhysRevLett.26.246. URL: https://link.aps.org/doi/10.1103/PhysRevLett.26.246.

[76] I.Ya. Volynskii, V.I. Makaraov, and V.V. Gann. "Effect of impurity and pressure on the topology of the Fermi surface of indium". In: *Sov. Phys. JETP* 42.3 (1975), p. 518.

[77] C. W. Chu, T. F. Smith, and W. E. Gardner. "Study of Fermi-Surface Topology Changes in Rhenium and Dilute Re Solid Solutions from T_c Measurements at High Pressure". In: *Phys. Rev. B* 1 (1 Jan. 1970), pp. 214–221. DOI: 10.1103/PhysRevB.1.214. URL: https://link.aps.org/doi/10.1103/PhysRevB.1.214.

[78] W.G. Zittel et al. "Band-reordering effects in the ultra-high-pressure equation of state of lithium". In: *J. Phys. F: Met. Phys.* 15 (L247 1985).

[79] Bing Li et al. "Diamond anvil cell behavior up to 4 Mbar". In: *Proceedings of the National Academy of Sciences* 115.8 (2018), pp. 1713–1717. ISSN: 0027-8424. DOI: 10.1073/pnas.1721425115. eprint: https://www.pnas.org/content/115/8/1713.full.pdf. URL: https://www.pnas.org/content/115/8/1713.

[80] Jeffrey M. McMahon et al. "The properties of hydrogen and helium under extreme conditions". In: *Rev. Mod. Phys.* 84 (4 Nov. 2012), pp. 1607–1653. DOI: 10.1103/RevModPhys.84.1607. URL: https://link.aps.org/doi/10.1103/RevModPhys.84.1607.

[81] Ranga P. Dias and Isaac F. Silvera. "Observation of the Wigner-Huntington transition to metallic hydrogen". In: *Science* 355.6326 (2017), pp. 715–718. ISSN: 0036-8075. DOI: 10.1126/science.aal1579. eprint: http://science.sciencemag.org/content/355/6326/715.full.pdf. URL: http://science.sciencemag.org/content/355/6326/715.

[82] Hua Y. Geng. "Public debate on metallic hydrogen to boost high pressure research". In: *Matter and Radiation at Extremes* 2.6 (2017), pp. 275–277. ISSN: 2468-080X. DOI: https://doi.org/10.1016/j.mre.2017.10.001. URL: http://www.sciencedirect.com/science/article/pii/S2468080X1730105X.

[83] Shanti Deemyad and Rong Zhang. "Probing quantum effects in lithium". In: *Physica C: Superconductivity and its Applications* 548 (2018), pp. 68–71. ISSN: 0921-4534. DOI: https://doi.org/10.1016/j.physc.2018.02.007. URL: http://www.sciencedirect.com/science/article/pii/S0921453417302320.

[84] Graeme J. Ackland et al. "Quantum and isotope effects in lithium metal". In: *Science* 356.6344 (2017), pp. 1254–1259. ISSN: 0036-8075. DOI: 10.1126/science.aal4886. eprint: http://science.sciencemag.org/content/356/6344/1254.full.pdf. URL: http://science.sciencemag.org/content/356/6344/1254.

[85] Sabri F. Elatresh et al. "Evidence from Fermi surface analysis for the low-temperature structure of lithium". In: *Proceedings of the National Academy of Sciences* 114.21 (2017), pp. 5389–5394. ISSN: 0027-8424. DOI: 10.1073/pnas.1701994114. eprint: https://www.pnas.org/content/114/21/5389.full.pdf. URL: https://www.pnas.org/content/114/21/5389.

[86] Bartomeu Monserrat et al. "Structure and Metallicity of Phase V of Hydrogen". In: *Phys. Rev. Lett.* 120 (25 June 2018), p. 255701. DOI: 10.1103/PhysRevLett.120.255701. URL: https://link.aps.org/doi/10.1103/PhysRevLett.120.255701.

[87] Cheol-Hwan Park et al. "Velocity Renormalization and Carrier Lifetime in Graphene from the Electron-Phonon Interaction". In: *Phys. Rev. Lett.* 99 (8 Aug. 2007), p. 086804. DOI: 10.1103/PhysRevLett.99.086804. URL: https://link.aps.org/doi/10.1103/PhysRevLett.99.086804.

[88] Aaron Bostwick et al. "Quasiparticle Dynamics in Graphene". In: *Nature Physics* 3 (Jan. 2007), pp. 36–40. DOI: 10.1038/nphys477.

[89] Akihiro Kojima et al. "Organometal Halide Perovskites as Visible-Light Sensitizers for Photovoltaic Cells". In: *J. Am. Chem. Soc.* 131.17 (2009), pp. 6050–6051. ISSN: 0002-7863. DOI: 10.1021/ja809598r. URL: https://doi.org/10.1021/ja809598r.

[90] Martin A. Green, Anita Ho-Baillie, and Henry J. Snaith. "The Emergence of Perovskite Solar Cells". In: *Nat. Photonics* 8 (2014), pp. 506–514. DOI: 10.1038/nphoton.2014.134. URL: http://dx.doi.org/10.1038/nphoton.2014.134%20https://www.nature.com/articles/nphoton.2014.134.pdf.

[91] Aslihan Babayigit et al. "Toxicity of Organometal Halide Perovskite Solar Cells". In: *Nat. Mater.* 15 (2016), pp. 247–251. DOI: 10.1038/nmat4572. URL: http://dx.doi.org/10.1038/nmat4572%20http://www.nature.com/articles/nmat4572.pdf.

[92] Adam H. Slavney et al. "Chemical Approaches to Addressing the Instability and Toxicity of Lead Halide Perovskite Absorbers". In: *Inorg. Chem.* 56.1 (2017), pp. 46–55. ISSN: 0020-1669. DOI: 10.1021/acs.inorgchem.6b01336. URL: https://doi.org/10.1021/acs.inorgchem.6b01336%20https://pubs.acs.org/doi/pdfplus/10.1021/acs.inorgchem.6b01336.

[93] John D. Donaldson et al. "Effects of the Presence of Valence-Shell Non-Bonding Electron Pairs on the Properties and Structures of Caesium Tin(II) Bromides and of Related Antimony and Tellurium Compounds". In: *Dalton Trans.* 15 (1975), pp. 1500–1506. ISSN: 0300-9246. URL: http://dx.doi.org/10.1039/DT9750001500%20http://pubs.rsc.org/en/content/articlepdf/1975/dt/dt9750001500.

[94] J. A. A. Ketelaar, A. A. Rietdijk, and C. H. van Staveren. "Die Kristallstruktur von Ammonium, Kalium, Rubidium und Cäsiumstannibromid". In: *Recl. Trav. Chim. Pays-Bas* 56.9 (1937), pp. 907–908. DOI: doi:10.1002/recl.19370560913. URL: https://onlinelibrary.wiley.com/doi/abs/10.1002/recl.19370560913%20https://onlinelibrary.wiley.com/doi/pdf/10.1002/recl.19370560913.

[95] A. Spinelli et al. "Electronic transport in doped $SrTiO_3$: Conduction mechanisms and potential applications". In: *Phys. Rev. B* 81.15 (2010), p. 155110. DOI: 10.1103/PhysRevB.81.155110. URL: https://link.aps.org/doi/10.1103/PhysRevB.81.155110%20https://journals.aps.org/prb/pdf/10.1103/PhysRevB.81.155110.

[96] Kuan Zong Fung, Jong Chen, and Anil V. Virkar. "Effect of Aliovalent Dopants on the Kinetics of Phase Transformation and Ordering in RE2O3 – Bi2O3 (RE = Yb, Er, Y, or Dy) Solid Solutions". In: *J. Am. Ceram. Soc.* 76.10 (1993), pp. 2403–2418. DOI: doi:10.1111/j.1151-2916.1993.tb03961.x. URL: https://onlinelibrary.wiley.com/doi/abs/10.1111/j.1151-2916.1993.tb03961.x%20https://onlinelibrary.wiley.com/doi/pdf/10.1111/j.1151-2916.1993.tb03961.x.

[97] Miroslaw Maczka et al. "Effect of Aliovalent Doping on the Properties of Perovskite-Like Multiferroic Formates". In: *J. Mater. Chem. C* 3.36 (2015), pp. 9337–9345. ISSN: 2050-7526. DOI: 10.1039/C5TC02295A. URL: http://dx.doi.org/10.1039/C5TC02295A%20http://pubs.rsc.org/en/content/articlepdf/2015/tc/c5tc02295a.

[98] W. Eysel et al. "Crystal Chemistry and Structure of Na2SO4(I) and its Solid Solutions". In: *Acta Crystallogr. B* 41.1 (1985), pp. 5–11. ISSN: 0108-7681. DOI: doi:10.1107/S0108768185001501. URL: https://doi.org/10.1107/S0108768185001501%20http://journals.iucr.org/b/issues/1985/01/00/a24363/a24363.pdf.

[99] Nonglak Meethong et al. "Aliovalent Substitutions in Olivine Lithium Iron Phosphate and Impact on Structure and Properties". In: *Adv. Funct. Mater.* 19.7 (2009), pp. 1060–1070. DOI: doi:10.1002/adfm.200801617. URL: https://onlinelibrary.wiley.com/doi/abs/10.1002/adfm.200801617%20https://onlinelibrary.wiley.com/doi/pdf/10.1002/adfm.200801617.

[100] A. L. Abdelhady et al. "Heterovalent Dopant Incorporation for Bandgap and Type Engineering of Perovskite Crystals". In: *J. Phys. Chem. Lett.* 7.2 (2016), pp. 295–301. ISSN: 1948-7185 (Electronic) 1948-7185 (Linking). DOI: 10.1021/acs.jpclett.5b02681. URL: https://www.ncbi.nlm.nih.gov/pubmed/26727130.

[101] R. Begum et al. "Engineering Interfacial Charge Transfer in CsPbBr3 Perovskite Nanocrystals by Heterovalent Doping". In: *J. Am. Chem. Soc.* 139.2 (2017), pp. 731–737. ISSN: 1520-5126 (Electronic) 0002-7863 (Linking). DOI: 10.1021/jacs.6b09575. URL: https://www.ncbi.nlm.nih.gov/pubmed/27977176.

[102] Qi Chen et al. "Ag-Incorporated Organic - Inorganic Perovskite Films and Planar Heterojunction Solar Cells". In: *Nano Lett.* 17.5 (2017), pp. 3231–3237. ISSN: 1530-6984. DOI: 10.1021/acs.nanolett.7b00847. URL: http://dx.doi.org/10.1021/acs.nanolett.7b00847%20http://pubs.acs.org/doi/pdfplus/10.1021/acs.nanolett.7b00847.

[103] K. Z. Du et al. "Heterovalent B-Site Co-Alloying Approach for Halide Perovskite Bandgap Engineering". In: *ACS Energy Lett.* 2.10 (2017), pp. 2486–2490. ISSN: 2380-8195. DOI: 10.1021/acsenergylett.7b00824. URL: %3CGo%20to%20ISI%3E://WOS:000415914200044%20https://pubs.acs.org/doi/pdfplus/10.1021/acsenergylett.7b00824.

[104] Xiaoliang Miao et al. "Air-Stable CsPb(1-x)BixBr3 ($0 \leq x < 1$) Perovskite Crystals: Optoelectronic and Photostriction Properties". In: *J. Mater. Chem. C* 5.20 (2017), pp. 4931–4939. ISSN: 2050-7526. DOI: 10.1039/C7TC00417F. URL: http://dx.doi.org/10.1039/C7TC00417F%20http://pubs.rsc.org/en/content/articlepdf/2017/tc/c7tc00417f.

[105] Mojtaba Abdi-Jalebi et al. "Impact of Monovalent Cation Halide Additives on the Structural and Optoelectronic Properties of CH3NH3PbI3 Perovskite". In: *Adv. Energy Mater.* 6.10 (2016), p. 1502472. DOI: doi:10.1002/aenm.201502472. URL: https://onlinelibrary.wiley.com/doi/abs/10.1002/aenm.201502472%20https://onlinelibrary.wiley.com/doi/pdf/10.1002/aenm.201502472.

[106] P. K. Nayak et al. "Impact of Bi(3+) Heterovalent Doping in Organic-Inorganic Metal Halide Perovskite Crystals". In: *J. Am. Chem. Soc.* 140.2 (2018), pp. 574–577. ISSN: 1520-5126 (Electronic) 0002-7863 (Linking). DOI: 10.1021/jacs.7b11125. URL: https://www.ncbi.nlm.nih.gov/pubmed/29266934%20https://pubs.acs.org/doi/pdfplus/10.1021/jacs.7b11125.

[107] Z. Y. Bin et al. "Efficient n-type dopants with extremely low doping ratios for high performance inverted perovskite solar cells". In: *Energy Environ. Sci.* 9.11 (2016), pp. 3424–3428. ISSN: 1754-5692. DOI: 10.1039/c6ee01987k. URL: %3CGo%20to%20ISI%3E://WOS:000387862100010.

[108] Y. Yamada et al. "Impact of Chemical Doping on Optical Responses in Bismuth-Doped CH3NH3PbBr3 Single Crystals: Carrier Lifetime and Photon Recycling". In: *J. Phys. Chem. Lett.* 8.23 (2017), pp. 5798–5803. ISSN: 1948-7185 (Electronic) 1948-7185 (Linking). DOI: 10.1021/acs.jpclett.7b02508. URL: https://www.ncbi.nlm.nih.gov/pubmed/29130309%20https://pubs.acs.org/doi/pdfplus/10.1021/acs.jpclett.7b02508.

[109] G. Li et al. "Ion-Exchange-Induced 2D-3D Conversion of HMA1-x FAx PbI3 Cl Perovskite into a High-Quality MA1-x FAx PbI3 Perovskite". In: *Angew. Chem. Int. Ed.* 55.43 (2016), pp. 13460–13464. ISSN: 1521-3773 (Electronic) 1433-7851 (Linking). DOI: 10.1002/anie.201606801. URL: https://www.ncbi.nlm.nih.gov/pubmed/27667326.

[110] Zhan Zhang et al. "Bandgap Narrowing in Bi-Doped CH3NH3PbCl3 Perovskite Single Crystals and Thin Films". In: *J. Phys. Chem. C* 121.32 (2017), pp. 17436–17441. ISSN: 1932-7447. DOI: 10.1021/acs.jpcc.7b06248. URL: https://doi.org/10.1021/acs.jpcc.7b06248%20https://pubs.acs.org/doi/pdfplus/10.1021/acs.jpcc.7b06248.

[111] Zhao-Kui Wang et al. "High Efficiency Pb-In Binary Metal Perovskite Solar Cells". In: *Adv. Mater.* 28.31 (2016), pp. 6695–6703. DOI: doi:10.1002/adma.201600626. URL: https://onlinelibrary.wiley.com/doi/abs/10.1002/adma.201600626%20https://onlinelibrary.wiley.com/doi/pdf/10.1002/adma.201600626.

[112] Jiban Kangsabanik et al. "Double Perovskites Overtaking the Single Perovskites: A Set of New Solar Harvesting Materials with Much Higher Stability and Efficiency". In: *Phys. Rev. Mater.* 2.5 (2018), p. 055401. DOI: 10.1103/PhysRevMaterials.2.055401. URL: https://link.aps.org/doi/10.1103/PhysRevMaterials.2.055401%20https://journals.aps.org/prmaterials/abstract/10.1103/PhysRevMaterials.2.055401.

[113] Helen M. Chan, Martin R. Harmer, and Donald M. L. Smyth. "Compensating Defects in Highly Donor Doped BaTiO3". In: *J. Am. Ceram. Soc.* 69.6 (1986), pp. 507–510. DOI: doi:10.1111/j.1151-2916.1986.tb07453.x. URL: https://onlinelibrary.wiley.com/doi/abs/10.1111/j.1151-2916.1986.tb07453.x%20https://onlinelibrary.wiley.com/doi/pdf/10.1111/j.1151-2916.1986.tb07453.x.

[114] John P. Perdew, Kieron Burke, and Matthias Ernzerhof. "Generalized Gradient Approximation Made Simple". In: *Phys. Rev. Lett.* 77.18 (1996), pp. 3865–3868. URL: https://link.aps.org/doi/10.1103/PhysRevLett.77.3865%20https://journals.aps.org/prl/abstract/10.1103/PhysRevLett.77.3865.

[115] G. Kresse and J. Furthmüller. "Efficient Iterative Schemes for Ab Initio Total-Energy Calculations Using a Plane-Wave Basis Set". In: *Phys. Rev. B* 54.16 (1996), pp. 11169–11186. URL: https://link.aps.org/doi/10.1103/PhysRevB.54.11169.

[116] E. E. Salpeter and H. A. Bethe. "A Relativistic Equation for Bound-State Problems". In: *Phys. Rev.* 84 (6 Dec. 1951), pp. 1232–1242. DOI: 10.1103/PhysRev.84.1232. URL: https://link.aps.org/doi/10.1103/PhysRev.84.1232.

[117] Adam Jaffe et al. "High Compression Induced Conductivity in a Layered CuBr Perovskite". In: *under review* (2019).

[118] Y. Moritomo and Y. Tokura. "J. Chem. Phys." In: 101 (1994), pp. 1763–1766.

[119] R. Valiente and F. Rodríguez. In: *Phys. Rev. B* 60 (1999), pp. 9423–9429.

[120] K. Ohwada et al. In: *Phys. Rev. B* 72 (2005).

[121] F. Rodríguez et al. In: *Phys. Status Solidi B* 244 (2007), pp. 156–161.

[122] F. Aguado et al. In: *Phys. Rev. B* 85 (2012), p. 10010.

[123] A. Jaffe et al. "J. Am. Chem. Soc." In: 137 (2015), pp. 1673–1678.

[124] P. Ghalsasi et al. In: *Phys. Chem.* 17 (2015), pp. 32204–32210.

[125] Q. Li et al. In: *J. Phys. Chem. Lett* 8 (2017), pp. 500–506.

[126] L. Gao et al. In: *Phys. Rev. B* 50 (1994), pp. 4260–4263.

[127] C. Murayama et al. In: *Physica, C.* 183 (1991), pp. 277–285.

[128] J. S. Schilling. "in Frontiers of High Pressure Research II: Application of High Pressure to Low-Dimensional Novel Electronic Materials". In: *Vol.* Eds.: H. D. Hochheimer, B. Kuchta, P. K. Dorhout, J. L. Yarger), Springer, New York, 2001, pp. 345–360.

[129] R. Willett, H. Place, and M. Middleton. "J. Am. Chem. Soc." In: 110 (1988), pp. 8639–8650.

[130] R. Willett. In: *Acta. Cryst. Sect. B* 46 (1990), pp. 565–568.

[131] D. B. Mitzi. "in Prog". In: *Inorg. Chem., Vol. 48, -VCH, Weinheim.* 1999, pp. 1–121.

[132] Adam Jaffe et al. "Pressure-Induced Conductivity and Yellow-to-Black Piezochromism in a Layered CuCl Hybrid Perovskite". In: *Journal of the American Chemical Society* 137.4 (2015). PMID: 25580620, pp. 1673–1678. DOI: 10.1021/ja512396m. URL: https://doi.org/10.1021/ja512396m.

[133] S. Gupta, T. Pandey, and A. K. Singh. In: *Inorg Chem* 55 (2016), pp. 6817–6824.

[134] P. Zolfaghari, G. A. d. Wijs, and R. A. d. Groot. In: *J. Phys. Condens. Matter* 25 (2013), p. 29550.

[135] D. Cortecchia et al. In: *Inorg Chem* 55 (2016), pp. 1044–1052.

[136] J. P. Perdew, K. Burke, and M. Ernzerhof. In: *Phys. Rev. Lett* 77 (1996), pp. 3865–3868.

[137] A. Tkatchenko and M. Scheffler. In: *Phys. Rev. Lett* 102 (2009), p. 073005.

[138] L. J. de Jongh and A. R. Miedema. In: *Adv. Phys.* 23 (1974), pp. 1–260.

[139] S. L. Dudarev et al. In: *Phys Rev. B: Condens. Matter Mater* 57 (1998), pp. 1505–1509.

[140] Aliaksandr V. Krukau et al. "Influence of the exchange screening parameter on the performance of screened hybrid functionals". In: *The Journal of Chemical Physics* 125.22 (Dec. 2006), p. 224106. DOI: 10.1063/1.2404663. URL: https://doi.org/10.1063%2F1.2404663.

[141] Michael A. Boles, ..., and Hemamala I. Karunadasa. "Encased in Gold: Halide Perovskites Containing an Extended AuX Framework and Isolated MX6 Octahedra (M = In, Sb, Bi; X = Cl, Br)". In: *under review* (2019).

[142] Sharon H. Chou et al. "DFT Study of Atomically-Modified Alkali-Earth Metal Oxide Films on Tungsten". In: *The Journal of Physical Chemistry C* 118.21 (2014), pp. 11303–11309. DOI: 10.1021/jp4120578.

[143] Jorg Neugebauer and Matthias Scheffler. "Adsorbate-substrate and adsorbate-adsorbate interactions of Na and K adlayers on Al(111)". In: *Phys. Rev. B* 46 (24 Dec. 1992), pp. 16067–16080. DOI: 10.1103/PhysRevB.46.16067. URL: https://link.aps.org/doi/10.1103/PhysRevB.46.16067.

[144] M. Gajdo š et al. "Linear optical properties in the projector-augmented wave methodology". In: *Phys. Rev. B* 73 (4 Jan. 2006), p. 045112. DOI: 10.1103/PhysRevB.73.045112. URL: https://link.aps.org/doi/10.1103/PhysRevB.73.045112.

[145] Ph. Ghosez, J.-P. Michenaud, and X. Gonze. "Dynamical atomic charges: The case of ABO_3 compounds". In: *Phys. Rev. B* 58 (10 Sept. 1998), pp. 6224–6240. DOI: 10.1103/PhysRevB.58.6224. URL: https://link.aps.org/doi/10.1103/PhysRevB.58.6224.

[146] Na Sai, B. Meyer, and David Vanderbilt. "Compositional Inversion Symmetry Breaking in Ferroelectric Perovskites". In: *Phys. Rev. Lett.* 84 (24 June 2000), pp. 5636–5639. DOI: 10.1103/PhysRevLett.84.5636. URL: https://link.aps.org/doi/10.1103/PhysRevLett.84.5636.

[147] R. D. King-Smith and David Vanderbilt. "First-principles investigation of ferroelectricity in perovskite compounds". In: *Phys. Rev. B* 49 (9 Mar. 1994), pp. 5828–5844. DOI: 10.1103/PhysRevB.49.5828. URL: https://link.aps.org/doi/10.1103/PhysRevB.49.5828.

[148] Nicole A. Benedek and Turan Birol. "Ferroelectric metals reexamined: fundamental mechanisms and design considerations for new materials". In: *J. Mater. Chem. C* 4 (18 2016), pp. 4000–4015. DOI: 10.1039/C5TC03856A. URL: http://dx.doi.org/10.1039/C5TC03856A.

[149] Kevin F. Garrity, Karin M. Rabe, and David Vanderbilt. "Hyperferroelectrics: Proper Ferroelectrics with Persistent Polarization". In: *Phys. Rev. Lett.* 112 (12 Mar. 2014), p. 127601. DOI: 10.1103/PhysRevLett.112.127601. URL: https://link.aps.org/doi/10.1103/PhysRevLett.112.127601.

[150] Pengfei Li et al. "The origin of hyperferroelectricity in LiBO$_3$ (B=V, Nb, Ta, Os)". In: *Scientific Reports* 6 (Oct. 2015). DOI: 10.1038/srep34085.

[151] N. A. Spaldin and M. Fiebig. "The renaissance of magnetoelectric multiferroics". In: *Science* 309 (2005), pp. 391–392.

[152] Anubhav Jain et al. "The Materials Project: A materials genome approach to accelerating materials innovation". In: *APL Materials* 1.1 (2013), p. 011002. ISSN: 2166532X. DOI: 10.1063/1.4812323. URL: http://link.aip.org/link/AMPADS/v1/i1/p011002/s1%5C&Agg=doi.

[153] Shyue Ping Ong et al. "Python Materials Genomics (pymatgen): A robust, open-source python library for materials analysis". In: *Computational Materials Science* 68 (2013), pp. 314–319. ISSN: 09270256. DOI: 10.1016/j.commatsci.2012.10.028. URL: http://linkinghub.elsevier.com/retrieve/pii/S0927025612006295.

[154] Anubhav Jain et al. "FireWorks: a dynamic workflow system designed for high-throughput applications". In: *Concurrency Computation Practice and Experience* 27 (2015), pp. 5037–5059. DOI: 10.1002/cpe.3505.

[155] Kiran Mathew et al. "Atomate: A high-level interface to generate, execute, and analyze computational materials science workflows". In: *Computational Materials Science* 139.Supplement C (2017), pp. 140–152. ISSN: 0927-0256. DOI: https://doi.org/10.1016/j.commatsci.2017.07.030. URL: http://www.sciencedirect.com/science/article/pii/S0927025617303919.

[156] Anubhav Jain, Yongwoo Shin, and Kristin A. Persson. "Computational predictions of energy materials using density functional theory". In: *Nature Reviews Materials* 1.1 (Jan. 2016). DOI: 10.1038/natrevmats.2015.4. URL: https://doi.org/10.1038/natrevmats.2015.4.

[157] Qimin Yan et al. "Solar fuels photoanode materials discovery by integrating high-throughput theory and experiment". In: *Proceedings of the National Academy of Sciences* 114.12 (Mar. 2017), pp. 3040–3043. DOI: 10.1073/pnas.1619940114. URL: https://doi.org/10.1073/pnas.1619940114.

[158] Ru Chen et al. "Topological materials discovery using electron filling constraints". In: *Nature Physics* 14.1 (Oct. 2017), pp. 55–61. DOI: 10.1038/nphys4277. URL: https://doi.org/10.1038/nphys4277.

[159] Maarten de Jong et al. "A database to enable discovery and design of piezoelectric materials". In: *Scientific Data* 2 (2015), p. 150053. ISSN: 2052-4463. DOI: 10.1038/sdata.2015.53. URL: http://www.nature.com/articles/sdata201553.

[160] S. C. Abrahams. "Structurally Based Prediction of Ferroelectricity in Inorganic Materials with Point Group 6mm". In: *Acta Crystallographica Section B* B44 (1988), pp. 585–595. DOI: 10.1107/S0108768188010110.

[161] S. C. Abrahams. "Structurally based predictions of ferroelectricity in seven inorganic materials with space group Pba2 and two experimental confirmations". In: *Acta Crystallographica Section B* 45.3 (1989), pp. 228–232. ISSN: 16005740. DOI: 10.1107/S0108768189001072.

[162] Cesar Capillas et al. "A new computer tool at the Bilbao Crystallographic Server to detect and characterize pseudosymmetry". In: *Zeitschrift für Kristallographie* 226.2 (2011), pp. 186–196. ISSN: 0044-2968. DOI: 10.1524/zkri.2011.1321. URL: http://www.degruyter.com/doi/10.1524/zkri.2011.1321.

[163] J. M. Igartua et al. "Search for Pnma materials with high-temperature structural phase transitions". In: *Acta Crystallographica Section B Structural Science* 55.2 (1999), pp. 177–185. ISSN: 0108-7681. DOI: 10.1107/S0108768198013342. URL: http://scripts.iucr.org/cgi-bin/paper?S0108768198013342.

[164] E. Kroumova, M. I. Aroyo, and J. M. Perez-Mato. "Prediction of new displacive ferroelectrics through systematic pseudosymmetry search. Results for materials with Pba 2 and Pmc 2 1 symmetry". In: *Acta Crystallographica Section B Structural Science* 58.6 (2002), pp. 921–933. ISSN: 0108-7681. DOI: 10.1107/S0108768102012120. URL: http://scripts.iucr.org/cgi-bin/paper?S0108768102012120.

[165] H. T. Stokes et al. "Analysis of the ferroelectric phase transition in BaAl2O4 by group theoretical methods and first-principles calculations". In: *Physical Review B* 65.6 (2002), p. 064105. ISSN: 0163-1829. DOI: 10.1103/PhysRevB.65.064105. URL: http://link.aps.org/doi/10.1103/PhysRevB.65.064105.

[166] J. M. Perez-Mato et al. "Distortion modes and related ferroic properties of the stuffed tridymite-type compounds SrAl2 O4 and BaAl2 O4". In: *Physical Review B - Condensed Matter and Materials Physics* 79.6 (2009), pp. 1–12. ISSN: 10980121. DOI: 10.1103/PhysRevB.79.064111.

[167] Eva H. Smith, Nicole A. Benedek, and Craig J. Fennie. "Interplay of Octahedral Rotations and Lone Pair Ferroelectricity in $CsPbF_3$". In: *Inorganic Chemistry* 54.17 (2015), pp. 8536–8543. ISSN: 1520510X. DOI: 10.1021/acs.inorgchem.5b01213.

[168] Joseph W. Bennett. "Discovery and Design of Functional Materials: Integration of Database Searching and First Principles Calculations". In: *Physics Procedia* 34 (2012), pp. 14–23. ISSN: 18753892. DOI: 10.1016/j.phpro.2012.05.003. URL: http://www.sciencedirect.com/science/article/pii/S1875389212013168.

[169] Joseph W. Bennett et al. "Hexagonal ABC semiconductors as ferroelectrics". In: *Physical Review Letters* 109 (2012), p. 167602. ISSN: 00319007. DOI: 10.1103/PhysRevLett.109.167602.

[170] Joseph W. Bennett and Karin M. Rabe. "Integration of first-principles methods and crystallographic database searches for new ferroelectrics: Strategies and explorations". In: *J. Solid State Chem.* 195 (2012), pp. 21–31. ISSN: 00224596. DOI: 10.1016/j.jssc.2012.05.013. URL: http://dx.doi.org/10.1016/j.jssc.2012.05.013.

[171] Kevin F. Garrity. "High-throughput first-principles search for new ferroelectrics". In: *Phys. Rev. B* 97 (2 Jan. 2018), p. 024115. DOI: 10.1103/PhysRevB.97.024115. URL: https://link.aps.org/doi/10.1103/PhysRevB.97.024115.

[172] M. E. Lines and A. M. Glass. *Principles and Applications of Ferroelectrics and Related Materials*. Oxford University Press, Feb. 2001. DOI: 10.1093/acprof:oso/9780198507789.001.0001. URL: https://doi.org/10.1093%2Facprof%3Aoso%2F9780198507789.001.0001.

[173] Pierre Villars and Fritz Hulliger, eds. *PAULING FILE Multinaries Edition – 2012 in SpringerMaterials*. Copyright 2016 Springer-Verlag Berlin Heidelberg & Material Phases Data System (MPDS), Switzerland & National Institute for Materials Science (NIMS), Japan. 2012.

[174] Y. Shiozaki, E. Nakamura, and T. Mitsui, eds. *Landolt-Börnstein - Group III Condensed Matter Volume 36A1: "Ferroelectrics and Related Substances: Oxides Part 1: Perovskite-type Oxides and LiNbO3 Family"*. Springer-Verlag, 2001. DOI: 10.1007/b53034. URL: https://doi.org/10.1007/b53034.

[175] Y. Shiozaki, E. Nakamura, and T. Mitsui, eds. *Landolt-Börnstein - Group III Condensed Matter Volume 36A2: "Ferroelectrics and Related Substances: Oxides Part 2: Oxides other than Perovskite-type and LiNbO3 Family"*. Springer-Verlag, 2002. DOI: 10.1007/b82976. URL: https://doi.org/10.1007/b82976.

[176] Y. Shiozaki, E. Nakamura, and T. Mitsui, eds. *Landolt-Börnstein - Group III Condensed Matter Volume 36B1: "Ferroelectrics and Related Substances: Inorganic Substances other than Oxides Part 1: SbSI family ... TAAP"*. Springer-Verlag, 2004. DOI: 10.1007/b68045. URL: https://doi.org/10.1007/b68045.

[177] Y. Shiozaki, E. Nakamura, and T. Mitsui, eds. *Landolt-Börnstein - Group III Condensed Matter Volume 36B2: "Ferroelectrics and Related Substances: Inorganic Substances other than Oxides Part 2: (NH4)SO4 family ... K3BiCl6 2KCl KH3F4"*. Springer-Verlag, 2006. DOI: 10.1007/978-3-540-31354-0. URL: https://doi.org/10.1007/978-3-540-31354-0.

[178] Y. Shiozaki, E. Nakamura, and T. Mitsui, eds. *Landolt-Börnstein - Group III Condensed Matter Volume 36C: "Ferroelectrics and Related Substances: Organic crystals, liquid crystals and polymers"*. Springer-Verlag, 2006. DOI: 10.1007/978-3-540-31354-0. URL: https://doi.org/10.1007/978-3-540-31354-0.

[179] Anubhav Jain et al. "The Materials Project: A materials genome approach to accelerating materials innovation". In: *APL Materials* 1.1 (2013), p. 011002. ISSN: 2166532X. DOI: 10.1063/1.4812323. URL: http://link.aip.org/link/AMPADS/v1/i1/p011002/s1%5C&Agg=doi.

[180] Stefano Curtarolo et al. "AFLOW: An automatic framework for high-throughput materials discovery". In: *Computational Materials Science* 58 (June 2012), pp. 218–226. DOI: 10.1016/j.commatsci.2012.02.005. URL: https://doi.org/10.1016/j.commatsci.2012.02.005.

[181] Giovanni Pizzi et al. "AiiDA: automated interactive infrastructure and database for computational science". In: *Computational Materials Science* 111 (Jan. 2016), pp. 218–230. DOI: 10.1016/j.commatsci.2015.09.013. URL: https://doi.org/10.1016/j.commatsci.2015.09.013.

[182] G Bergerhoff and ID Brown. *Inorganic crystal structure database*. International Union of Crystallography, 1987. Chap. 2.2, pp. 77–95.

[183] Mariette Hellenbrandt. "The Inorganic Crystal Structure Database (ICSD)—Present and Future". In: *Crystallography Reviews* 10.1 (Jan. 2004), pp. 17–22. DOI: 10.1080/08893110410001664882. URL: https://doi.org/10.1080/08893110410001664882.

[184] James E. Saal et al. "Materials Design and Discovery with High-Throughput Density Functional Theory: The Open Quantum Materials Database (OQMD)". In: *JOM* 65.11 (Sept. 2013), pp. 1501–1509. DOI: 10.1007/s11837-013-0755-4. URL: https://doi.org/10.1007/s11837-013-0755-4.

[185] Scott Kirklin et al. "The Open Quantum Materials Database (OQMD): assessing the accuracy of DFT formation energies". In: *npj Computational Materials* 1.1 (Dec. 2015). DOI: 10.1038/npjcompumats.2015.10. URL: https://doi.org/10.1038/npjcompumats.2015.10.

[186] M. E. Lines and A. M. Glass. In: Oxford: Oxford University Press, 2001. Chap. Basic Concepts. ISBN: 9780198507789. URL: http://www.oxfordscholarship.com/10.1093/acprof:oso/9780198507789.001.0001/acprof-9780198507789-chapter-1.

[187] Karin M. Rabe et al. "Modern Physics of Ferroelectrics: Essential Background". In: *Physics of Ferroelectrics: A Modern Perspective*. Springer Berlin Heidelberg, 2007, pp. 1–30. DOI: 10.1007/978-3-540-34591-6_1. URL: https://doi.org/10.1007/978-3-540-34591-6_1.

[188] Boris A. Strukov and Arkadi P. Levanyuk. "General Characteristics of Structural Phase Transitions in Crystals". In: *Ferroelectric Phenomena in Crystals*. Springer Berlin Heidelberg, 1998, pp. 1–29. DOI: 10.1007/978-3-642-60293-1_1. URL: https://doi.org/10.1007/978-3-642-60293-1_1.

[189] Premi Chandra and Peter B. Littlewood. "A Landau Primer for Ferroelectrics". In: *Physics of Ferroelectrics: A Modern Perspective*. Berlin, Heidelberg: Springer Berlin Heidelberg, 2007, pp. 69–116. ISBN: 978-3-540-34591-6. DOI: 10.1007/978-3-540-34591-6_3. URL: http://dx.doi.org/10.1007/978-3-540-34591-6_3.

[190] H T Stokes and D M Hatch. *Isotropy Subgroups of the 230 Crystallographic Space Groups*. WORLD SCIENTIFIC, Jan. 1989. DOI: 10.1142/0751. URL: https://doi.org/10.1142/0751.

[191] Ulrich Müller. "Symmetry relations at phase transitions". In: *Symmetry Relationships between Crystal Structures*. Oxford University Press, Apr. 2013, pp. 196–215. DOI: 10.1093/acprof:oso/9780199669950.003.0015. URL: https://doi.org/10.1093/acprof:oso/9780199669950.003.0015.

[192] Matthew Kristofer Horton et al. "High-throughput prediction of the ground-state collinear magnetic order of inorganic materials using Density Functional Theory". In: *npj Computational Materials* 5.1 (2019), p. 2.

[193] Mois Ilia Aroyo et al. "Crystallography online: Bilbao Crystallographic Server". In: *Bulg. Chem. Commun.* 43.2 (Jan. 2011).

[194] Mois I. Aroyo et al. "Bilbao Crystallographic Server. II. Representations of crystallographic point groups and space groups". In: *Acta Crystallographica Section A Foundations of Crystallography* 62.2 (Mar. 2006), pp. 115–128. DOI: 10.1107/s0108767305040286. URL: https://doi.org/10.1107/s0108767305040286.

[195] Mois Ilia Aroyo et al. "Bilbao Crystallographic Server: I. Databases and crystallographic computing programs". In: *Zeitschrift für Kristallographie - Crystalline Materials* 221.1 (Jan. 2006). DOI: 10.1524/zkri.2006.221.1.15. URL: https://doi.org/10.1524/zkri.2006.221.1.15.

[196] Bilbao Crystallographic Server. *Structure Relations*. 2018. URL: http://www.cryst.ehu.es/cryst/rel.html (visited on 03/28/2018).

[197] Harold T. Stokes, Dorian M. Hatch, and Branton J. Campbell. *ISOTROPY Software Suite*. Available at iso.byu.edu.

[198] *mechanize Stateful programmatic web browsing.* https://pypi.python.org/pypi/mechanize/.

[199] Samuel V. Gallego et al. "MAGNDATA: towards a database of magnetic structures. I.The commensurate case". In: *Journal of Applied Crystallography* 49.5 (Oct. 2016), pp. 1750–1776. DOI: 10.1107/S1600576716012863. URL: https://doi.org/10.1107/S1600576716012863.

[200] MI Aroyo et al. "Bilbao Crystallographic Server: I. Databases and crystallographic computing programs". In: *Z. Krist.* 221.1 (2006), pp. 15–27. DOI: https://doi:10.1524/zkri.2006.221.1.15.

[201] J.P. Steadman and R.D. Willett. "The crystal structure of (C2H5NH3)2CuCl4". In: *Inorganica Chimica Acta* 4 (1970), pp. 367–371. ISSN: 0020-1693. DOI: https://doi.org/10.1016/S0020-1693(00)93307-3. URL: http://www.sciencedirect.com/science/article/pii/S0020169300933073.

Appendix A

Structural details for high pressure Li phases

Table A.1: Optimized lattice parameters (DFT–LDA) for phases of Li considered in this work

Pressure	Space Group	a (Å)	b (Å)	c (Å)			Fractional coordinates		
0 GPa	$Im\bar{3}m$	3.360	3.360	3.360	Li1	2a	0.000	0.000	0.000
10 GPa	$Fm\bar{3}m$	4.389	4.389	4.389	Li1	4a	0.000	0.000	0.000
40 GPa	$I\bar{4}3d$	5.272	5.272	5.272	Li1	16c	0.549	0.549	0.549
70 GPa	*Aba2*	6.789	8.062	5.014	Li1	8b	0.907	0.884	0.337
					Li2	8b	0.137	0.597	0.523
					Li3	8b	0.032	0.883	0.743
					Li4	8b	0.649	0.232	0.661
					Li5	8b	0.710	0.588	0.460
80 GPa	*Pbca*	4.412	4.365	7.951	Li1	8c	0.176	0.051	0.026
					Li2	8c	0.421	0.155	0.174
					Li3	8c	0.368	0.335	0.345
100 GPa	*Cmca-24*	7.622	4.280	4.267	Li1	16g	0.333	0.391	0.154
					Li2	8f	0.000	0.671	0.064
220 GPa	*Cmca-56*	15.687	3.855	3.847	Li1	16g	0.143	0.334	0.939
					Li2	16g	0.215	0.602	0.652
					Li3	16g	0.428	0.864	0.376
					Li4	8f	0.000	0.943	0.333
350 GPa	$P4_2/mbc$	3.597	3.597	4.192	Li1	8h	0.667	0.552	0.000
					Li2	8g	0.628	0.128	0.250
450 GPa	$R\bar{3}m$	2.118	2.118	4.598	Li1	6c	0.000	0.000	0.148
500 GPa	$Fd\bar{3}m$	2.830	2.830	2.830	Li1	8a	0.000	0.000	0.000

Table A.2: Generators of space groups discussed above 40 GPa [200]

Space Group	Symmetries in Seitz Notation
$I\bar{4}3d$	$\{1\|0\}$
	$\{2_{001}\|\frac{1}{2}0\frac{1}{2}\}$
	$\{2_{010}\|0\frac{1}{2}\frac{1}{2}\}$
	$\{3^+_{111}\|0\}$
	$\{m_{1-10}\|\frac{1}{4}\frac{1}{4}\frac{1}{4}\}$
	$\{1\|\frac{1}{2}\frac{1}{2}\frac{1}{2}\}$
Pbca	$\{1\|0\}$
	$\{-1\|0\}$
	$\{2_{001}\|\frac{1}{2}0\frac{1}{2}\}$
	$\{2_{010}\|0\frac{1}{2}\frac{1}{2}\}$
Cmca	$\{1\|0\}$
	$\{-1\|0\}$
	$\{2_{001}\|0\frac{1}{2}\frac{1}{2}\}$
	$\{2_{010}\|0\frac{1}{2}\frac{1}{2}\}$
	$\{1\|\frac{1}{2}\frac{1}{2}0\}$
$P4_2/mbc$	$\{1\|0\}$
	$\{-1\|0\}$
	$\{2_{001}\|0\}$
	$\{4^+_{001}\|00\frac{1}{2}\}$
	$\{2_{010}\|\frac{1}{2}\frac{1}{2}0\}$
$R\bar{3}m$	$\{1\|0\}$
	$\{-1\|0\}$
	$\{2_{110}\|0\}$
	$\{3^+_{001}\|0\}$
	$\{1\|\frac{2}{3}\frac{1}{3}\frac{1}{3}\}$
$Fd\bar{3}m$	$\{1\|0\}$
	$\{-1\|0\}$
	$\{2_{001}\|\frac{3}{4}\frac{1}{4}\frac{1}{2}\}$
	$\{2_{010}\|\frac{1}{4}\frac{1}{2}\frac{3}{4}\}$
	$\{2_{110}\|\frac{3}{4}\frac{1}{4}\frac{1}{2}\}$
	$\{3^+_{111}\|0\}$
	$\{1\|0\frac{1}{2}\frac{1}{2}\}$
	$\{1\|\frac{1}{2}0\frac{1}{2}\}$

Appendix B

Structural details on Sn-alloyed $Cs_2AgBiBr_6$ substitutions

Substitution	Total Sn concentration (atom%)	Formula	Calculated E_g
None	0	$Cs_2AgBiBr_6$	1.11 eV Indirect (expt = 1.95 eV; indirect)
Sn^{2+} @ $Ag^+ \rightarrow Ag^+$ vac	0.625	$Cs_2Ag_{0.875}Sn^{II}_{0.0625}BiBr_6$	1.07 eV Direct
Sn^{2+} @ $Ag^+ \rightarrow Ag^+$ vac	1.25	$Cs_2Ag_{0.75}Sn^{II}_{0.125}BiBr_6$	1.02 eV Direct
Sn^{2+} @ $Ag^+ \rightarrow Ag^+$ vac	2.5	$Cs_2Ag_{0.5}Sn^{II}_{0.25}BiBr_6$	0.10 eV Indirect
Sn^{2+} @ $Ag^+ \rightarrow Ag^+$ vac	5	$Cs_2Sn^{II}_{0.5}BiBr_6$	1.46 eV Indirect
Sn^{4+} @ $Bi^{3+} \rightarrow Ag^+$ vac	1.25	$Cs_2Ag_{0.875}Bi_{0.875}Sn^{IV}_{0.125}Br_6$	0.67 eV Indirect
$3Sn^{4+}$ @ $3Bi^{3+} \rightarrow Bi^{3+}$ vac	1.875	$Cs_2AgBi_{0.75}Sn^{IV}_{0.1875}$ Br_6	0.49 eV Indirect
$2Sn^{2+}$ @ 50/50 Ag^+/Bi^{3+}	2.5	$Cs_2Ag_{0.875}Sn^{II}_{0.25}$ $Bi_{0.875}Br_6$	0.64 eV Direct
$2Sn^{2+}$ @ 50/50 Ag^+/Bi^{3+}	20	$CsSn^{II}Br_3$	0.29 eV Direct
Sn^{4+} @ $Bi^{3+} \rightarrow Ag^+$ vac	10	Cs_2 $Sn^{IV}Br_6$	1.41 eV Direct
Sn^{2+} @ $Ag^+ \rightarrow$ no vac	1.25	$Cs_2Ag_{0.875}Sn^{II}_{0.125}BiBr_6$	Metallic
Sn^{4+} @ $Ag^+ \rightarrow 3Ag^+$ vac	1.25	$Cs_2Ag_{0.5}BiSn^{IV}_{0.125}Br_6$	Metallic

Table B.1: The various substitution patterns in Sn-alloyed $Cs_2AgBiBr_6$ for which band structures have been calculated. "Vac" indicates a vacancy. The oxidation states in the 'Substitution' column indicate the nominal oxidation state of the substitution based on the atomic site substituted and vacancies being introduced.

Sn^{2+} @ Ag^{+} → Ag^{+} vac

Coordinates of Sn	Coordinates of vacancy	Energy relative to lowest-energy configuration (meV) (Å)
(0.0, 0.0, 0.5)	(0.5, 0.0, 0.0)	14.2
(0.0, 0.0, 0.5)	(0.0, 0.5, 0.5)	0.0
(0.0, 0.0, 0.5)	(0.5, 0.5, 0.5)	42.8
(0.0, 0.0, 0.5)	(0.25, 0.0, 0.5)	17.4
(0.0, 0.0, 0.5)	(0.75, 0.0, 0.5)	17.2
(0.0, 0.0, 0.5)	(0.25, 0.5, 0.0)	16.1
(0.0, 0.0, 0.5)	(0.75, 0.5, 0.0)	19.3

Sn^{4+} @ Bi^{3+} → Ag^{+} vac

Coordinates of Sn	Coordinates of vacancy	Energy relative to lowest-energy configuration (meV) (Å)
(0.0, 0.0, 0.5)	(0.0, 0.0, 0.0)	0.0
(0.0, 0.0, 0.5)	(0.5, 0.0, 0.0)	140.6
(0.0, 0.0, 0.5)	(0.0, 0.5, 0.0)	0.3
(0.0, 0.0, 0.5)	(0.5, 0.5, 0.5)	139.7
(0.0, 0.0, 0.5)	(0.25, 0.0, 0.5)	111.6
(0.0, 0.0, 0.5)	(0.75, 0.0, 0.5)	110.0
(0.0, 0.0, 0.5)	(0.25, 0.5, 0.0)	157.1
(0.0, 0.0, 0.5)	(0.75, 0.5, 0.0)	157.2

$2Sn^{2+}$ @ 50/50 Ag^{+}/Bi^{3+}

Coordinates of Sn @ Ag^{+}	Coordinates of Sn @ Bi^{3+}	Energy relative to lowest-energy configuration (meV) (Å)
(0.0, 0.0, 0.0)	(0.0, 0.5, 0.0)	0.0
(0.0, 0.0, 0.0)	(0.25, 0.5, 0.5)	79.3
(0.0, 0.0, 0.0)	(0.5, 0.0, 0.5)	135.9
(0.0, 0.0, 0.0)	(0.75, 0.0, 0.0)	29.3
(0.0, 0.0, 0.0)	(0.75, 0.5, 0.5)	80.3

Table B.2: The spatial locations of the Sn atom(s) and/or vacancy and total energy of the relaxed structure computed with DFT–PBE in a 2×1×1 supercell (lattice parameters a = 22.50 Å, b = c = 11.25 Å), calculated for various substitution patterns. The qualitative features of orbital hybridization in the electronic band structures are insensitive to the configuration. "Vac" indicates a vacancy.

$3Sn^{4+}$ @ $3Bi^{3+} \rightarrow Bi^{3+}$ vac

Coordinates of vacancy	Coordinates of Sn1	Coordinates of Sn2	Coordinates of Sn3	Energy relative to lowest-energy configuration (meV) (Å)
(0.0, 0.0, 0.0)	(0.25, 0.0, 0.0)	(0.0, 0.25, 0.0)	(0.0, 0.0, 0.5)	1.3
(0.0, 0.0, 0.0)	(0.25, 0.25, 0.5)	(0.25, 0.0, 0.0)	(0.0, 0.25, 0.0)	0.5
(0.0, 0.0, 0.0)	(0.25, 0.25, 0.5)	(0.0, 0.25, 0.0)	(0.0, 0.0, 0.5)	2.4
(0.0, 0.0, 0.0)	(0.25, 0.25, 0.5)	(0.25, 0.0, 0.0)	(0.0, 0.0, 0.5)	0.0
(0.0, 0.0, 0.0)	(0.0, 0.5, 0.5)	(0.5, 0.0, 0.5)	(0.5, 0.5, 0.5)	324.7
(0.0, 0.0, 0.0)	(0.0, 0.0, 0.5)	(0.5, 0.0, 0.5)	(0.5, 0.5, 0.5)	326.0
(0.0, 0.0, 0.0)	(0.0, 0.0, 0.5)	(0.0, 0.5, 0.5)	(0.5, 0.5, 0.5)	323.9
(0.0, 0.0, 0.0)	(0.0, 0.0, 0.5)	(0.0, 0.5, 0.5)	(0.5, 0.0, 0.5)	328.5

Table B.3: The spatial locations of the Sn atoms and vacancies and total energy of the relaxed structure computed with DFT–PBE in a 2×2×1 supercell (lattice parameters a = b = 22.50 Å, c = 11.25 Å) for nominal substitution of Sn^{4+} at the Bi^{3+} site and Bi^{3+} vacancies. The qualitative features of orbital hybridization in the electronic band structures are insensitive to the configuration. "Vac" represents a vacancy.

2 Sn^{2+} @ 2 $Ag^{1+} \rightarrow$ 2 Ag^{1+} vac and 1 Sn^{4+} @ 1 $Bi^{3+} \rightarrow$ 1 Ag^{1+} vac

Site	Coordinates	Substitution
Ag	(0.0, 0.0, 0.0)	Sn
Ag	(0.0, 0.25, 0.25)	Sn
Bi	(0.5, 0.0, 0.25)	Sn
Ag	(0.0, 0.5, 0.0)	vac
Ag	(0.25, 0.25, 0.0)	vac
Ag	(0.25, 0.0, 0.25)	vac

Table B.4: Substitution pattern for the nominal mixed valence substitution case in a 320 atom supercell.

Substitution	Total energy per atom (eV)	Energy relative to undoped (eV)
none	-3.405	0
Sn^{2+} @ $Ag^{+} \rightarrow Ag^{+}$ vac	-3.437	1.654
Sn^{4+} @ $Bi^{3+} \rightarrow Ag^{+}$ vac	-3.405	2.721
$2Sn^{2+}$ @ 50/50 Ag^{+}/Bi^{3+}	-3.423	-1.289

Table B.5: The relative formation energies for the doped structures calculated based on $E_{formation} = (E_{doped} - E_{undoped}) + \sum_{\alpha} n_{\alpha}\mu_{\alpha}$ where α denotes the atomic species and the μ_{α} is the energy per atom for the respective elemental solids.

Appendix C

$(EA)_2CuBr_4$ and $(EA)_2CuCl_4$ structural details

	a (Å)	b (Å)	c (Å)	Volume (Å^3)	Cu–Cl bond length (Å) short/long/out of plane
Experiment	21.18	7.47	7.35	1162.88	2.29 / 2.98 / 2.28
After relaxation	21.75	7.38	7.30	1171.59	2.29 / 2.96 / 2.34

Table C.1: $(EA)_2CuCl_4$: relaxed from experimental structure from [201]. Comparing lattice constants after relaxation where the volume and internal coordinates were allowed to relax using PBE + TS vdW with FM ordering.

Pressure (GPa)	axial Cu–Br bond length (Å)	equatorial Cu–Br bond length (Å)	Cu–Br–Cu angle	lattice parameters (Å)
0	2.51	3.12 / 2.43	159.8°	11.90 / 7.99 / 7.45
0.59	2.50	2.98/ 2.44	163.0°	11.70 / 7.84 / 7.32
0.91	2.49	2.94 / 2.44	164.4°	11.60 / 7.76 / 7.30
1.53	2.48	2.87 / 2.45	164.9°	11.54 / 7.65 / 7.24
5	2.46	2.38 / 2.69	166.4°	11.21 / 7.34 / 6.89
15	2.50	2.32/ 2.31	168.7°	10.95 / 6.81 / 6.25
20	2.47	2.28 / 2.29	167.7°	10.76 / 6.70 / 6.13

Table C.2: Change in Cu–Br octahedral bond lengths, bond angle, and lattice parameters with increasing pressure. All calculations were done with the α phase as the starting point and with constant pressure applied, allowing the volume and internal coordinates to relax. We note there is reduced Cu–Br distortion with increasing pressure. Above 5 GPa, the α phase is no longer observed experimentally, but without further structural details, we continue using it as the starting point for the high pressure structural relaxations.